Title of Thesis

Development of A Highly Sensitive AC/DC
Magnetometer utilizing High-T_c SQUID for
Characterization of Magnetic Mixture Materials

2015, September

Mohd Mawardi Bin Saari

Graduate School of
Natural Science and Technology
(Doctor's Course)

OKAYAMA UNIVERSITY

ABSTRACT

Magnetometers have become considerably important nowadays in many fields owing to promising potentials of non-invasive magnetic technique. A magnetometer that possesses high sensitivity, compact and low-running cost is rather desired so that it is versatile compared to conventional magnetometers and applicable in many areas. This thesis reports a development of an AC/DC magnetometer using a high-T_c SQUID (high critical temperature superconducting quantum interference devices) with a flux transformer. The critical feature of the system is the use of a high-T_c SQUID and a normal conductive detection coil, which enables the realization of a compact, highly sensitive and low-running-cost system. Optimizations and improvements performed during this work to increase the performance of the developed system are presented. Implementation of a feedback system of dual excitation coil enabled a wide range of excitation magnetic field to be achieved with high resolution. Optimizations on the shape of detection coil and sample increased the sensitivity in DC susceptibility measurement. The proposed harmonic detection technique for DC susceptibility measurement was effective in improving the signal-to-noise ratio. A compensation coil technique was implemented during fabrication of detection coil for AC susceptibility measurement to archive effective reduction in interference signal from excitation magnetic field and compact integration of AC/DC detection coil. This thesis culminates with two demonstrations of the developed system in a non-destructive evaluation of moisture content in mortar and a characterization of magnetic moment distribution in low-concentration solutions of magnetic nanoparticles for bio-medical applications. The separation of magnetic properties in mixture materials was successfully achieved with high sensitivity in both applications. The developed system can be expected as a powerful instrument for explorations of magnetic properties and non-destructive tests in future.

TABLE OF CONTENTS

CHAPTER 1: INTRODUCTION

1.1 Overview

Magnetometers have a close relation in various fields and applications where they have been used to determine magnetic responses of materials. Magnetometers that are used to determined magnetic properties of materials can be properly called susceptometers. Most of magnetometers have been extensively used for material-related researches and they are indispensable instruments in the advancement of science and technology. Recently, magnetometers have been becoming considerably important for their practicality and advantages such that they have been applied in bio-medical applications [1]–[3], measurements using non-destructive technique [4], [5], magnetotellurics, magnetic microscopy, magnetocardiogram and magnetoencephalogram [6]. Early highly sensitive magnetometers were reported by S. Foner [7] using a vibrating-sample technique and D. O. Smith [8] using a vibrating-coil technique. In both reported magnetometers, induction coils were used to sense the magnetic response. Starting from these reported laboratory magnetometers, magnetometers have been widely commercialized until now to serve various purposes. The invention of superconducting quantum interference device (SQUID) had resulted in a significant advancement in sensitivity of magnetometers. A new type magnetometer utilizing superconductivity technology and high sensitivity of SQUID had been reported by M. Pelizzone et al. [9]. Nowadays, both types of conventional magnetometers utilizing induction coil and low critical temperature (low-T_c) SQUID are commercially available.

The sensitivity of the conventional magnetometers (susceptometers) can be estimated to the order of 10^{-8} A·m^2 (10^{-5} emu) for commercial magnetometers using

induction coil and less than 10^{-10} A·m² for commercial magnetometers using low-T_c SQUID and homogenous superconducting magnet [9]–[14]. Both magnetometers have advantages and drawbacks such as the induction coil magnetometers have a lower running cost and simple configuration in comparison to the low-T_c SQUID magnetometers where expensive liquid ⁴He is required [15]. Conversely, the low-T_c SQUID magnetometers show a superior sensitivity compared to the induction coil magnetometers where a high sensitivity measurement is desired in many applications. To fill the gap and overcome the drawbacks between these conventional magnetometers, a new type of magnetometer is expected. Furthermore, a few requirements that must be fulfilled and incorporated in the design of the new type magnetometer such that it must be highly sensitive, simple and compact as well as low running cost so that it can be used to serve in a wide diversity of applications. Based on these reasons, considerations and development of a more versatile magnetometer were performed in this research.

Sensitivity of a magnetometer system can be improved by using SQUID [9]. There are two types of SQUIDs utilizing different types of superconductors; low-T_c SQUIDs and high critical temperature (high-T_c) SQUIDs. The conventional ways to cool SQUIDs to their operating temperatures are by using liquid ⁴He for low-T_c SQUIDs and liquid N_2 for high-T_c SQUIDs. A high sensitivity can be achieved in low-T_c SQUIDs owing to their low energy noise $E_N \approx 4k_B T \sqrt{\pi L_{loop} C}$ compared to high-T_c SQUIDs, where k_B is Boltzmann's constant, T is the temperature of the SQUID, L_{loop} is the inductance of the SQUID loop, and C is the self-capacitance of the Josephson junction [6]. However, improvements in high-T_c SQUIDs have been made rapidly in recent years, and a sensitivity of 25 fT/Hz$^{1/2}$ at 77 K and 1 kHz has been reported [16] and further improvements can be expected in future. Moreover, cryogenic systems for high-T_c SQUIDs are simple and can be made more compact owing to smaller thermal load resulted from conduction and blackbody radiation and larger heat capacity for

liquid N_2. From this, utilization of high-T_c SQUIDs in a magnetometer system can be expected to realize a low-running-cost, compact and highly sensitive magnetometer.

In a SQUID magnetometer system, a magnetic response from a sample can be detected by means of direct magnetic coupling method and detection using a flux transformer. In the direct magnetic coupling method, the magnetic response is measured by bringing the SQUID near to the sample and the magnetic fluxes from the sample are directly coupled to the SQUID [17]. The sensitivity can be enhanced in this method by bringing the SQUID nearer to the sample if the sample is at cryogenic temperature and in a low-ambient magnetic field noise. In the case of a room-temperature sample, the tail gap (window spacing) of the dewar flask can be improved to reduce the spatial gap [18]. However, this method is not applicable for SQUID based susceptometers where the application of a high-magnetic field is necessary. A strong magnetic field will easily destabilize and saturate the SQUIDs' operation [5], [19]. To perform measurement using the SQUID in a high magnetic field environment, detection using a flux transformer can be used where the magnetic response is detected by a detection coil and transferred to the SQUID via the flux transformer. Superconducting second-order gradiometers (e.g., NbTi coils) are commonly used in commercial low-T_c SQUID magnetometers. A highly sensitive detection with a wide and flat band of magnetic response characteristic can be achieved by using superconducting detection coils; however, the design and construction of a superconducting coil including its cryogenic system is difficult in a limited spatial space. It is also difficult to achieve the complete cancellation of the effect of the applied magnetic field in the superconducting coils [10]. In the case of high critical temperature superconducting materials are used in the superconducting coils, the contact resistance introduced at coil's connections will result in increase of cut-off frequency, thus deteriorating the magnetic response characteristic and sensitivity. The use of induction coil (e.g., resistive Cu coil) as the detection coil for the flux transformer of the SQUID has

3

also been reported [20], [21]. Since the voltage is induced when an AC magnetic response is exposed to the induction coil, the SQUID can be considered as an amplifier for the detected signal. The induction coil can be properly designed to achieve a highly sensitive detection with the combination of the SQUID as shown in section 2.2. Sensitivity of the induction coil is lower in comparison to the superconducting coil in a low frequency region due to its resistive element and frequency characteristic. However, the induction coil is simpler to fabricate and realization of a compact detection coil can be expected in this method. The effect of the excitation DC magnetic field to the SQUID can be ignored and in the case of AC magnetic field, the cancellation factor of the induction coil can be easily improved. Furthermore, since the cryogenic insulation is not required, the lift-off between the sample and the detection coil can be minimized to further improve the magnetic coupling. It has also been reported that by cooling the induction coil and/or configuring the sample signal at a fixed resonant frequency, the sensitivity of the induction coil can be further improved [22].

Various types of magnetometers have been developed in order to determine magnetic properties of materials by measurement methods such as magnetic susceptibility, relaxation and remanence. In the case of susceptometers where they measure magnetic response during excitation of magnetic fields, DC and AC susceptibilities are widely utilized to characterize the magnetic properties of materials. The DC susceptibility is obtained by measuring the static magnetization of a sample under a DC magnetic field and by sweeping the DC magnetic field over a range, the so-called magnetization curve can be obtained. The AC susceptibility is obtained through the measurement of the dynamic magnetization during excitation of an AC magnetic field. From this, frequency-dependent characteristics and the dynamics of the magnetic property of materials can be assessed [10], [23], [24]. It is worthy to note that detection sensitivity of an induction coil can be improved easily in the measurement of the AC susceptibility compared to the DC susceptibility by utilizing the

frequency characteristic of the coil. A shorter time of evaluation is also can be expected in the measurement of the AC susceptibility compared to the magnetization curve measurement [25]. However, eddy current effect outside the sample and interference of excitation magnetic field must be taken under consideration upon the measurement of the AC susceptibility. To measure the static magnetization of a sample, the voltage in the detection coil can be induced by either changing the coil or the sample position. Moving-sample technique has been proven to permit high sensitivity and performance for a magnetometer in comparison to vibrating-coil technique. In the vibrating-coil technique, the vibrating coil senses the strong excitation magnetic field and signal nulling of the excitation magnetic field becomes difficult due to non-uniformities in the applied magnetic field are a function of the magnetic field [7], [8]. The dynamic magnetization of the sample can be measured by fixing the sample near the induction coil and the magnetic response resulted from the coupling of the AC magnetic field to the detection coil can be reduced by using cancellation techniques discussed in chapter 5. Functionality to evaluate the both AC and DC susceptibilities is rather necessary for a magnetometer so that it is versatile for various applications and capable to provide further information for analysis.

To realize the practicality of a magnetometer in any fields, there are a few requirements that must be fulfilled and incorporated in the design of magnetometer such that it must be highly sensitive, simple and compact as well as low running cost. Under these considerations, a compact AC/DC magnetometer utilizing a high-T_c SQUID and an induction type detection coil was developed in this research to accomplish the aforementioned requirements. Optimizations on sample shape and position, detection technique, detection coil geometry, excitation magnetic field system, AC and DC detection unit had been performed by experiments and simulations in this work.

The feasibility of the developed highly sensitive magnetometer was demonstrated in two applications where a magnetic evaluation technique was applied to magnetic mixture materials. In the first application, evaluation on moisture content in mortar was performed and a magnetic evaluation method was proposed to achieve a non-destructive and fast evaluation method compared to the conventional methods. Evaluation of moisture content is very important in this field because it relates to the safety issues in constructions. In the second application, the magnetic properties of magnetic nanoparticles in low-concentration solutions were evaluated. Magnetic nanoparticles have shown promising characteristics in many fields particularly in bio-medical applications. Their characteristics including magnetic properties are required to be characterized and optimized for each specific applications. Evaluations of magnetic properties were successfully carried out with high sensitivity using the developed system. In future, it can be expected that the developed system will play an important role in highly sensitive magnetic explorations.

1.2 Research Aim

The aim of this research is to developed a highly sensitive magnetometer (susceptometer) using a high-T_c SQUID and applying the developed system in focus areas in this research such as non-destructive tests (NDT) and bio-medical applications utilizing magnetic nanoparticles. This work is one part of the "Strategic Promotion of Innovative R&D" program under Japan Science and Technology Agency (JST) to improve high-T_c SQUID system for industry applications and promote the high-T_c SQUID sensing instrument for frontier bio and non-destructive sensing technologies.

1.3 Thesis Organization

This thesis is mostly arranged based on the chronological development during this research where the progresses were reported in the peer-reviewed literature. The contents of most chapters are drawn from literature where the author of this thesis was main author or co-author. The introduction in chapter 1 includes a brief review of the commercially available magnetometers including their advantages and drawbacks. The requirements for a new type magnetometer and its design in the detection technique are presented.

Chapter 2 explains briefly on the origin of the magnetism, measurement techniques of magnetic susceptibility and several types of magnetic sensors. Details on the SQUID theory and its control circuits, and the high-T_c SQUID used in this research are presented.

Chapter 3 describes the individual parts of the developed system. Basic characteristics and evaluations of the developed system are presented in details including experimental and simulation results.

Chapter 4 explains optimizations performed to improve detection sensitivity for DC susceptibility measurement. It consists of a consideration on a harmonic detection technique and geometry improvements of the detection coil and sample case.

Chapter 5 discusses detection methods to reduce the interference signal from the excitation magnetic field for AC susceptibility measurement. The discussion includes considerations on detection coil arrangements and integration of DC and AC detection coils to achieve a compact detection coil for both measurements.

Chapter 6 shows a demonstration of the developed system on a non-destructive and fast evaluation of moisture content in mortar using a proposed magnetic method. The results show that different moisture contents affected the magnetic property of the mixture materials

of mortar. Change of magnetization characteristic was also observed during the hydration process developed in mortar.

Chapter 7 presents evaluations of magnetic properties of magnetic nanoparticles in low concentration solutions. Reconstruction methods of magnetic moment distribution (particle size distribution) and a comparison between static and dynamic behaviors of magnetic nanoparticles are shown. An investigation on different sizes of particles is also presented. Chapter 8 summarizes the works performed in this research.

CHAPTER 2: SQUID SENSOR

A brief explanation on the origin of the magnetism, measurement techniques of magnetic susceptibility or magnetic moments and magnetic sensors will be described in the former part of this chapter. The latter part will explain on the SQUID theory, SQUID operating principle, electronic circuits and environment needed to operate the SQUIDs, and the high-T_c SQUID employed in this study.

2.1 Magnetism and Measurement Methods

Magnetism is a property of materials that respond to an applied magnetic field. If magnetic field H is applied to a material, the relation of the appeared magnetic flux density B and applied magnetic field H in the material can be described as

$$B = \mu_0 \left(H + M \right) \ \left(\text{SI unit} \right), \tag{2.1.1}$$

where μ_0 is the vacuum permeability and $\mu_0 M$ is the magnetic polarization of the material. Here, magnetization M (per unit volume) defines the behaviors of magnetic property of materials and generally can be divided into 3 major classes: diamagnetic, paramagnetic and ferromagnetic. In terms of magnetic field H, magnetization M can be expressed as

$$M = \chi \cdot H , \tag{2.1.2}$$

where χ (dimensionless) is magnetic susceptibility of materials. For diamagnetic materials, the value of χ is negative (in order of -10^{-6}); such that they will repel the applied magnetic field. For paramagnetic materials, χ is positive ($\chi \geq 10^{-5}$) and will attract to the applied magnetic field. The response of magnetization M in a small magnetic field H ($<$ a few Tesla) for diamagnetic and paramagnetic materials is approximately linear in which χ is constant.

For ferromagnetic materials, χ is positive with large value and depending on the magnetic field $\boldsymbol{H}$. This kind of magnetic behavior has a hysteresis characteristic which results in non-zero magnetization $\boldsymbol{M}$ even when magnetic field $\boldsymbol{H}$ is zero.

The origin of magnetism can be classified in two roots; (i) moving electric charges create magnetic field (Maxwell's equation) and (ii) many particles that have non-zero spin magnetic moments. The contribution of these two sources will generate their individual magnetic moment and the vector sum of them is the net magnetic moment of any system, which is the value of the total magnetization $\boldsymbol{M}$ in a volume V. Magnetic moments that consist in an atom are resulted from intrinsic magnetic moments of electron due to electron spin, electron's orbital angular moments and intrinsic magnetic moments of nuclear spins. Generally, the intrinsic magnetic moments of nuclear spins are much smaller than that of electron and negligible. In the closed shell of an atom, electron spins are paired and the electrons are distributed spherically around the atom resulting in no total angular moment. When external magnetic field is applied to this closed shell atom, the orbital motion of electrons alters to oppose the change of magnetic field inside the atom (shielding effect), similar to Lenz's law. Using classical theory of diamagnetism, the susceptibility can be expressed as

$$\chi_{diamagnetism} = -\frac{\mu_0 N Z e^2}{6m}\left\langle r^2 \right\rangle, \quad\quad\quad (2.1.3)$$

where N is number of atoms per unit volume, Z is number of electrons, e is electron charge, m is electron mass and $<r^2>$ is the mean square distance of the electrons from nucleus. For magnetic moments which are resulted from electron spins can be expressed as

$$\mu_s = -\frac{g_s \mu_B L_s}{\hbar}, \tag{2.1.4}$$

where g_s is the electron g-factor ($g_s = 2.0023$), μ_B is the Bohr magneton, L_s is the spin angular momentum and $\hbar = h/2\pi$ (h: Plank's constant). Here Bohr magneton is a physical constant and is given by

$$\mu_B = \frac{\mu_0 e \hbar}{2m} = 9.274 \times 10^{-24} \; J/T. \tag{2.1.5}$$

Similarly, magnetic moments arose from orbital angular momentum of electrons' revolution is expressed as

$$\mu_s = -\frac{g_l \mu_B L_l}{\hbar}, \tag{2.1.6}$$

where g_l is the electron orbital g-factor ($g_l = 1$) and L_l is the angular momentum of electron's orbital motion. The total magnetic moment in an atom can be determined by

$$\mu_s = -\frac{g_J \mu_B J}{\hbar}, \tag{2.1.7}$$

where g_J is the Landé g-factor and J is the total angular momentum quantum number, determined by angular momentum coupling of the total spin and orbital angular momentum.

Generally, magnetic moments of materials can be measured using 3 major methods. The first one is by measuring force exerted by a material that is placed in a non-uniform or gradient magnetic field. This technique is highly sensitive and with the combination of recent superconducting magnet technology and laser displacement detection technique, it has shown a superior sensitivity compared to other methods. However, as this technique is based on the force exerted by a gradient magnetic field, $F = MdH/dx$; measurement in a uniform magnetic

11

field is not feasible and not adaptable to highly anisotropic materials. The second one is indirect technique which measures phenomena originated from the magnetic property. This includes measurement of the Faraday effect, microwave ferromagnetic resonance measurements and so on. This technique in particular instances is highly sensitive and yet having disadvantages due to the limitation to particular phenomena that can only be observed in limited classes of materials. The last one is direct measurement method of the induced magnetic field of the materials. This technique measures the true response of the magnetic property and has been vastly used in many conventional magnetometers. During the early time of this technique, induction measurement in normal pickup coils was used where the induced voltage was amplified by conventional amplifiers. This resulted to low sensitivity of measurement and various efforts were put to improve sensitivity including in vibrating-sample and vibrating-coil techniques. In recent years, low-T_c SQUID with superconducting input coils and superconducting magnets have been implemented in which resulting in a great improvement of the sensitivity.

2.2 Magnetic Sensors

Magnetic sensors become essential in various instruments that supporting our daily life nowadays. There is a wide variety of magnetic sensors based on established law of physics phenomena that have been utilized in various fields and applications. These magnetic sensors are applied on a particular application based on their performance (i.e., operating principal, sensitivity, dynamic ranges of frequency and magnetic field, etc.), advantages and drawbacks. Some types of magnetic sensors that are commonly used are shown in Fig. 2.2.1 with respect to their typical target areas of application in terms of magnetic flux density [26]. Superconducting quantum interference device (SQUID) is the most sensitive magnetic
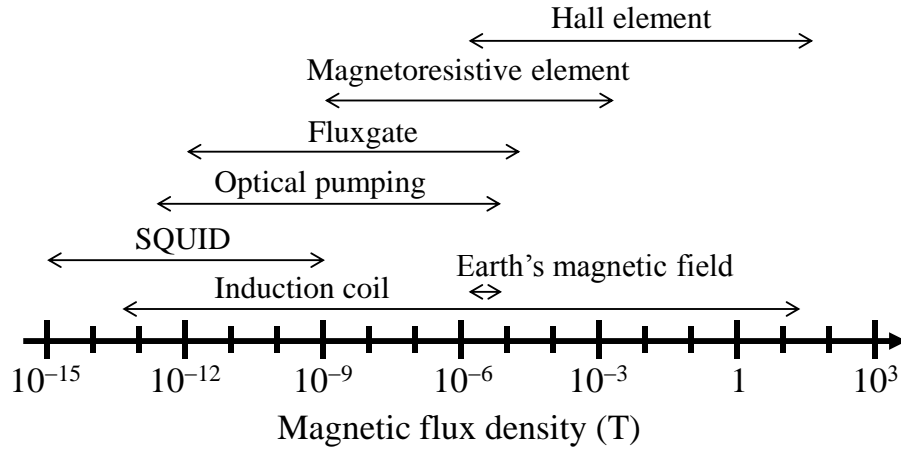
Fig. 2.2.1. Magnetic sensors and their typical target measurements of magnetic flux density.

sensor among induction coil, optical pumping magnetometer, fluxgate, magnetoresistive and Hall elements. It is noteworthy that a SQUID sensor measures the change in magnetic flux while, for an example, a fluxgate measures absolute magnetic field. The sensitivity of SQUID becomes advantageous when measuring relative changes of magnetic field. However, a sensitive magnetic sensor (e.g., SQUID) requires a low magnetic field ambient in order it to operate properly without being influenced by environmental noises. A common method to provide a low and stable magnetic field is by performing magnetic shielding using high magnetic permeability materials (e.g., permalloy) or superconducting materials utilizing Meissner effect.

The aim of this work is to develop a highly sensitive magnetometer where it measures the magnetic susceptibility of a sample under a wide range of excitation magnetic fields. For example in the measurement of a 0.1 ml water sample, its DC susceptibility is given by -9.1×10^{-6} (SI unit) and the resulted magnetic moment is in the order of 10^{-8} A·m^2 when a DC magnetic field of 100 mT is applied to it. This means that a highly sensitive magnetic sensor is required to detect the small magnetization of water. However, magnetic sensors such as SQUID, fluxgate and magnetoresistive element are simply saturated by the strong excitation magnetic field, making them not suitable for sensing in a susceptometer
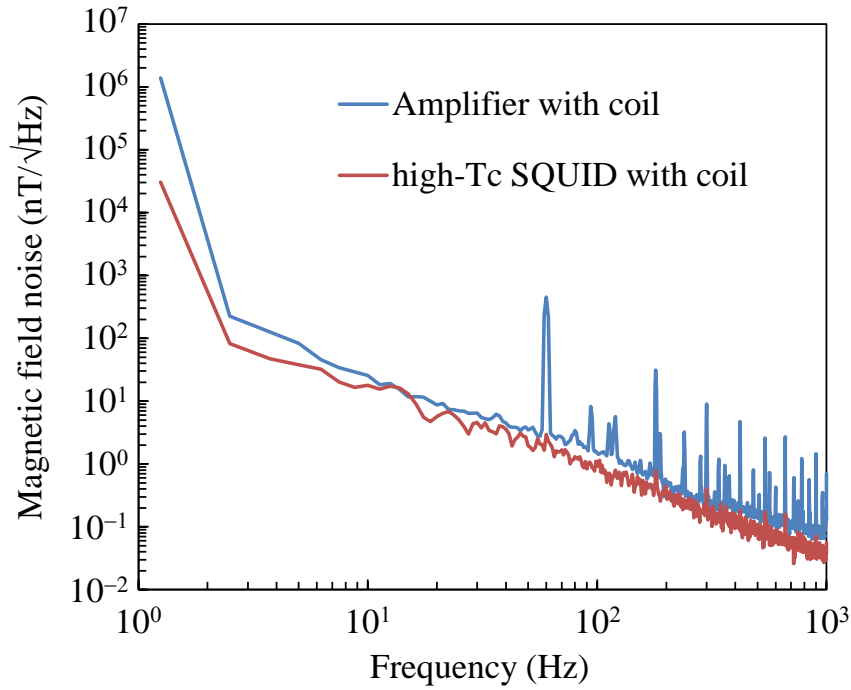
13

Fig. 2.2.2. Magnetic field noise characteristics of ultra-low-noise amplifier and high-T_c SQUID during connection to elliptical Cu coils.

system. Induction coil has proven a simple, easy-to-fabricate, compact and highly sensitive magnetic sensor over time [27]. Its performance and sensitivity can be tuned for specific applications by its design. Although it can only detect time-variant magnetic fluxes, detection of a static magnetization (DC susceptibility) of a sample can be achieved by spatial modulation of the magnetization relative to a detection coil. This modulation technique is utilized in the conventional magnetometers such as vibrating-sample [7] and vibrating-coil magnetometers [8]. In the conventional magnetometers, an induced voltage at a detection coil is amplified and measured by semiconductor amplifiers and their typical sensitivity is in the order of 10^{-8} A·m². The main factor that limit the sensitivity in the conventional magnetometers is the thermal noise of the semiconductor amplifiers. The thermal noise of typical ultra-low-noise amplifiers is in the order of 300 pV/Hz$^{1/2}$ [21], [28], while the thermal noise of induction coils can be reduced further depending on the coil design. This means that the sensitivity can be improved by using a more superior amplifier.

14

SQUID has been used in many exotic applications [6], [29] and is not only limited as a magnetic sensor. Because of its superior sensitivity and wide dynamic range in terms of frequency and magnetic field, SQUID is also utilized as a highly sensitive picovoltmeter [6], [30], [31] and picoammeter [32], [33]. By using a SQUID as an amplifier for a susceptometer, improvement in sensitivity can be expected. This was proved by the first type of susceptometer utilizing a low-T_c SQUID [9]. In the SQUID based susceptometer, a flux transformer method is used where the magnetization detected at a detection coil is transferred to a magnetically shielded SQUID. A preliminary comparison of magnetic noise between a high-T_c SQUID used in this research and an ultra-low-noise semiconductor amplifier (NF Corporation, SA-200F3) was performed when they were connected to a detection coil. The typical voltage noise of the semiconductor amplifier was 500 pV/Hz$^{1/2}$ and the detection coil was composed of a pair of 200-turn elliptical coils. The inductance, resistance and wire diameter of the elliptical coils were 294 μH, 1.953 Ω and 0.32 mm, respectively. The magnetic noise in the both cases are shown in Fig. 2.2.2. It was found that the magnetic field noise increased by 2 times in the region below 1 kHz for the semiconductor amplifier in comparison to the SQUID. Large interference spectra were also observed in the magnetic noise characteristic of the semiconductor amplifier. This could reduce the sensitivity of magnetometer in the case of performing measurement in the noise band. From this preliminary result, it was concluded that the sensitivity of a susceptometer using an induction coil as sensing sensor could be improved by using a SQUID as a high performance amplifier.

2.3 SQUID Theory

One SQUID consists of a superconducting loop and one or two weakly-coupled superconducting junctions called Josephson junction [15]. It combines the physical
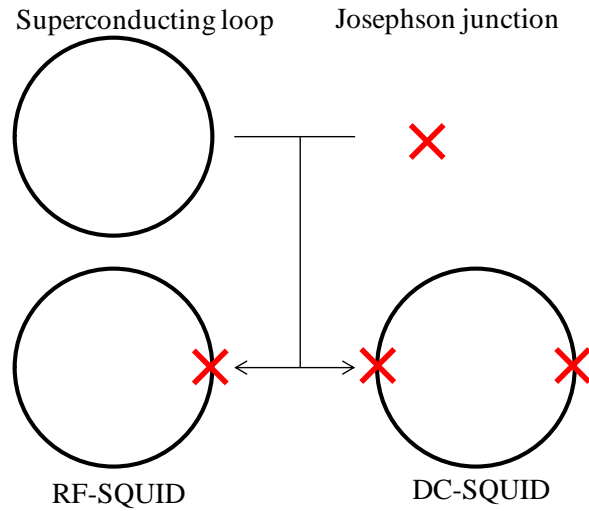
Fig. 2.3.1. RF-SQUID and DC-SQUID basic structures.

phenomena of flux quantization and Josephson tunneling effect. Because it is operated in the superconducting state, the supercurrent flowing through the ring has relatively very small resistance (nearly zero) and very sensitive to the flux change in the superconducting loop. SQUIDs are commonly operated in resistive mode where small changes in current and flux are converted into voltage as output. The flux contained in a closed superconducting loop is quantized in units of the flux quantum $\Phi_0 = h/2e \approx 2.07 \times 10^{-15}$ Wb. Here $h \equiv 2\pi\hbar$ is Plank's constant, and e is the electronic charge. SQUIDs can be categorized in 2 types depending on the number of Josephson junction. As shown in Fig. 2.3.1, the RF-SQUID consists of one Josephson junction and DC-SQUID consists of two Josephson junctions.

In the early day of SQUIDs development, RF-SQUID was widely used since it was easier to manufacture a single junction rather than two junctions; however the situation was reversed by the development of cylindrical DC-SQUID [34] and advancement in the thin-film fabrication process of the semiconductor. Theoretically, DC-SQUID is superior to RF-SQUID in term of flux noise characteristic and this was proven experimentally where a sensitivity of 10^{-14} T$\sqrt{}$Hz could be attained by DC-SQUIDs in many cases.
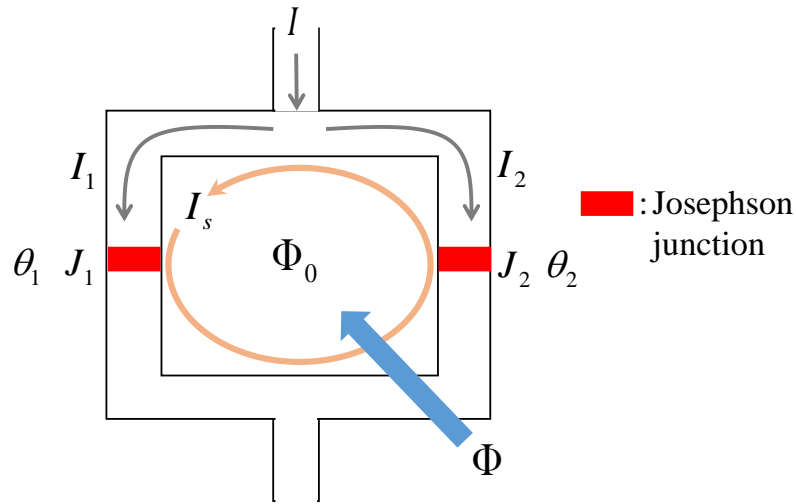
Fig. 2.3.2. Schematic drawing of DC-SQUID

The DC-SQUID operating principle can be simply explained using Fig. 2.3.2. From Josephson tunneling effect, the current I flowing through a junction is given by [15]

$$I = I_0 \sin \theta .$$ (2.3.1)

Using above expression, the sum of the current I flowing through two junctions in Fig. 2.3.2 can be obtained as

$$I = I_1 + I_2 = I_{c1} \sin \theta_1 + I_{c2} \sin \theta_2 .$$ (2.3.2)

Here, I_{c1} and I_{c2} are critical currents; θ_1 and θ_2 are phase differences of superconducting wave function. The total current I flowing through the superconducting loop changes as the total flux through the SQUID is changed and the relation between θ_1, θ_2 phase difference and total flux through the SQUID can be shown as

$$\theta_1 - \theta_2 = 2\pi(\Phi / \Phi_0) + 2\pi n ,$$ (2.3.3)

where n is a integer. As $2\pi n$ from equation (2.2.3) can be omitted, the equation can be simplified to

$$\theta_1 - \theta_2 = 2\pi(\Phi / \Phi_0). \tag{2.3.4}$$

Assuming both critical currents are identical, $I_{c1} = I_{c2} = I_c$, the total current flowing through the superconducting loop can be expressed as

$$I = 2I_c \sin\left(\frac{\theta_1 + \theta_2}{2}\right)\cos\left(\frac{\theta_1 - \theta_2}{2}\right)$$

$$= 2I_c \cos\left(\frac{\pi\Phi}{\Phi_0}\right)\sin\left(\theta_1 + \frac{\pi\Phi}{\Phi_0}\right). \tag{2.3.5}$$

Therefore, the maximum current can be shown, in absolute unit, as

$$I_{max} = 2I_c \left|\cos\left(\frac{\pi\Phi}{\Phi_0}\right)\right|. \tag{2.3.6}$$

Equation (2.3.6) shows that the maximum current has a periodic behavior of Φ_0, depending on magnitude of total flux through the loop. It becomes maximum when the total flux through the loop is an integer number of Φ_0 and minimum at half integer values.

Fig. 2.3.3 shows basic characteristic of SQUID. As the bias current flowing through SQUID is increased, the output voltage remains zero until it reaches critical current. When the bias current exceeds the critical current, SQUID starts to show resistive behavior and output voltage is observed as a and b shown in Fig.2.3.3. This is due to the Josephson barriers limit the tunneling of cooper pairs, therefore showing electrical resistance.

When a magnetic flux Φ is applied at the superconducting loop of the SQUID, the shielding current I_s is induced and it circulates within the loop due to Meissner effect of superconductivity. The superconducting loop of the SQUID maintains the threaded magnetic
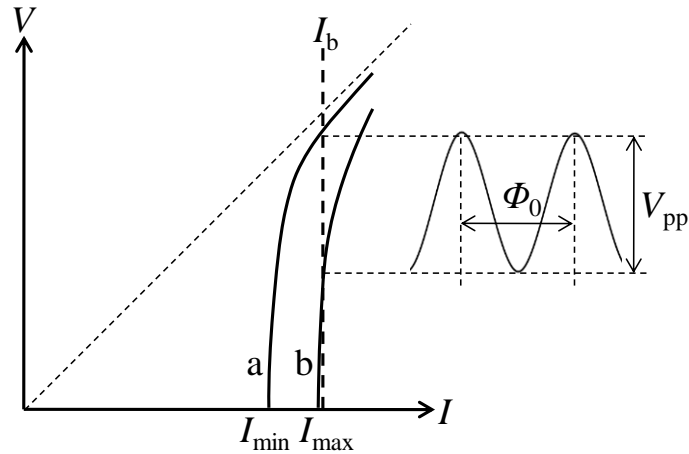
Fig. 2.3.3. Current-voltage characteristics at integer and half-integer values of applied flux; bias current I_b operating point; output voltage at operating point.

flux at an integer value of $n\Phi_0$ due the quantum effect; however, as the applied magnetic flux increases, the Josephson junctions limit the flowing of the shielding current. This causes the magnetic flux to increase by Φ_0 at the superconducting loop where the flowing direction of shielding current is reversed to compensate the quantization of the magnetic flux. The further increase of the magnetic flux causes the shielding current to oscillate, therefore, resulting the superconducting current flowing through the Josephson junctions to oscillate. When the SQUID is biased at an appropriate constant current I_b (Fig. 2.3.3) within the region of I_{min} and I_{max} (resistive mode), this causes the voltage to swing between two extrema, producing the oscillations with period Φ_0 shown in the right side of Fig. 2.3.3. The maximum response to a small flux change $\delta\Phi << \Phi_0$ is obtained when $\Phi \approx (2n+1)\Phi_0/4$, where the flux-to-voltage transfer coefficient $V_\Phi \equiv |(\partial V/\partial \Phi)_I|$ is a maximum. The resulting voltage change $\delta V = V_\Phi \delta\Phi$ is approximately linear in $\delta\Phi$ in this regime.

2.4 SQUID Electronics

In this chapter, the electronics needed to read out the information of a DC-SQUID used as a flux sensor, i.e., to quantitatively determine the amount of the applied flux signal threading the SQUID loop, and also to control the device's settings in order to attain the optimum sensitivity and accuracy of the flux measurement, will be briefly explained. As shown in chapter 2.3, the SQUID acts as a flux-to-voltage converter with a non-linear, periodic V-Φ characteristic where V is the voltage across the SQUID and Φ is the applied flux. To convert this non-linearity into linear output, feedback circuit called Flux-locked Loop (FLL) circuit is used. There are two types of FLL circuit which are flux modulation readout scheme and direct readout scheme, as shown in Figs. 2.4.1 and 2.4.2.

Flux modulation readout FLL circuit has been used widely since the early time of the SQUID. A square wave modulation flux Φ_{mod} of typically 100 kHz is applied to the SQUID such that it is periodically switched between two working points W^+ and W^- placed at
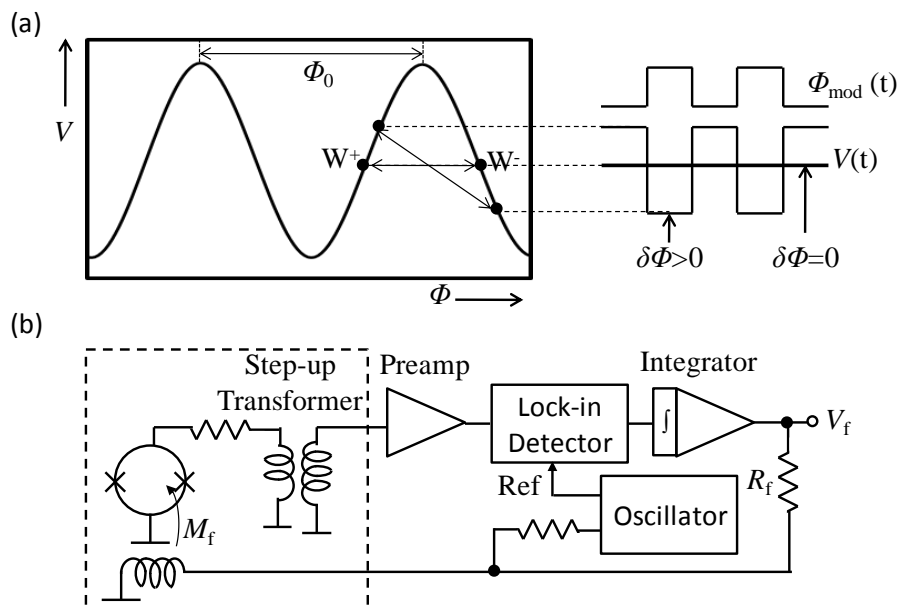

Fig. 2.4.1. Flux modulation readout FLL circuit. (a) V-Φ characteristic, (b) The FLL circuit.

adjacent slopes of its V-Φ characteristic (Fig. 2.4.1 (a)). Using square-wave modulation, the SQUID is always biased at points with minimum noise. Sinusoidal modulation minimizes the detrimental effect of switching transient but increases the noise because the SQUID passes through points with reduced or even no sensitivity. Assume there is zero alternating voltage across the SQUID without applied flux ($\delta\Phi$=0). A positive change in flux $\delta\Phi$>0 leads to a square-wave SQUID voltmeter which is out of phase with the modulation flux (see signals $\Phi_{mod}(t)$ and V(t) in Fig. 2.4.1 (a)). For a negative flux $\delta\Phi$<0, the alternating SQUID voltage will be in phase with the modulation flux. Therefore, the applied flux can be sensed by synchronously detecting the SQUID output voltage at the modulation frequency. The alternating voltage across the SQUID is increased by a cooled step-up transformer, further amplified at room temperature, and lock-in detected at the modulation frequency. A small resistance is placed between the SQUID and the transformer primary to avoid the SQUID being shorted by the transformer. The lock-in detector output signal, which an image of the V-Φ characteristic, is integrated and fed back as a current into a feedback coil. The feedback coil is magnetically coupled to the SQUID and the feedback flux will counterbalance the flux applied to the SQUID. The voltage V_f across the feedback resistor R_f is the linearized output signal [15].

In the early 1990s, a few groups worked on a new approach, direct readout scheme, to simplify the readout electronic. This new approach eliminates the need of cryogenic-temperature components, e.g., cooled step-up transformer, while providing a high bandwidth system and has been used for multichannel applications. The direct readout FLL circuit is shown in Fig. 2.4.2. The SQUID is biased at a fixed working point W, which is located at the steepest part of the V-Φ characteristic. A positive change in flux $\delta\Phi$ will cause a positive change in SQUID voltage δV. The difference between the SQUID voltage and the voltage at the working point V_b is amplified, integrated and fed back into the SQUID via a
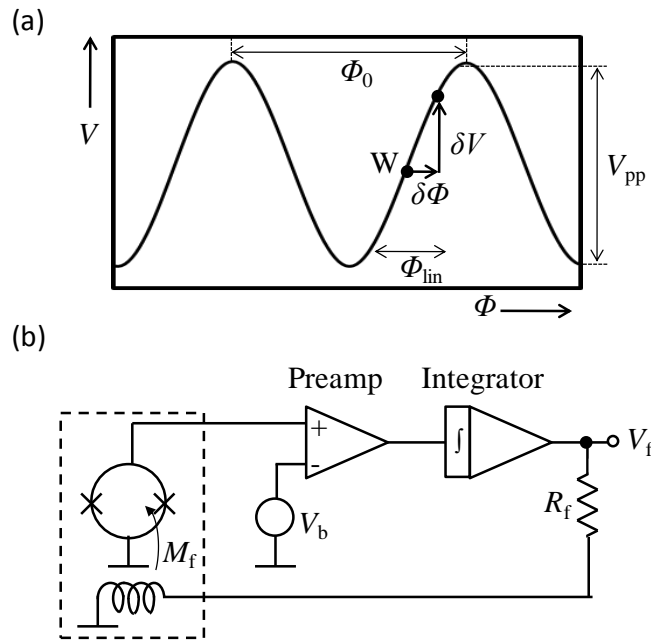
21

Fig. 2.4.2. Direct readout FLL circuit. (a) Φ-V characteristic, (b) The FLL circuit.

feedback resistor R_f and a feedback coil which is magnetically coupled to the SQUID via a mutual inductance M_f. This feedback flux counterbalances the flux applied to the SQUID resulting in the working point W to be fixed at a same point. The voltage V_f across the feedback resistor depends linearly on the applied flux and by reading out the voltage V_f, the applied flux can be measured.

Flux modulation readout has advantage in suppressing $1/f$ and white noise compared to direct readout while direct readout can provide higher system bandwidth and the circuit is more compact than that with flux modulation. A direct readout FLL circuit (Magnicon GmbH, Germany) was used in this system development.

2.5 High-T_c SQUID

In this study, a DC SQUID which was fabricated from high critical temperature superconductor materials by ISTEC-SRL (International Superconductivity Technology

Center – Superconductivity Research Laboratory) in Japan was employed [35]. The high-T_c SQUID module was mainly composed of an input coil and a SQUID chip. The input coil was fabricated from a single high critical temperature superconductor layer in a flip-chip configuration. The superconducting thin-film input coil was used in order to reduce signal attenuation due to resistance. This resulted also in high magnetic coupling between the SQUID and input coil. The input coil had 59 turns. The high-T_c SQUID was configured to be a directly coupled first-order gradiometer, instead of a magnetometer, to improve its rejection of external noise. Moreover, to permit operation under a high-magnetic field comparable with low-T_c SQUIDs, the high-T_c SQUID was fabricated with a ramp-edge Josephson junction on an MgO substrate with a gradiometer configuration. $SmBa_2Cu_3O_y$ (SmBCO) and $Er_{0.95}La_{0.1}Ba_{1.95}Cu_3O_y$ (L1ErBCO) were used as the base and counter electrodes, respectively. Up until now, high-T_c SQUIDs fabricated using bicrystal and step-edge Josephson junctions are widely used such that they can be fabricated through simple processes incorporating single-layer superconducting films. However, the critical current I_c and the junction normal-state resistance R_n of high-T_c SQUIDs fabricated in these kinds of Josephson junctions are difficult to control and will result in large spread of I_c and R_n parameters, reducing the reproducibility of the SQUIDs. Even though the fabrication techniques of ramp-edge Josephson junctions are complicated and difficult, improvement of the product of I_cR_n, and high reproducibility can be expected, and a few groups had demonstrated successful fabrication of high-T_c SQUIDs containing ramp-edge Josephson junctions. Furthermore, the ramp-edge Josephson junctions will also introduce great flexibility in layout designs of the SQUIDs compared to bicrystal and step-edge Josephson junctions (i.e., in the layout of bicrystal Josephson junctions, the Josephson junctions must be fabricated at the grain boundary of the disoriented substrates). It has been shown that the ramp-edge Josephson junction provides high-stability SQUID operation in the presence of the external field

because of its resilience to flux trapping and hopping at junctions, resulting in low flux noise of SQUIDs [6], [19]. The input coil substrate was placed over the high-T_c SQUID gradiometer substrate (flip-chip configuration) with an overall size of 7.5 mm × 15 mm, as shown in Fig. 2.5.1. The SQUID inductance and the calculated mutual inductance were 40 pH and 1.95 nH, respectively. The DC bias current, modulation voltage, and transfer function were 9.3 μA, 38 μV$_{p-p}$, and 0.51 V/Φ_0, respectively. For feedback coil, 3-turn on-chip feedback coil was fabricated on top of the SQUID loop. The coupling between SQUID and feedback coil was measured to be 66.8 μA/Φ_0.

The sequence from top of the multilayer materials is given by L1ErBCO/SrSnO$_3$ (SSO)/SmBCO/SrSnO$_3$/Pr$_{1.4}$Ba$_{1.6}$Cu$_{2.6}$Ga$_{0.4}$O$_y$ (P4G4)/BaZrO$_3$ (BZO) on MgO substrate. Except L1ErBCO, all layers were deposited by off-axis magnetron sputtering method and the counter-electrode of L1ErBCO was deposited using pulsed laser deposition technique. The L1ErBCO was selected as the counter electrode layer due to its lower deposition temperature compared to the SmBCO layer. The black-colored P4G4 layer was expected to work as a temperature homogenizer over the whole substrate during the deposition of the upper layers, which has similar crystal structure to YBCO. The BZO layer was inserted as the buffer layer to improve the crystal orientation of the P4G4 layer. To form the weak coupling barrier between upper and lower superconducting layers, a poor Cu precursor layer (L1ErBCO layer with a few tens percent poor in Cu content) was deposited using pulsed laser deposition technique prior to deposition of counter electrode. The structure of the ramp-edge was formed using standard photolithography using a resist reflow process and Ar ion milling with incident angle of 30° to the substrate surface. Details of the fabrication process are reported in reference [36]. The flux noise of the one high-T_c SQUID gradiometer is shown in Fig. 2.5.2. These noise characteristics were measured by ISTEC-SRL prior to the shipping of the high-T_c SQUID, consisting of measurements with/without pickup coil during AC and DC biases. The
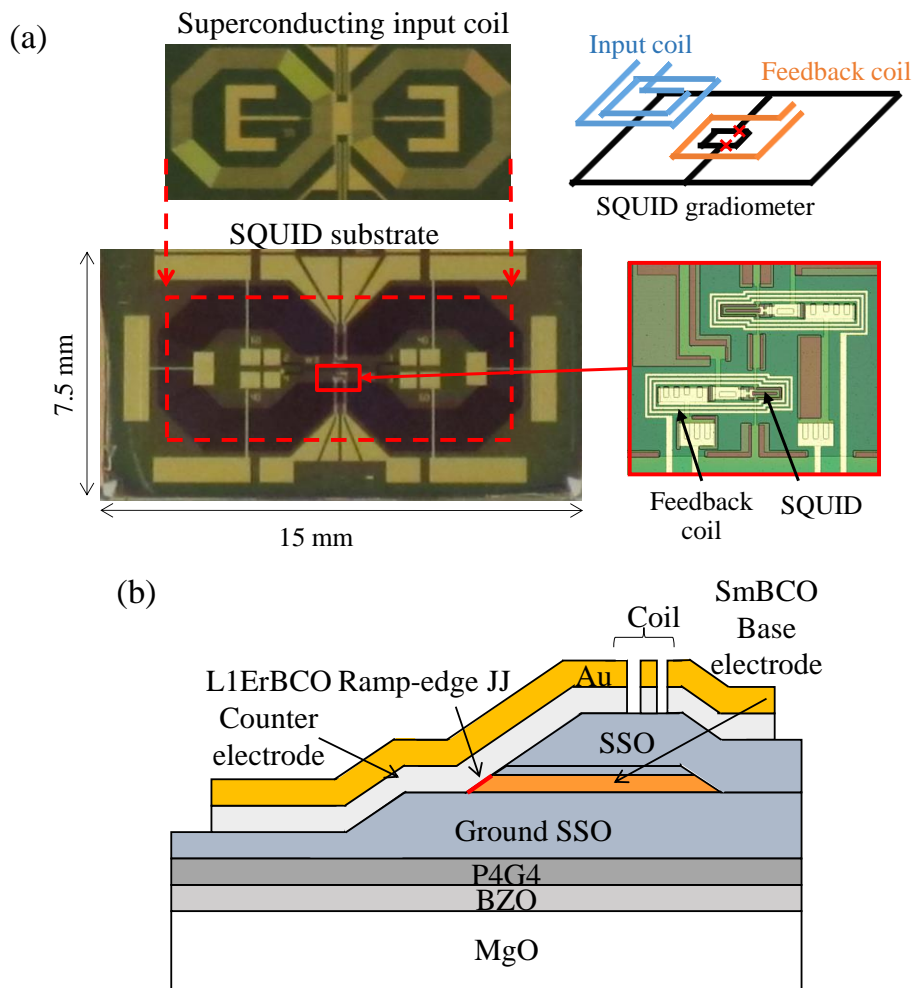
Fig. 2.5.1. (a) Directly coupled high-T_c SQUID planar gradiometer and input coil substrates. (b) Cross-sectional view of a SQUID.

used pickup coil was consisted of 5-layer 0.04-mm Litz wires wounded in 30 turns. The internal and outer diameters were 40 mm, and 46.8 mm, respectively. As shown in Fig. 2.5.2 for measurement result without the pickup coil with DC bias, the spectrum strength increased when the frequency becomes smaller in the region of below 500 Hz. This is called 1/f noise ("flicker" noise) which is caused by motion of flux lines trapped in the body of the SQUID and fluctuations of critical current and resistance in the Josephson junctions. In the region of 700 Hz and higher, white noise became dominant. This is caused by the thermal fluctuations at the Josephson junctions. This noise has characteristic of being frequency-independent
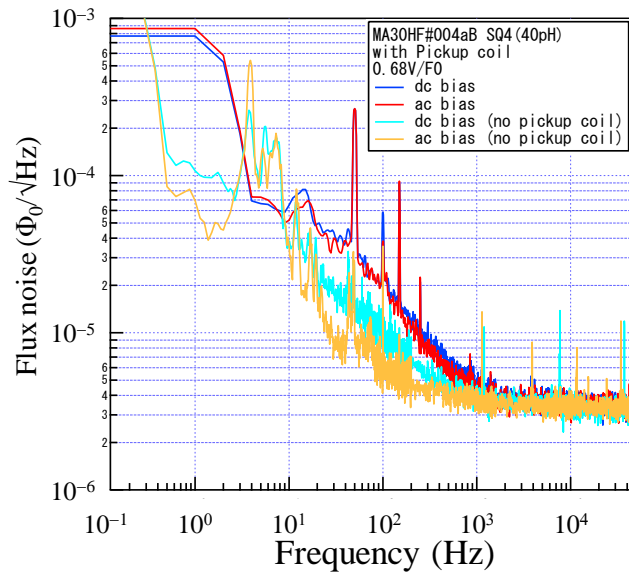
Fig. 2.5.2. Representative of the flux noise of the high-T_c SQUID with/without pickup coil during AC and DC biases.

noise and highly related to the SQUID temperature and the flux-to-voltage transfer coefficient. For above reasons, SQUIDs noise can be generally divided to $1/f$ noise and white noise. The white noise will limit the sensitivity of SQUIDs in high frequency measurement, while in low frequency measurement, the $1/f$ noise becomes problematic. The orange-colored line represents the noise characteristic during AC bias mode, which showed improved noise characteristic in comparison to DC bias mode. The use of flux modulation scheme, bias current reversal scheme and improving SQUID quality can be methods to suppress the $1/f$ noise.

CHAPTER 3: DEVELOPMENT OF HIGH-T_C SQUID MAGNETOMETER

In this chapter, the overall system setup is shown and components used in the developed system are described in former parts. In latter parts, optimizations of sample position, sample shape and a preliminary evaluation on the developed magnetometer system are presented.

The system configuration of the developed system is shown in Fig. 3. A sample is positioned between the poles of an electromagnet under a given excitation DC magnetic field. The secondary magnetic field generated from the magnetized sample is sensed by reciprocating the position of the sample horizontally. The reciprocating motion of the sample
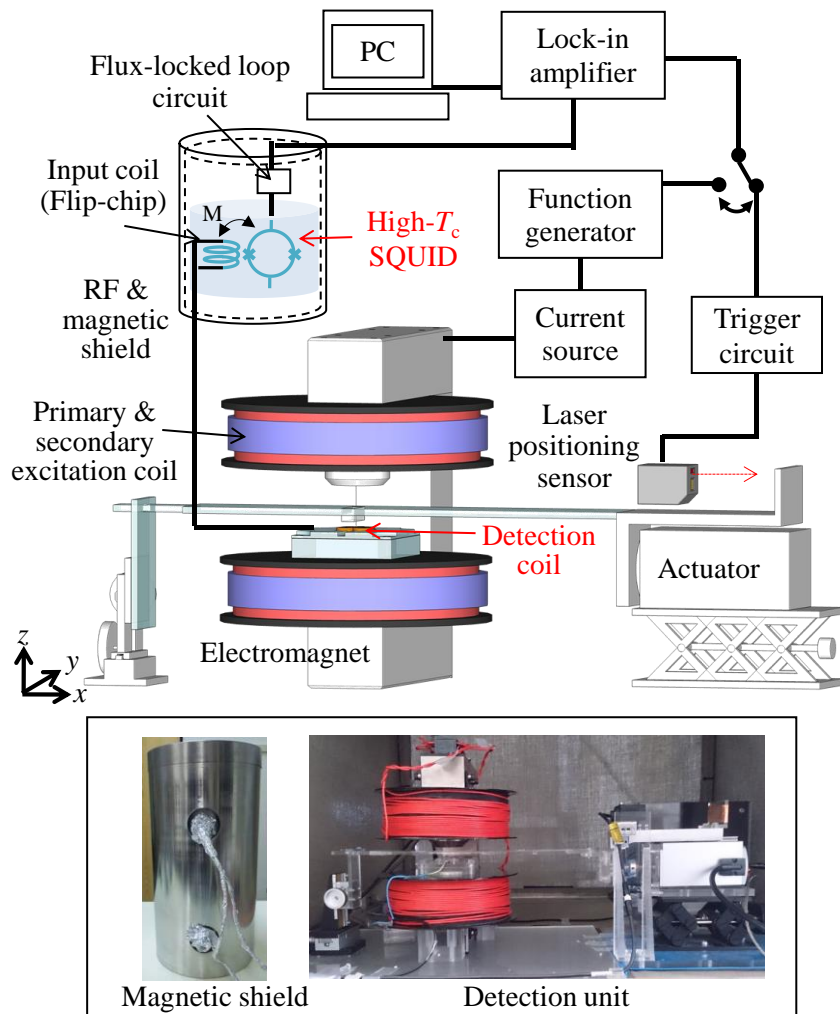

Fig. 3. Schematic diagram and actual images of the developed system.

is achieved by using a computer-controlled actuator. The sample and actuator are coupled by a 1 mm acrylic sample holder and separated by 290 mm. From the reciprocating motion, the static magnetization of the sample is modulated and sensed as an AC signal at the detection coil. The detected signal is transferred to the SQUID through the inductively coupled superconducting input coil. The SQUID output is detected by a lock-in amplifier, and the obtained data were recorded and analyzed by a computer (Labview). The lock-in detection enables a higher signal-to-noise ratio to be realized by selecting signals in the vibration frequency band [5]. A laser-positioning sensor is used to monitor the sample position, and as a phase reference to the detected signal.

3.1 Detection Unit

To decrease the effects of distant noise and the applied magnetic field, the detection coil was made to be a first-order planar differential coil (see Fig. 3.1.1). This type of coil is sensitive to the difference in flux changes between 2 loops, and will cancel out the distant magnetic field as its gradient is small with same rate of flux changes within these 2 loops. Thus, it permits measurement without further magnetic shielding at the sample. The first-order differential coil consisted of two identical circular coils connected in a series-opposing configuration. One coil had 200 turns and was fabricated from a copper wire with a diameter of 0.32 mm; its internal and external diameters, length, resistance, and inductance were 9 mm, 17 mm, 5 mm, 2.08 Ω, and 446.2 μH, respectively. The detection coil is connected in series with the input coil. These coils configuration are shown in Fig. 3.1.2.

In order to estimate performance of the detection coil characteristic, a calculation on effective area was done [24]. To simplify the simulation, a detection coil consisted of one circular coil, i.e. magnetic field response at one coil was measured while another coil acted
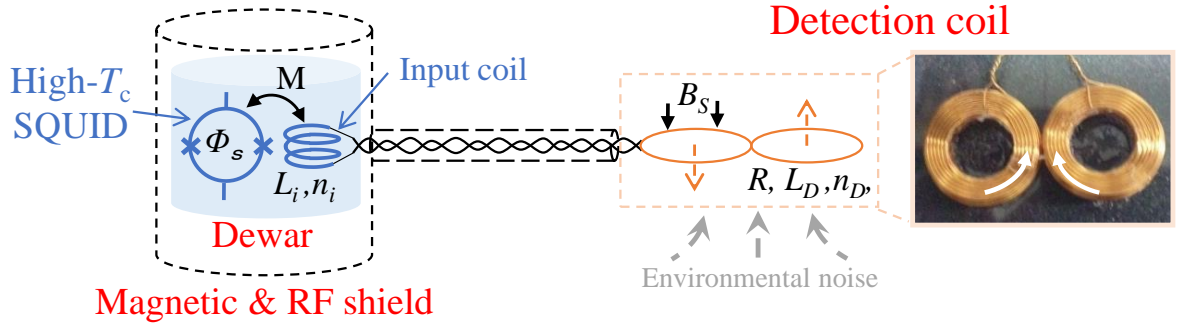
Fig. 3.1.1. Detection unit.

as a reference coil, was considered. The relationship between the signal flux applied to the SQUID Φ_s and magnetic field of the sample B_S is given by

$$\Phi_s \approx \frac{M n_D \pi r_D^2 \omega B_S}{\sqrt{R^2 + (\omega L_D)^2}} ,$$ (3.1.1)

where M, n_D, r_D, L_D, ω, and R are mutual inductance between the SQUID and the input coil, number of turns of the circular coil (200 turns), the average radius of the circular coil (6.8 mm), the series inductance of the detection coil (892.4 µH), frequency, and total resistance of the coil circuit (4.3 Ω), respectively. Here, $L_D \gg L_i$, and $M = 1.88$ nH are assumed. By substituting these values using above parameters into equation (3.1.1), the simulation result is shown in Fig. 3.1.2. The effective area represents the sensitivity of the detection coil. From
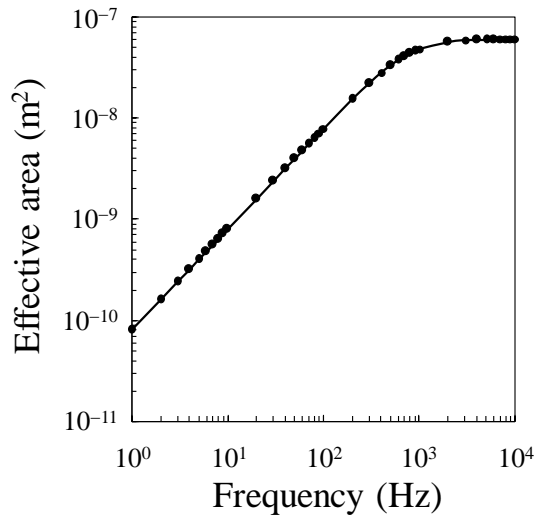

Fig. 3.1.2. Estimated frequency response of the system.

this result, the value of effective area increases with the frequency and then saturates with the cutoff frequency around 900 Hz. In this system, the sample is vibrated approximately at 3 Hz and the effective area can be estimated in the order of 10^{-10} m^2.

Fabrication of high-T_c SQUIDs is much more difficult compared to low-T_c SQUIDs. However, cooling of high-T_c SQUIDs is much simple and the running cost is inexpensive as liquid nitrogen is used. SQUIDs can be cooled by two methods; either by a cryogenic liquid or by a cooler. A simple method of cooling is to immerse the high-T_c SQUID in liquid nitrogen that is contained in a dewar flask. In this study, the dewar was designed to have two layers of Fiber Reinforced Plastics (FRP) with the gap between inner and outer casing was in vacuum state. Furthermore, the inner casing was wrapped with superinsulation to reduce radiative heat flow. A sensor probe was used to attach the SQUID at the end of it, so that the installation and replacement of a SQUID chip can be done easily. The probe was made of Glass Fiber Reinforced Plastics (GFRP) with a foam plug at the neck of it. Space between the dewar and the probe was sealed by o-rings attached at the neck of the probe.

Environmental radio frequency noise and Earth's magnetic field may have a major effect in the SQUID performance and increase noise in measurements. When a sensitivity of measurement below Earth's field and ambient magnetic field is desired, e.g., Magnetoencephalography (MEG) and Magnetocardiography (MCG), it is required to magnetically shield the SQUID from those effects, as brain and heart signals are extremely weak. The common method used to 'protect' SQUID is by surrounding SQUID with one or more shields made from a high permeability material such as permalloy (nickel-iron alloy). Unlike electricity, magnetic fields cannot be blocked or isolated, and shielding of SQUID can be done by re-routing the magnetic fields. Since magnetic shield material consists of high magnetic permeability, magnetic field tends to flow along this material, avoiding the objects
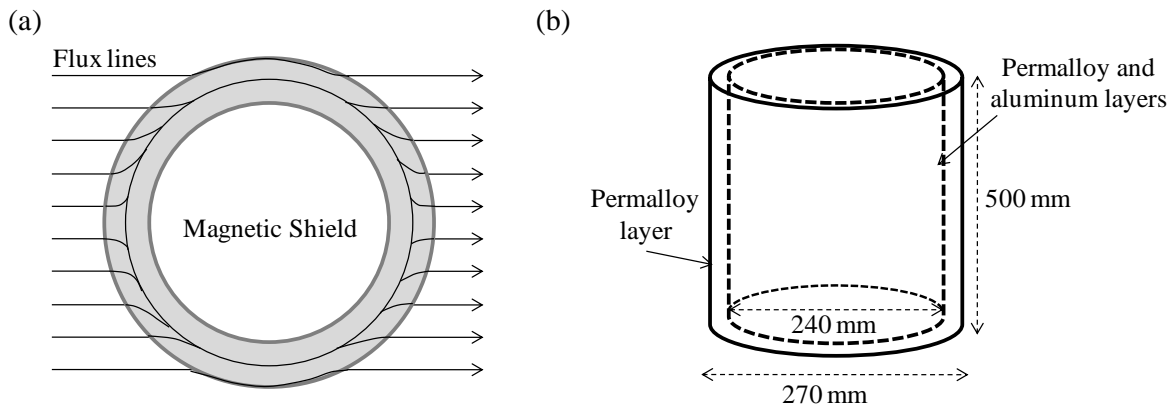
Fig. 3.1.3. Magnetic shield: (a) shielding effect, (b) design of magnetic shield.

inside. This can be illustrated in Fig. 3.1.3 (a). Therefore, the amount of magnetic fields entering inside the shield can be largely decreased. The shielding effect can be improved by increasing the thickness of the shield, however, the weight and the size of shield will increase rapidly. Instead of increasing the thickness, by making multi-layer shield, same shielding effect can be achieved. Besides that, the magnetic permeability can be improved further by annealing process. In the commercial magnetometer systems composing of low-T_c SQUIDs and superconducting magnets, low-T_c superconducting layers are employed to shield the SQUIDs. This method utilizes the perfect diamagnetism of the type I superconductor (Meissner effect) where the external magnetic fields are being opposed by the magnetic fields generated from the induced superconducting currents. However, in the liquid N_2 system where type II superconductors are used, the type II superconducting shields may introduce additional flux noises to the SQUIDs due to flux creeping and jumping at the shield layers and this will limit the SQUIDs operation and sensitivity. Besides magnetic shielding, it is also crucial to make sure the SQUIDs are rf (radio frequency) tight from environmental rf noise. The sources of rf noise can be resulted from mobile cellular signal to power line interferences, ranging from a few tens Hz to MHz order. These rf noises will decrease the flux-voltage transfer function of the SQUIDs and in the worst case, the SQUIDs cannot be operated due to

31

the transfer function is completely buried in the rf noises. The common way to shield SQUIDs from rf noises is by using Faraday cage where the SQUIDs are placed within a metal box or cage. This shielding mechanism is based on eddy current effect that, electrical currents are induced to oppose the penetrating fluxes when high frequency electromagnetic waves enter the metal box. Due to this reason, aluminum is commonly used as rf shield due to its high electrical conductivity (i.e., high electrical conductivity will result in greater eddy currents to cancel out the penetrating fluxes).

In this study, a double layer closed cylindrical magnetic shield, made of permalloy material and aluminum sheets with a thickness of 1 mm, was designed and employed. This double layer shield was divided to inner layer and outer layer. The inner layer was constructed from two layers of permalloy and aluminum sheets and the outer layer was from one layer of permalloy sheet. The aluminum layer was employed in order to provide shielding from electromagnetic wave. The inner layer diameter, outer layer diameter, and height of the magnetic shield were 240 mm, 270 mm, and 500 mm, respectively.

3.2 Electromagnet

The electromagnet employed in this study had a circular measurement region of 40 mm in diameter. The distance between its poles was 25 mm, and it was designed to generate up to 300 mT using a primary excitation coil. Its overall dimensions were 210 mm $\times$ 260 mm $\times$ 290 mm as shown in Fig. 3.2.1 (a). A Hall Effect sensor (Honeywell SS94A) was used to measure the z-component of magnetic field between the poles of the electromagnet. A linear function between current fed to the DC magnet and magnetic field strength was obtained as shown in Fig.3.2.1 (b).
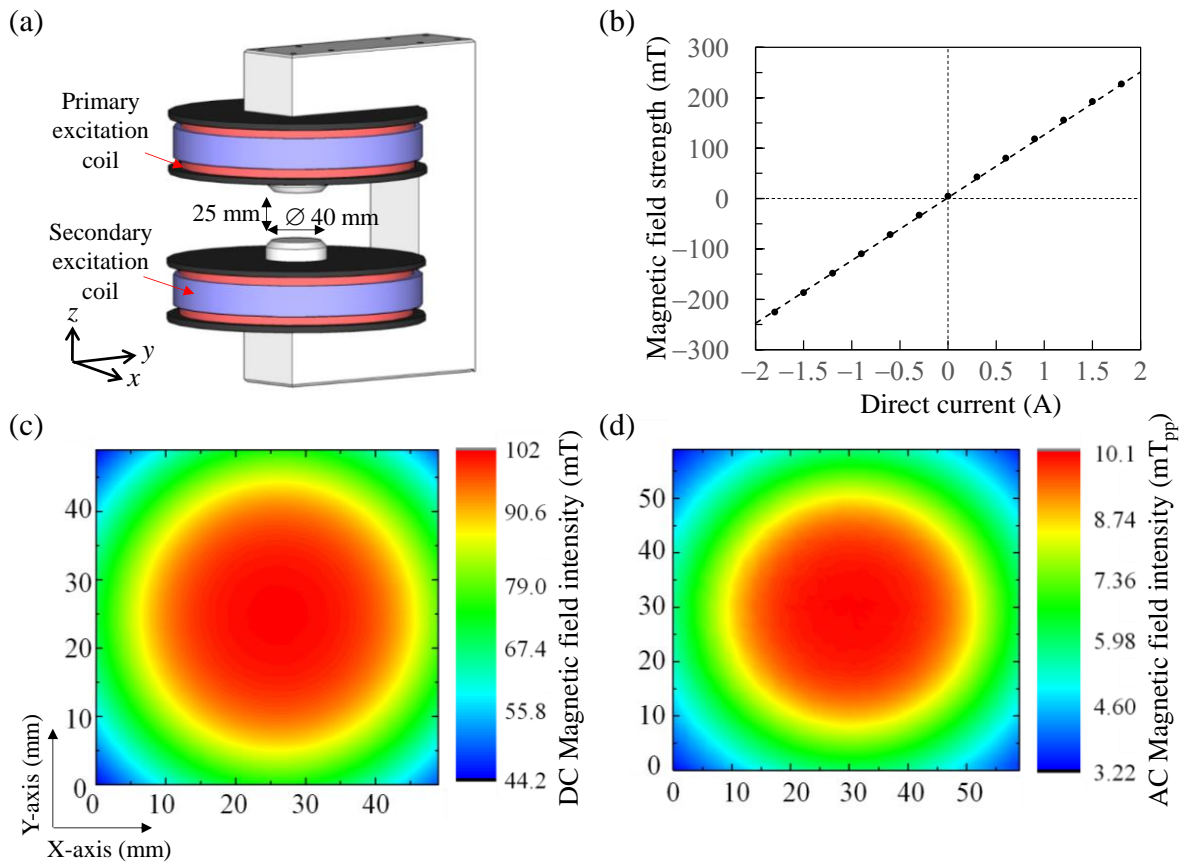
Fig. 3.2.1. (a) Schematic figure of the electromagnet. (b) Characteristic of generated magnetic field with respect to supplied direct current. (c) Distribution of *z*-component DC magnetic field in *xy*-plane. (d) Distribution of *z*-component AC magnetic field in *xy*-plane.

Fig.3.2.1 (c) shows the distribution of DC magnetic field when 0.79 A of direct current was fed to the electromagnet. The magnetic field distribution was measured in 50×50 mm^2 area between pole pieces with 1-mm interval. The measurement plane was at the center between the poles gap in the *z*-direction. It was shown that a uniform magnetic field could be obtained within 30-mm diameter in *xy*-plane and it is sufficient for a 30 mm $\times$ 30 mm sample to make measurements in this area. The center area of the pole pieces can be preferable place for measurements as magnetic field non-uniformities, if exist, can be relatively small. Fig.3.2.1 (d) shows the distribution of AC magnetic field when 10 mT$_{pp}$ of 5 Hz AC magnetic field with an offset of 100 mT of DC magnetic field was applied.
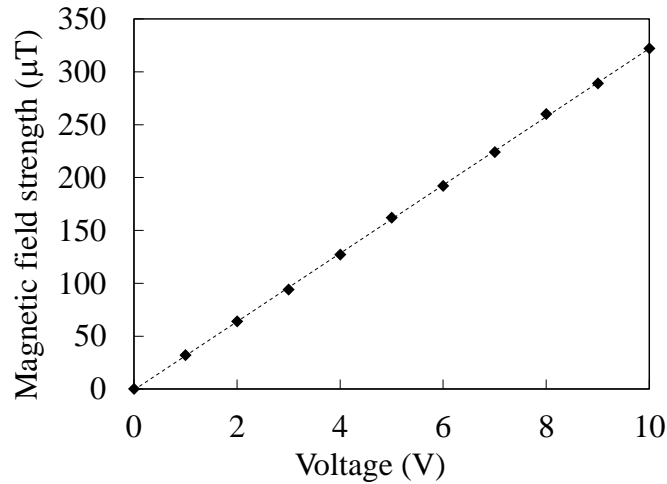
Fig. 3.2.2. Magnetic field generated by the secondary excitation coil with respect to applied voltage at the function generator.

.

It was shown that a uniform AC magnetic field could be obtained within 30 mm diameter in *xy*-plane when measuring AC responses of samples.

A wide range of magnetic field strength could be obtained by using the primary excitation coil that was integrated in the design of the electromagnet. However, the magnetic field resolution depends on the resolution of the supplied current and the number of turns in the excitation coil. However, since the primary excitation coil contained a large number of turns which might result to a lower resolution of the magnetic field, the resolution was improved by using a secondary excitation coil method. A 20-turn secondary excitation coil was fabricated on the outside layer of the primary excitation coil as shown in Fig.3.2.1 (a). A function generator was used as the current source for the secondary excitation coil in order to obtain a high resolution current. The characteristic of the generated magnetic field with respect to the applied voltage at the function generator is shown in Fig. 3.2.2.

To prevent the generated magnetic field from drifting and to obtain a high resolution of magnetic field from both excitation coils, a digital feedback system was developed. Both excitation coils were controlled by a computer and the generated magnetic field was
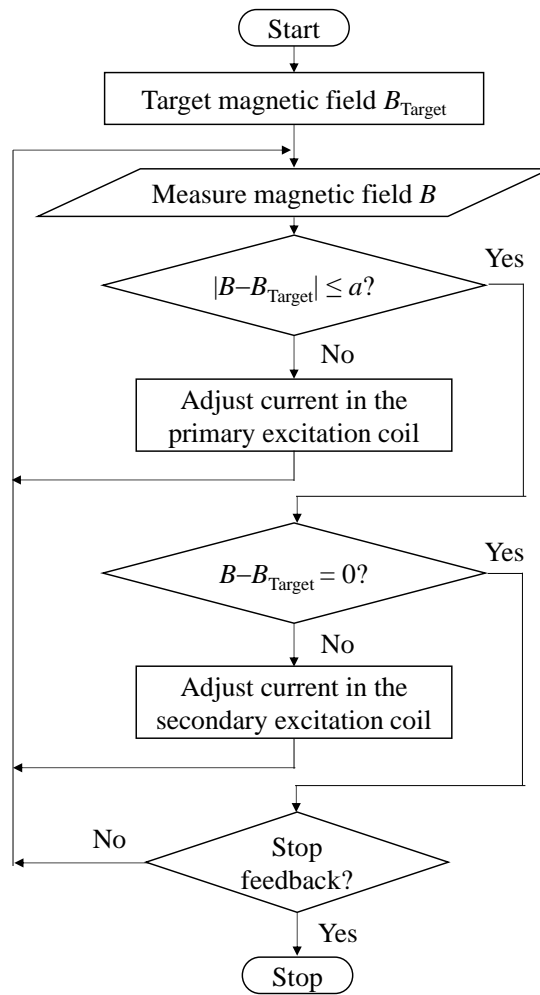
Fig. 3.2.3. Flowchart of the feedback program of the excitation magnetic field system.

monitored using a program coded in Labview. The feedback system enabled an automation

control of excitation magnetic field system with a fast sweep of target values. The flowchart

of the feedback program is shown in Fig. 3.2.3, where a represents the maximum resolution

of magnetic field generated from the primary excitation coil and this value was determined

experimentally. The sweeping characteristic of the generated magnetic field from the

excitation coils is shown in Fig. 3.2.4. By using the feedback system which controlled both

excitation coils, a wide range and stable excitation magnetic field could be achieved with a

resolution of 40 μT. For a comparison, the magnetic field resolution of the conventional
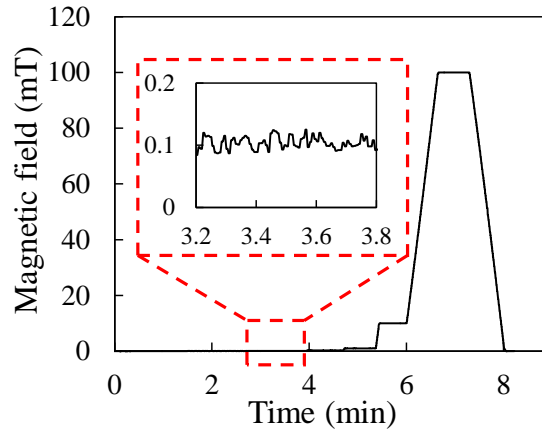
Fig. 3.2.4. Sweeping characteristic of the induced magnetic field controlled by the feedback system.

magnetometers is approximately 30 µT. Further improvements in the performance of the excitation magnetic field system can be expected by using a superior current source and feedback system.

3.3 Moving Stage

A compact linear step-up actuator was employed in order to move the sample. This computer controlled actuator was driven by DC 24 volts power. A computer was used to execute commands to a controller and the controller output pulse signals to operate the actuator. The linear motion of the actuator is based on trapezoidal velocity profile with s-curve profile so that the motion is smooth with reduced jerk motion. Using this setting, the mechanical vibrations and tears can be reduced thus prolongs the lifespan of the actuator. The displacement of the motion equation with respect to the time t including jerk parameter j can be expressed as [37]

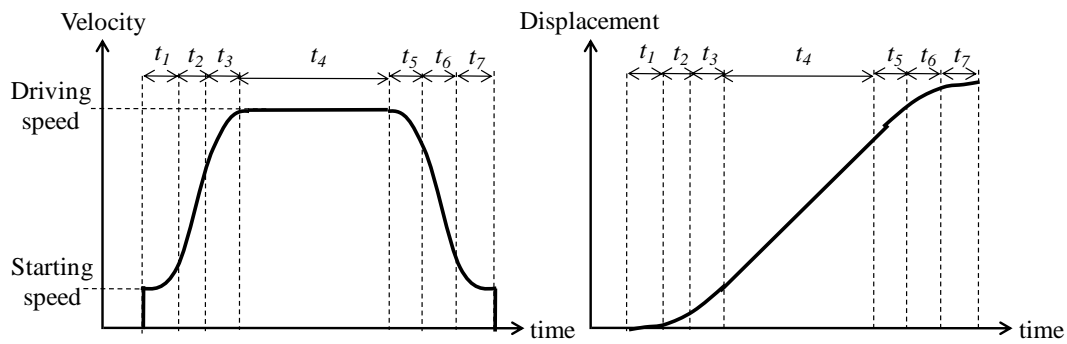$$x = x_0 + vt + \frac{1}{2}at^2 + \frac{1}{6}jt^3, \tag{3.3.1}$$

36

Fig. 3.3.1 S-curve motion profile for the actuator.

where x_0 is initial position, v is the driving speed, and a is the acceleration/deceleration. The jerk parameter j is the first derivative of the acceleration and its value determines how fast the acceleration changes. The velocity profile of the s-curve motion is shown in the Fig. 3.3.1 for zero initial position. The motion of the actuator is divided into 7 periods for a linear motion, and for each period, different pulses corresponded to motion speed are calculated and sent to the actuator. The drive speed can be varied depending on the setting. The size of actuator was given by 140 mm × 60 mm × 90 mm and the actuator could provide up to 0.004 mm of resolution. The sample was coupled to the actuator by acrylic plate with thickness of 1 mm and the distance between the sample and the actuator was 290 mm. The actuator was fixed on a stage with adjustable height.

The sample is vibrated by reciprocating the s-curve motion. The vibration frequency of the sample primarily depends on the actuator drive speed. Moreover, the SQUID output is significantly related to the rate of flux change at the detection coil based on the induction method. This means that if the sample moves in a sinusoidal manner, the vibration frequency and vibration amplitude are the main factors governing the induced voltage at the detection coil. Moreover, the waveform characteristic of the induced voltage is also influenced by the gradient characteristic of the planar differential coil. In the case where the sample is vibrated
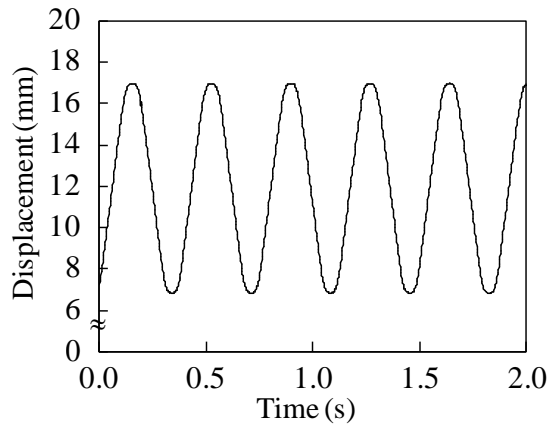
37

Fig. 3.3.2. Movement of actuator with an estimated vibration frequency of 2.67 Hz.

on top of the first order differential coil, the induced sinusoidal-like voltage of the first-order planar differential coil may become distorted when the sample vibration displacement overlaps both identical coils. The additional voltage is induced at the adjacent identical coil with reverse polarity, producing a distortion of the waveform of the total output. Therefore, the vibration displacement should be set to less than 17 mm so that a sinusoidal-like voltage output can be achieved when the sample is vibrated in a sinusoidal motion. For an initial value during this work, the vibration displacement was set at 10 mm because the effective area of the coil is approximately given by its internal diameter. The displacement characteristic of the actuator measured by the laser-positioning sensor is shown in Fig. 3.3.2. The actuator starting speed, driving speed, and acceleration/deceleration were 0.8 mm/s, 80 mm/s, and 0.4 mm/s^2, respectively. These were the manufacturer's recommended settings for the current actuator; a superior actuator could be used to achieve a higher vibration frequency.

3.4 Noise Characteristic and Sensitivity

Noise due to vibration should be treated carefully in the vibrating-sample system. The spurious background signal, which is related to motion-induced noise, has the same frequency as the sample signal and will affect the precision of measurements. To reduce mechanical coupling between the ancillary equipment, independent shock-mounting bases for each system were employed, and the detection coil was clamped to the pole face of the electromagnet. Fig. 3.4.1 (a) shows the sensitivity calibration curve of the detection system response with respect to the applied AC magnetic field frequency. The output response of the detection unit was calibrated with the known sensitivity of a magnetoresistive sensor (MR; Honeywell HMC2003). The calibration was performed by uniformly applying the same magnetic field to a circular coil and the MR sensor at different frequencies.

Environmental noise may become a major factor in limiting the sensitivity of a measurement. It is informative to compare magnetic field signal from the sample with the environmental noise. The magnetic noise characteristic of the detection unit was evaluated
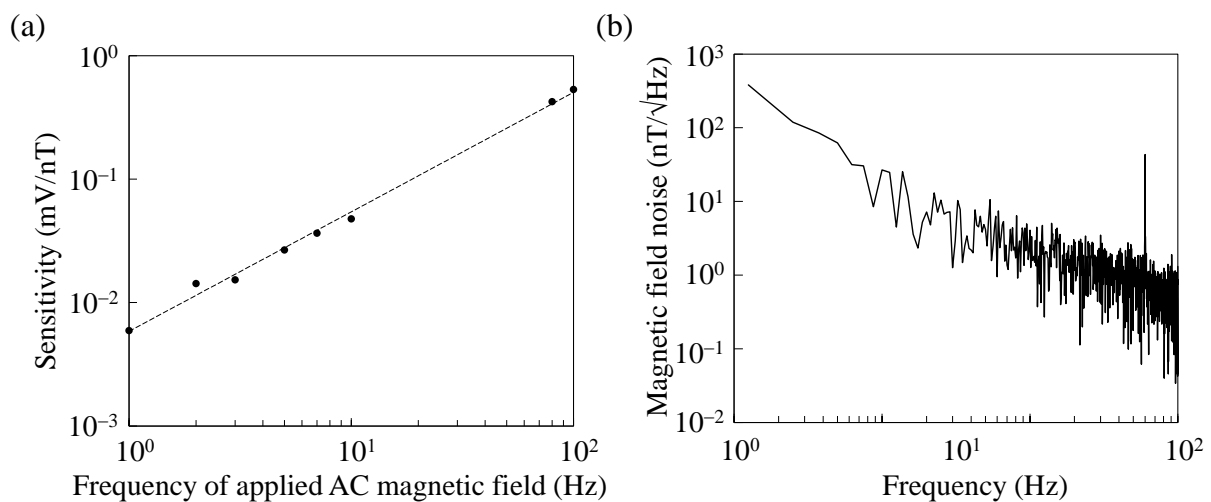

Fig. 3.4.1. (a) Sensitivity response of the detection system with respect to the frequency of the applied signal. (b) Noise characteristic of the developed system in the presence of DC magnetic field.

during exposure of a 63-mT DC magnetic field to the detection coil. The noise characteristic is shown in Fig. 4.1.2 (b). The spectrum output of detection unit was analyzed by a spectrum analyzer. The measurement range was between 0.1 Hz to 100 Hz. A higher magnetic field resolution and a lower noise characteristic could be achieved at a higher frequency of vibration from the so-called $1/f$ noise characteristic. A spectral component at 60 Hz (power line interference) could be observed clearly. At 2.7 Hz, an approximate noise of 6 nT/$\sqrt{\text{Hz}}$ could be expected.

3.5 Detection Frequency and Trigger Circuit

A test sample was prepared by uniformly dispersing Fe_3O_4 powder in a polystyrene polymer in order to investigate the characteristic of the motion-induced signal. The weight ratio of the Fe_3O_4 powder was of 4.7 wt%. The granular materials of polystyrene polymer were dissolved in acetone and then mixed with the iron oxide powder. The crystal structure of the iron oxide powder observed by a scanning electron microscope (SEM) is shown in Fig. 3.5.1 (b). The mean size of the particles was approximately determined to be 0.4 μm. The mixture then was heated gradually to vaporize the excessive acetone, hot-pressed and gradually cooled to room temperature. The magnetic characteristic of the prepared composite was evaluated by a commercial low-T_c SQUID magnetometer (Quantum Design, MPMS SQUID VSM) and the result is shown in Fig. 3.5.1 (a). The composite showed a small hysteresis and ferromagnetic property. The composite was machined to 26 mm $\times$ 26 mm $\times$ 7 mm with a mass of 5.043 g and enclosed in a measurement case whose external dimensions were 30 mm $\times$ 30 mm $\times$ 19 mm.

The estimated vibration frequency was calculated as 2.67 Hz from the aforementioned parameters of the actuator. Using the test sample, the induced signal during
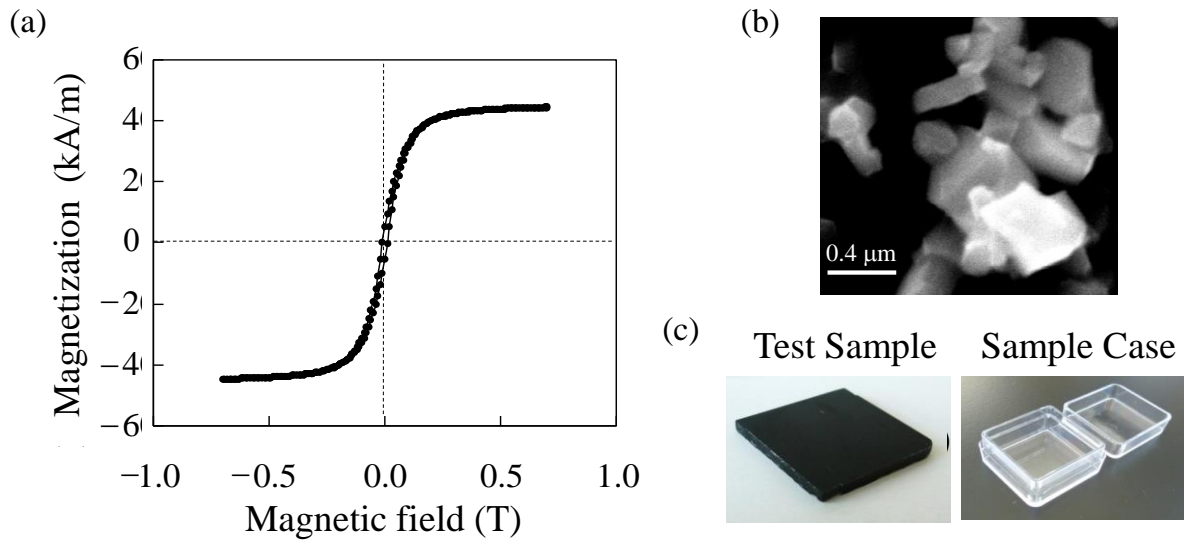
Fig. 3.5.1. (a) Magnetic property of the standard sample. (b) SEM image of the iron oxide powder. (c) Prepared test sample and sample case.

sample vibration was lock-in detected at different reference frequencies. The internal lock-in amplifier oscillator was used as the reference signal for detection. The test sample was placed such that the relative distance R, which is the maximum distance between the front edge of the case and the center of the first-order differential coil, was 17 mm by considering the direction from the coil center to the sample to be positive [Fig. 3.6.1 (a)]. The maximum and minimum positions of the front edge of the case were given when the values of the relative distance R were 17 and 7 mm, respectively. The applied field, vibration cycles, vibration amplitude, and lift-off were set to 12 mT, 50 cycles, 5 mm, and 1 mm, respectively. A peak was obtained at 2.693 Hz and considered to be the optimal parameter for the detection frequency (Fig. 3.5.2). Using the sensitivity calibration curve, the peak at 2.693 Hz corresponds to 15 μV/nT.

Basically, the amplitude of sample signals can be detected by a lock-in amplifier utilizing an independent internal oscillator as a reference. However, the phase information of the detected signals cannot be exploited, making the discrimination of the magnetic property,
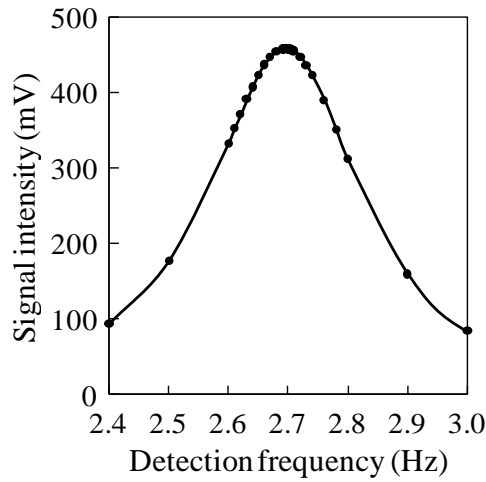
Fig. 3.5.2. Frequency dependence of the detected signal.

e.g., paramagnetism or diamagnetism, to be difficult. In the case of vibrating-sample systems where the sample movement is homologous to the waveform of the induced signal, the sample displacement can be synchronized with the detected signals for signal detection. It was possible to directly use the output of the laser-positioning sensor as the reference signal; however, the output signals of the sensor used in this study contained a small amount of noise where this noise might affect the precision in the lock-in technique. Moreover, a sharp change
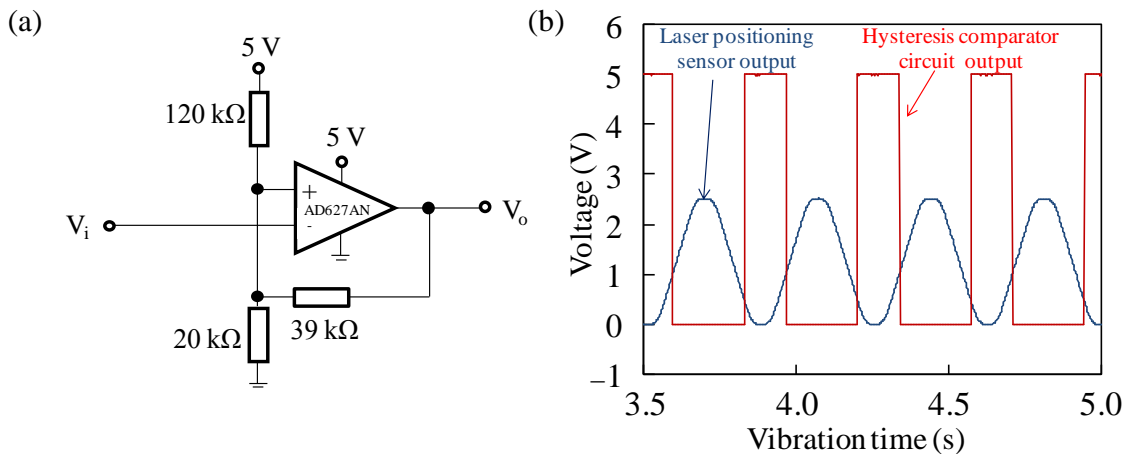
Fig. 3.5.3. (a) Circuit diagram of the hysteresis comparator circuit. (b) Triggering characteristic of the circuit with respect to the laser-positioning sensor output.

in the reference signal is desirable for a precise detection at the lock-in amplifier. To achieve synchronization between the moving mechanism and detection unit and high SNR detection, the output of the laser-positioning sensor was converted to TTL wave signals by a hysteresis comparator circuit and the TTL signal was used as the reference signal at the lock-in detection technique. The design and triggering characteristic of the circuit is shown in Fig. 3.5.3, and by using the precise triggered TTL signal, the frequency of the vibrating sample was determined to be 2.693 Hz, which was same in the case of using the independent oscillator as the source of the reference signal.

3.6 Dependence of Sample Position

The sample position relative to the pickup coil affects the strength of the detected signal. To examine this effect, the detected signal strength was measured with respect to distance R. The arrangement of the detection coil relative to the test sample is shown in Fig. 3.6.1 (a). The vibration displacement was fixed at 10 mm, while the relative distance R was varied. The strength of the detected signal reached a minimum when R = 5 mm and a maximum peak when R = 13 mm [Fig. 3.6.1 (b)]. This result demonstrates that the differential coil is very sensitive when fluxes change within the internal diameter of the identical coil. The signal strength was at a minimum when the sample was vibrated at the center of the differential coil due to the distorted waveform of the sample signal having a small spectral component at the fundamental vibration frequency.

The lift-off effect of the sample to the detection coil was also investigated. Theoretically, a wider lift-off will produce a smaller signal because of the decrease in coupled fluxes at the pickup coil. The sample lift-off effect to the detected signal is shown in Fig. 3.6.1 (c). The detected signal gradually decreased with increasing lift-off.
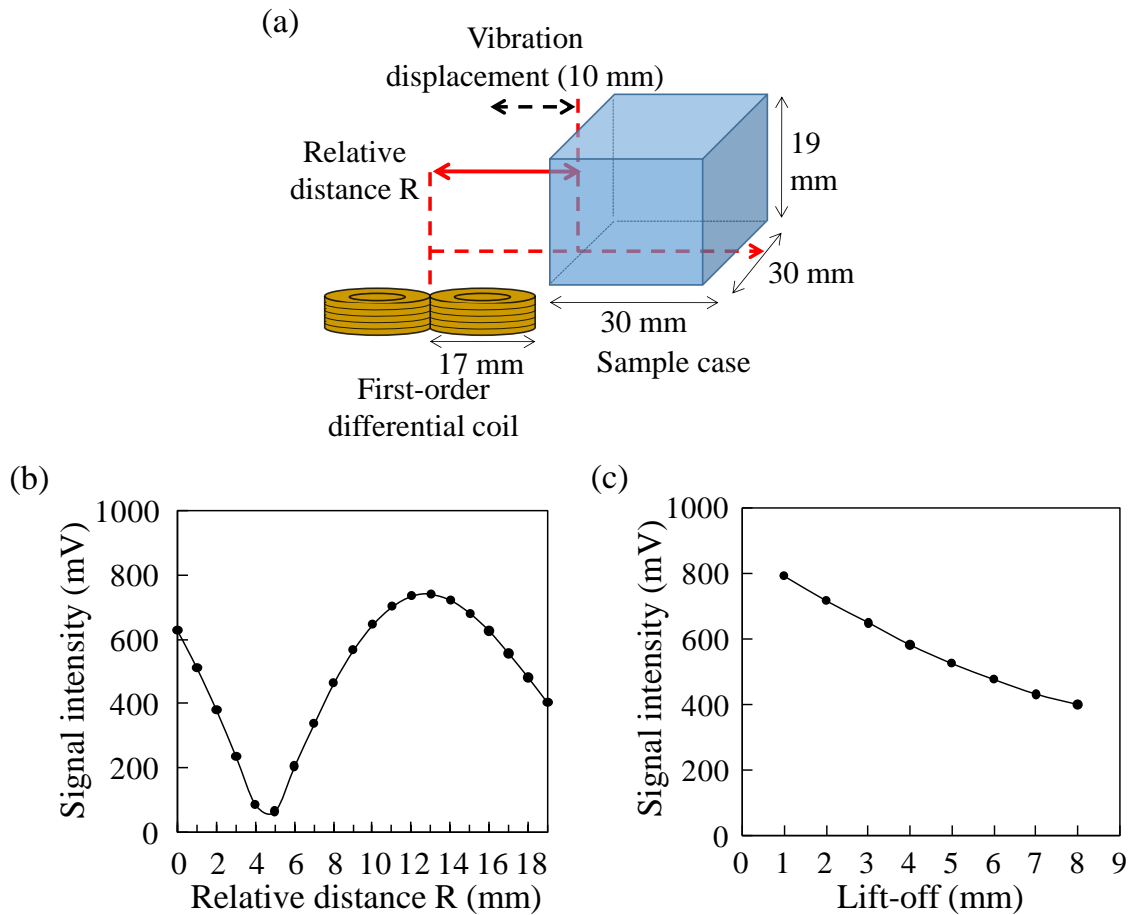
Fig. 3.6.1. (a) Schematic figure of the sample position relative to the pickup coil. (b) Dependence of the obtained signal strength with respect to the relative distance R. (c) Lift-off effect of the sample to the signal strength.

3.7 Dependence of Sample Shape

To clarify the shape dependence of measurement samples with respect to the detected signal, the magnetic field response of water in different sizes of sample cases was measured. The different sample cases were made by varying the diameter and height of cylindrical cases (Fig. 3.7.1). 5 different cylindrical cases with diameters ranging from 10 to 30 mm in 5 mm intervals with the same height of 20 mm, and 4 different cylindrical cases with height
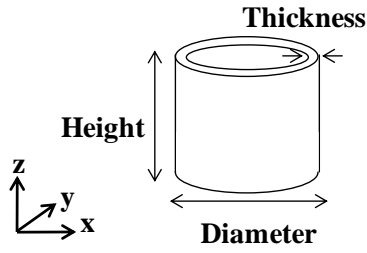
Fig. 3.7.1. Cylindrical case for investigation of sample shape.

Table 3.7. Parameters of the cylindrical cases.

Case	I	II	III	IV	V	VI	VII	VIII
Diameter (mm)	10	15	20	25	30	20	20	20
Height (mm)	20	20	20	20	20	10	15	25
Thickness (mm)	1.6	1.6	1.7	2	2	1.7	1.7	1.7

ranging from 10 to 25 mm in 5 mm intervals with the same diameter of 20 mm were prepared
as shown in Table 3.7. The cases were positioned so that the axis of the cylindrical case was
parallel to the direction of the applied magnetic field. The applied magnetic field was fixed at
63 mT, and measurement was conducted under optimized parameters. For the different case
diameters, the obtained signal started to saturate at the case diameter of approximately 18 mm
[Fig.3.7.2 (a)], suggesting that the quantity of flux changes in the detection coil became
constant when the sample was larger than the identical coils. Fig.3.7.2 (b) shows the result for
different case height. The detected signals increased slightly with respect to the height, except
when the case height was 25 mm, which might result from experimental error. From this, it
can be concluded that the detected signals were significantly related to case diameter
compared to case height for the developed system.

Simulations were also carried out in order to investigate the sample shape
dependence using water as the sample. A large number of water molecules that is contained
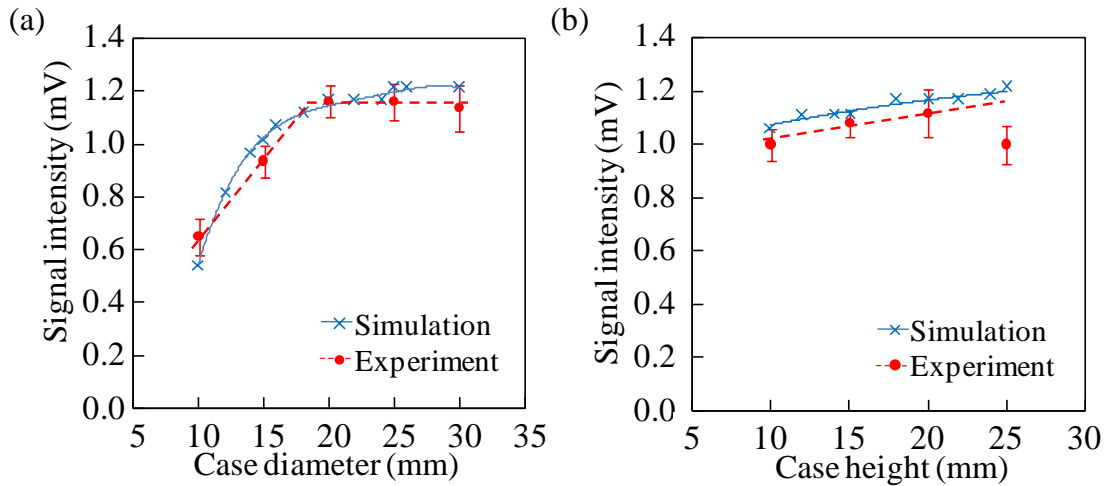
Fig. 3.7.2. Experimental and simulation results for different sizes of cylindrical cases. (a) Height of all cylindrical cases was fixed at 20 mm. (b) Diameter of all cylindrical cases was fixed at 20 mm.

in a region with high concentration can be represented as an accumulation of atomic magnets. By considering a pole model, the magnetic moment of these atomic magnets can be expressed as $m = Q_m L$, where m is the magnetic dipole moment in volume V, Q_m is the pole strength per area of the magnet, and L is the pole separation of the magnet [38]. It must be noted that to precisely express the atomic magnets in the pole model, the size of the magnet should be small in comparison to the distance at which the magnetic field is observed so that individual magnetic field effect of each atomic magnet can be neglected. When a uniform magnetic field is applied to water, these atomic magnets can be assumed to be oriented in the magnetization direction and uniformly distributed. The poles of these atomic magnets face the adjacent magnets with opposite polarities, thus cancelling each other's effects everywhere except at the top and bottom surfaces. Although the atomic magnetics expressed by the magnetic dipole moments have a discrete and finite size, it is convenient to assume that water exhibits continuous magnetization. This assumption should lead to no appreciable error for volumes that contain a vast number of magnetic dipole moments. From this, the magnetic field of water can be represented as the magnetic fields generated by the
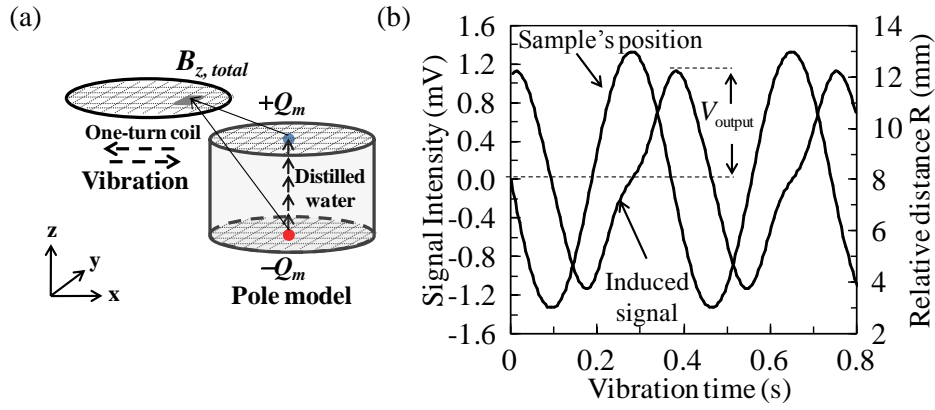
Fig. 3.7.3. (a) Schematic arrangement of one-turn coil and sample. (b) Sample position relative to the center of the differential coil, and the calculated signal intensity for a 20-mm diameter and 20-mm height of cylindrical case.

equivalently superficial magnetic charge Q_m at the top and bottom of circular surfaces. The top surface has positive magnetic charges while the bottom surface has negative magnetic charges. When the two surfaces come closer which is equivalent to decrease in sample volume, the cancellation effect between charges at top and bottom surfaces increases to reduce the apparent magnetic field. When the surface area is increased which is equivalent to increase of numbers of magnetic charges, the quantity of the generated magnetic fluxes is increased. The experimental conditions were simulated by uniformly scattering the magnetic charges $+Q_m$ and $-Q_m$ in a 1-mm-spaced grid at top and bottom surfaces as shown in Fig. 3.7.3 (a). The x- and y-components of the magnetic field generated by the magnetic charges were ignored because the sensitive axis of the pickup coil was in the z-direction. The z-component of the magnetic field B_z (x,y,z) generated by a magnetic charge $Q_m(x',y',z')$ is given by

$$B_z(x, y, z, x', y', z') = \frac{\mu_0}{4\pi} Q_m \frac{z - z'}{((x - x')^2 + (y - y')^2 + (z - z')^2)^{3/2}}, \quad (3.7.1)$$

where μ_0 is the vacuum permeability. The value of Q_m can be determined by

47

$$Q_m = \chi_{water} \cdot H \cdot S \,, \tag{3.7.2}$$

where χ_{water} is the suscepibility of water, H is the applied magnetic field, and S is the unit area of 1 mm^2. The magnetic field resulting from a magnetic charge $+Q_m(x',y',z/2')$ at the top surface and a magnetic charge $-Q_m(x',y',-z'/2)$ at the bottom surface is expressed by

$$B_{z,total}(x,y,z,x',y',z') = B_{z,top}(x,y,z,x',y',z'/2) - \\ B_{z,bottom}(x,y,z,x',y',-z'/2) \,. \tag{3.7.3}$$

Here, the sample case radius is given by $(x'^2+y'^2)^{1/2}$ with the case height of z'. The sample case is centered at the origin and its axis is in the z-direction. In the case where the sample is small in comparison to the size of the detection coil, the sample can be treated as a point-like magnet and equation (3.7.3) can be simplified to

$$B_z(x,y,z,x',y',z') = \frac{\mu_0}{4\pi} Q_m^{total} L \frac{2(z-z')^2 - (x-x')^2 - (y-y')^2}{((x-x')^2 + (y-y')^2 + (z-z')^2)^{5/2}} \,, \tag{3.7.4}$$

where Q_m^{total} is the total magnetic charge at surface, L is the magnet length, and the total magnetic moment m is given by $Q_m^{total}L$. In this investigation, the simulation is further simplified by vibrating the detection coil in the x-direction instead of the sample. There is no difference in either method because the ubiquitous magnetic field in the simulation is from the magnetic charges only. Furthermore, the calculation time in the simulation can be significantly reduced by calculating the flux changes in a simple one-turn coil instead of a multiple-turn first-order differential coil because of two reasons. First, the effect of the fluxes penetrating the adjacent coil can be considered small because the sample overlaps only one coil and the magnetic field from the sample decreases proportionally with the distance. Second, a rough estimation is sufficient whereas the calculation in the multiple-turn coil provides a more precise result in expense of a great increase in calculation time because the

matrix calculation method is used [39]. Under these considerations, the total flux penetrating the one-turn coil at a given time can be expressed as

$$\Phi(t) = \sum_{x,y,z} \sum_{x',y',z'} B_{z,total}(x, y, z, x', y', z') \cdot Q(x, y, z, t) \ , \tag{3.7.5}$$

where

$$Q(x, y, z, t) = \begin{array}{l} 1 \quad \text{for } \left[x - (A\sin 2\pi ft + c)\right]^2 + y^2 \leq r^2 \\ 0 \quad \text{for } \left[x - (A\sin 2\pi ft + c)\right]^2 + y^2 > r^2 \end{array}, \tag{3.7.6}$$

which represents the $B_{z,total}$ integration area of 1 mm^2 at the vibrating coil. Here x and y, r, A, f, and c are the position of the integration area in the xy-plane, coil radius, vibration amplitude, vibration frequency, and offset resulting from the relative distance of the coil and sample, respectively. By numerically substituting and varying the time to mimic the vibration of a magnetized sample, the induced voltage V_{output} of the detection unit can be expressed as

$$V_{output} = \frac{\left.\dfrac{\overline{\Delta\Phi}}{\Delta t}\right|_{max}}{\sqrt{2} \cdot S \cdot 2\pi f} \cdot a, \tag{3.7.7}$$

where a is the sensitivity of the detection unit at the vibration frequency, and S is the area for the mean radius of the identical circular coil. To precisely express a multi-turn coil with a one-turn coil, the effective coil diameter and lift-off to the sample must be determined. After several simulation runs with different parameters of coil diameter and lift-off to the sample, 13.8 mm and 1 mm were selected as the effective coil diameter and lift-off, respectively. The raw waveform of the induced signal for 20 mm of diameter and height of case is shown in Fig. 3.7.3 (b). The waveform shows distortion when the coil at the farthest position from the case (R = 13 mm). At this position, the overlapping area is small and resulting the rapid decrease of the flux changes. A comparison to the experimental results were carried out by simulating the effect of the water volume in different case sizes over the detected signal using this model.

49

The results of the selected coil parameters are shown in Fig. 3.7.2. The simulation results could be considered to agree well with the graph shape of the experimental results. The approximations of various parameters might cause the simulation results to exhibit outputs slightly different that those obtained by experimental results. From the simulation and experimental results, the detected signals in the developed system were significantly related to the case diameter in comparison to the case height. The detected signals saturated as the dimensions of the sample case exceeded 20 mm in diameter and 10 mm in height. As a result, the error resulting from the dependency of the sample shape could be reduced by using sample cases with case diameter ranging from 20 mm to 30 mm and the height ranging from 10 mm to 25 mm.

3.8 System Evaluation

The developed system was evaluated by the measurement of the magnetic field response of the test sample and purified water contained in 30 mm × 30 mm × 19 mm cases under optimized parameters. The excitation magnetic field during the measurement of water sample was set to 63 mT. For the measurement of the test sample, a 12 mT DC magnetic field was applied. The signal induced by the test sample was used as the reference for the phase information of the water's signal. The strength of the detected signals and their phases are shown in Fig. 3.8. A maximum fluctuation of 0.15 mV in the water's signal was observed. This value is equivalent to 10 nT and represents the lowest field resolution of the developed system. Considering this as the detection limit of the developed system, the precision in susceptibility can be estimated by comparing the signal equivalent to the volume susceptibility of water, -9.1×10^{-6} SI [7.2×10^{-7} emu (dimensionless)], which is observed to be 1×10^{-7} emu (dimensionless) at 63 mT. The diamagnetism of water could be confirmed as
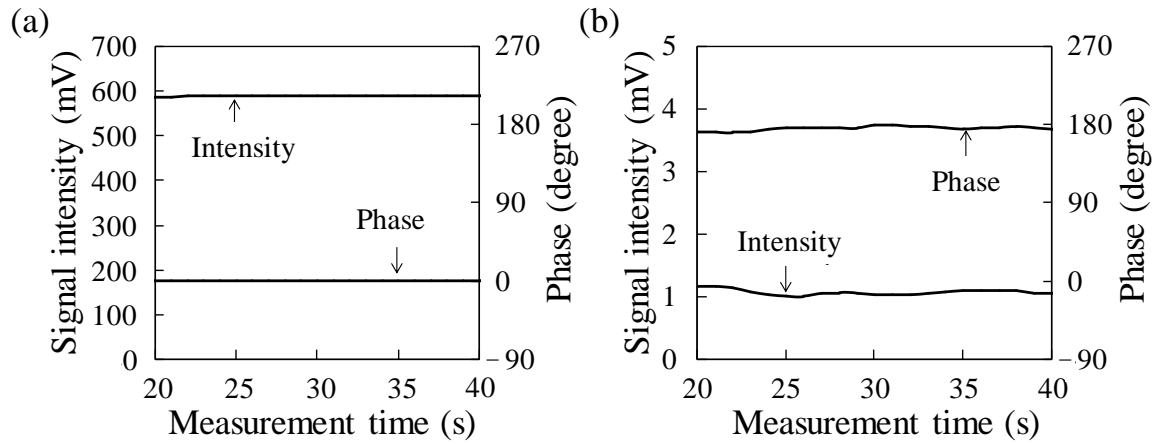
Fig. 3.8. Detected signals' strength and their phase information during measurements of (a) standard sample and (b) purified water.

the water's signal was 180° out of phase to the signal of the test sample. From this, a highly sensitive evaluation of magnetic property can be expected by using the developed system.

CHAPTER 4: OPTIMIZATION OF DETECTION TECHNIQUE

4.1 Overview

Sensitivity in conventional magnetometer systems using induction coils is mainly limited by the thermal noise and $1/f$ noise of the used induction coils, and motion-induced noise due to the mechanical vibration. In the latter problem, a few techniques have been reported to reduce the motion induced noise through isolation of the detection frequency from the vibration frequency [40], [41]. In these techniques, the frequency of a sample-generated signal is doubled by utilizing the output characteristic of the induction coils. Sensitivity of a vibrating-sample magnetometer system utilizing an induction coil can be improved by methods such as increase of vibration frequency and optimization in induction coil designs. In the former case, the sensitivity is enhanced because the signal-to-noise ratio (SNR) of an induction coil is proportional to the frequency where a signal is modulated. However, since the spatial modulation of signal consists of vibrating a sample mechanically, mechanical limitation in a vibrating system imposes a limit in the achievable vibration frequency. A rather complex vibrating system may be required in order to achieve a high vibration frequency. Furthermore, the difficulty in increasing vibration frequency is also increased when the vibration motion requires a large stroke of displacement such as in the developed system, resulting in a high acceleration is applied to a sample. In the latter, many studies have been performed to optimize the design of normal induction pickup coils for vibrating-sample magnetometers and SQUID-based magnetometers [7], [21], [42].

To improve the sensitivity in the developed system, a few considerations on the design of the detection coil and detection technique were carried out. Since a planar differential coil configuration was adopted in the developed system, the intrinsic gradient

characteristic of the detection coil could be utilized to reduce the outlined problems. Optimization of the detection coil for a harmonic detection had been investigated and implemented in the developed system to increase the sensitivity. In this chapter, optimizations of the detection coil and the detection technique are presented.

4.2 Magnetic Field Noise

When a sample is exposed to an external magnetic field, the sample is magnetized and generates a secondary magnetic field. In the vibrating-sample magnetometers where the induction coils are employed, the detection coils cannot detect the static secondary magnetic field where they respond only to the time-variant magnetic fields according to Faraday's induction law. In order to sense this static secondary magnetic field, the secondary magnetic field must be modulated at a certain frequency by changing the position of the detection coils or the sample. As the modulation frequency is increased, the induced voltage increases so as the SNR. This is equal to the reduction of magnetic field noise at higher frequency and by modulating the secondary magnetic field at high frequency, sensitivity of the developed system can be improved. The voltage induced when applying the magnetic field B_s to the pickup (detection) coil is $V_s = n_p\omega B_s\pi r_p^2$ and this will result in the flowing of signal current I_s at the input coil [21]. Here, ω is the angular frequency of the magnetic field, n_p is the number of turns, and r_p is the radius of the pickup coil. Since the SQUID is magnetically coupled to the input coil by mutual inductance M, I_s introduces magnetic flux $\phi_s = MI_s$ to the SQUID. The relation between ϕ_s and B_s can be expressed as

$$\phi_s \approx \frac{MV_s}{\sqrt{\left(R_i + R_p\right)^2 + \left(\omega L_p\right)^2}} = \frac{Mn_p\omega\pi r_p^2 B_s}{\sqrt{R^2 + \left(\omega L_p\right)^2}},$$ (4.2.1)

by assuming that the inductance of input coil L_i is negligible compared to pickup coil inductance L_p, and R is the total resistance of input coil R_i and pickup coil R_p. Due to the noise contribution in this system is given by thermal noise of the resistance from the flux transformer and the SQUID itself, the flux noise at the SQUID is given by

$$S_\phi^{1/2} = \left(\frac{4k_b TRM^2}{R^2 + (\omega L)^2} + S_{\phi,sq} \right)^{1/2}, \qquad (4.2.2)$$

where k_b is the Boltzmann's constant, and T is the absolute temperature. Therefore, the magnetic field noise in this system without circumstance noise can be expressed as

$$S_B^{1/2} = \frac{S_\phi^{1/2} \left(R^2 + (\omega L_p)^2 \right)^{1/2}}{\omega n_p \pi r_p^2 M}. \qquad (4.2.3)$$

From this, it means that the sensitivity of the developed system is limited by the noise of the detection coil at low frequencies. The measured noise characteristic of the developed system during exposure of DC magnetic field to the detection coil is shown in Fig. 3.4.1 (b) where improvement in the noise level can be achieved at higher frequencies. By taking advantage of the gradient characteristic of the first-order planar differential coil, the sensitivity can be further improved using the harmonic detection technique. This technique is very similar to reference [40], but incorporates a different system arrangement in which the sample size is comparable to the size of the pickup coil.

4.3 Harmonic Detection Technique

In the early detection technique of the developed system, the sample was vibrated on top of one coil of the first-order differential coil with the other identical coil acting as a reference coil. The vibration direction was parallel to the baseline of the first-order differential coil.
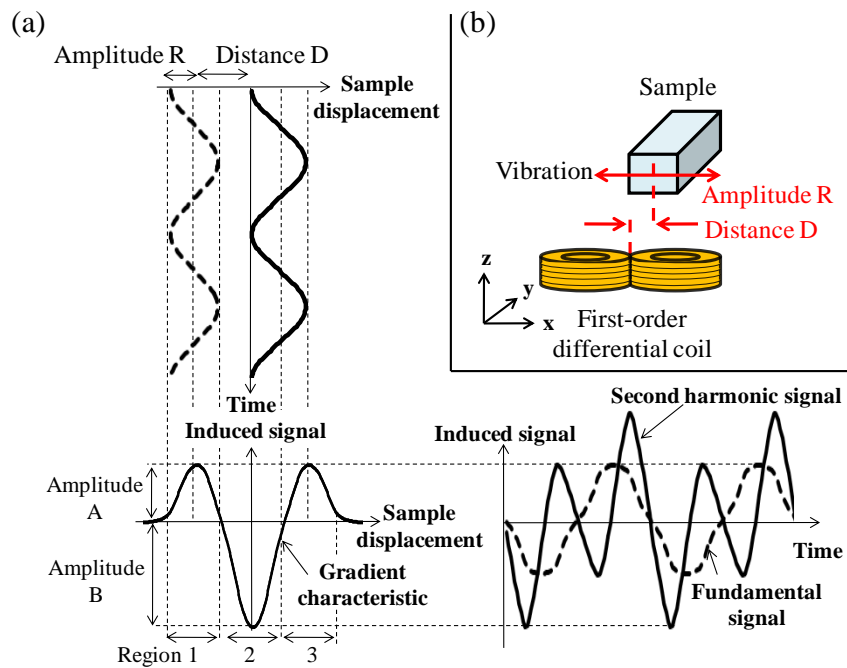
Fig. 4.3.1. (a) Measurement principle of the harmonic detection technique. (b) Schematic arrangement of the sample and first-order differential coil.

The induced signal was detected at a vibration frequency such that the fundamental component of the induced signal was the largest. With the harmonic detection technique, the sample is vibrated between the positive and negative parts of the gradient characteristic of the first-order differential coil, i.e., on top of the two identical coils. The induced waveform of the signal is closely related to the gradient characteristic of the pickup coil. Here, the second harmonic component of the induced signal is large compared to the fundamental component. By detecting the induced signal at the second harmonic frequency, the noise level in the detection frequency band can be lowered, thus increasing the sensitivity of the developed system. Fig. 4.3.1 shows the arrangement of the sample and first-order differential coil with respect to the induced waveforms of the signals. For a sample whose size is comparable to the external diameter of the one identical coil, when the sample is vibrated with amplitude R within region 1, 2, or 3, the fundamental component will be the largest. By shifting distance D, which is the distance between the center of the first-order differential coil and the center of

vibration, and vibrating the sample between region 2 and 3, the second harmonic signal will be generated. The amplitude of the second harmonic signal can be roughly estimated by the mean value of amplitude A and B. It should be noted that the induced waveform is greatly affected by the gradient characteristic of the coils, amplitude R, and distance D. To maximize the signal intensity of the second harmonic component, the gradient characteristic must be optimized so that the SNR can be further increased. Moreover, the dependence of harmonic components on amplitude R and distance D must also be investigated to obtain their optimum parameters.

4.4 Fabrication of First-order Differential Coils

The output characteristic of the first-order differential coil depends on the geometry of the sample and the first-order differential coil. To optimize the gradient characteristic, the dependence of the induced signal on the shape of the sample and the pickup coil was investigated using a simulation method explained in the next section. Different shapes of first-order differential coils using different sizes of samples were moved in linear motion with a constant velocity along the baseline of the first-order differential coil to find the dependency on them. As a result, by setting a sample width that is parallel to the baseline, almost the same as the baseline length, amplitude B of the gradient characteristic (see Fig. 4.4.1) can be maximized to twice the value of amplitude A. Moreover, the gradient characteristic was also improved by using the first-order differential coil that is fabricated from elliptical coils compared to circular coils. The elliptical coils have advantages in terms of a larger flux change rate in which the intensity of the induced signal increases, and a smaller baseline length where a high gradient characteristic and smaller amplitude of vibration can be achieved. For a comparison to the previous circular first-order differential
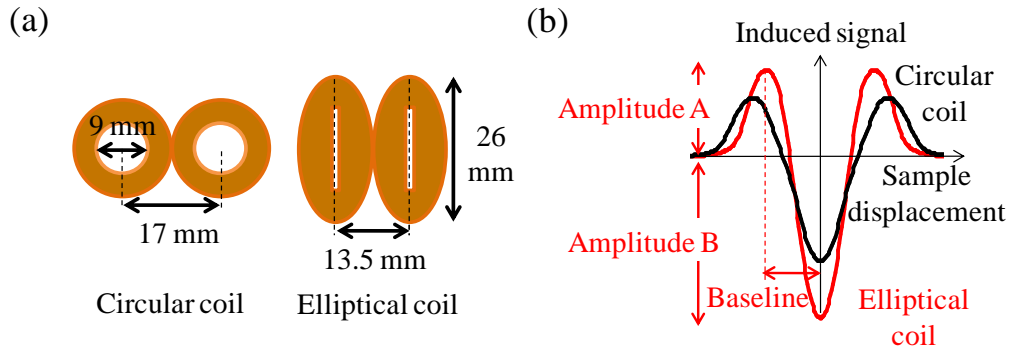
56

Fig. 4.4.1. (a) Fabricated two types of first-order differential coils. (b) Simulated signal response of both coils when a linear-motion sample is moved above them.
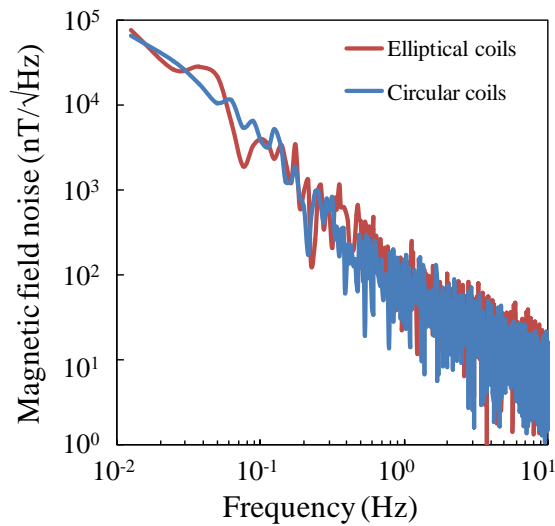
Fig. 4.4.2. Measured magnetic field noise of circular and elliptical coils during exposure of 40-mT magnetic field.

coil, a first-order differential coil of elliptical coils was designed and fabricated with comparable effective area and magnetic field noise using equation (4.2.1) [21]. Both the circular and elliptical coils had same 200 turns for one coil. For one circular coil, its external and internal diameters, length, resistance, and inductance were 17 mm, 9 mm, 5 mm, 2.08 Ω, and 446.2 µH, respectively. For one elliptical coil, its external major and minor axes, internal major and minor axes, length, resistance, and inductance were 26 mm, 13.5 mm, 15 mm, 1.5 mm, 3.9 mm, 2.99 Ω, and 451.6 µH, respectively. Both coils were wound using

0.32-mm-diameter copper wires. The measured magnetic field noise of both coils is shown in the Fig. 4.4.2 where they showed almost similar magnetic field noise in a low frequency region.

A ferromagnetic test sample was prepared for the investigation by uniformly dispersing 1 wt% of Fe_3O_4 in a polystyrene polymer. Its size was 10 mm × 30 mm × 3 mm with a mass of 0.871 g.

4.5 Simulation on Harmonic Components

As a preliminary investigation and comparison of the harmonic components induced by the elliptical and circular coils, their dependence on amplitude R and distance D was calculated using a pole model explained in chapter 3.7. In this case both identical coils of the first order differential coil will contribute to the generated signals due to the movement of the sample, so that signals induced by both identical coils must be calculated. Given the contribution of both identical coil, the total fluxes penetrating the area of the first-order differential at given time t can be calculated by

$$\phi(t) = \sum_{x+f(t),\, y} B_z(x + f(t), y, k)\Delta(x + f(t))\Delta y - \sum_{x+L+f(t),\, y} B_z(x + L + f(t), y, k)\Delta(x + L + f(t))\Delta y\,, \tag{4.5.1}$$

where L is the baseline length of the first-order differential coil, k is the lift-off of the sample, and $f(t)$ is the displacement function of the first-order differential coil. Note that the total fluxes are the difference of fluxes penetrating both identical coils due to their series-opposing connection. Therefore, the induced signal which is proportional to the rate of flux change can be determined by numerically substituting time t.

The basic motion of an actuator is based on a trapezoidal motion profile where its linear displacement can be separated into three periods of time intervals, involving acceleration, displacement with constant velocity, and finally deceleration [37]. A linear displacement of the actuator can be expressed as

$$g(t)=\begin{cases} 0.5at^2 & (0 \leq t < t_1) \\ v\cdot(t-t_1)+0.5at_1^2 & (t_1 \leq t < t_2), \\ v\cdot(t-t_2)-0.5at^2 + v\cdot(t_2-t_1)+0.5at_1^2 & (t_2 \leq t < t_3) \end{cases} \qquad (4.5.2)$$

where a is the acceleration and v is the constant driving velocity of the actuator. Here, the intervals of $0 \leq t < t_1$, $t_1 \leq t < t_2$, and $t_2 \leq t < t_3$ are the periods for acceleration, displacement with constant velocity, and deceleration of the actuator, respectively. The interval length between t_1 and t_2 changes with respect to the displacement of the actuator as v and a are constant. The vibration motion with amplitude R for the actuator can be achieved by reciprocating the linear displacement and can be expressed as

$$f(t) = \left(g\left(t-t_3 \cdot \left\lfloor \frac{t}{t_3} \right\rfloor \right) - \frac{R}{2} \right)\cdot(-1)^{\left\lfloor \frac{t}{t_3} \right\rfloor} \qquad (0 \leq t < \infty), \qquad (4.5.3)$$

where $\lfloor t \rfloor$ is the floor function of t.

Vibration amplitude R and distance D were varied to investigate their effect on the induced harmonic components. The sample width, which was 10 mm, was set parallel to the baseline of the first-order differential coils. The driving velocity of the actuator was 100 mm/s. Amplitude R and distance D were varied from between 4 mm and 15 mm, and between 0 mm and 10 mm, respectively. The lift-off of the sample was 2 mm. To reduce calculation time, one-turn first-order differential coil of both types was used in the simulation. The dimensions of a one-turn coil were given by the external dimensions of both coils. The time-variant waveform of the flux change rate was calculated using equation (4.5.1), and then

Fig. 4.5.1. (a) Schematic arrangement of the one-turn first order differential coil relative to the sample. (b) Calculated harmonic components of first-order differential coils.

analyzed using fast Fourier transform (FFT) analysis for each of the waveforms, respectively. Finally, the magnitude of harmonic components resulted from FFT analysis was normalized with a maximum value of the overall harmonic components to achieve a better comparison. The simulation results are shown in Fig. 4.5.1 for fundamental, second harmonic and third harmonic components. The fundamental components for both coils showed a peak at small R and D, and then decreased with increments of R and D. The fundamental component had a normalized peak of 0.62 at R = 5 mm and D = 0 mm for the circular coils, and a normalized peak of 1 at R = 5 mm and D = 0 mm for the elliptical coils. The second harmonic component

increased with a decrease in the fundamental component and had a normalized peak of 0.49 at R =12 mm and D = 7 mm for the circular coils, and a normalized peak of 0.82 at R = 10 mm and D = 6 mm for the elliptical coils. The third harmonic component had a normalized peak of 0.39 for the circular coils, and 0.75 for the elliptical coils at R = 15 mm and D = 0 mm. This preliminary result showed that the harmonic components were improved using elliptical coils.

4.6 Measurement of Harmonic Components

To further investigate the dependence on amplitude R and distance D, the harmonic components induced by circular and elliptical coils were measured using the developed system. The applied field was 40 mT and the other parameters were the same as in the simulation. The harmonic components were measured with respect to differing amplitudes R and distances D using the lock-in technique. The experiment results are shown in Fig. 4.6.1. The fundamental component had a peak of 65.8 mV at R = 6 mm and D = 0 mm for the circular coils, and a peak of 102.8 mV at R = 5 mm and D = 0 mm for the elliptical coils. Then, the fundamental component decreased with increments of R and D. The second harmonic component increased with an increment in distance D and had a peak of 60.5 mV at R =12 mm and D = 6 mm for the circular coils, and a peak of 87.8 mV at R = 10 mm and D = 6 mm for the elliptical coils. The third harmonic component had a maximum peak of 48.9 mV for the circular coils, and 86.7 mV for the elliptical coils at R = 15 mm and D = 0 mm. The comparison of simulation and experimental results is shown in Fig. 4.6.2.

The simulation and the experimental results agreed well, with approximately similar contours and positions of peaks for all harmonic components. The signal intensity of the
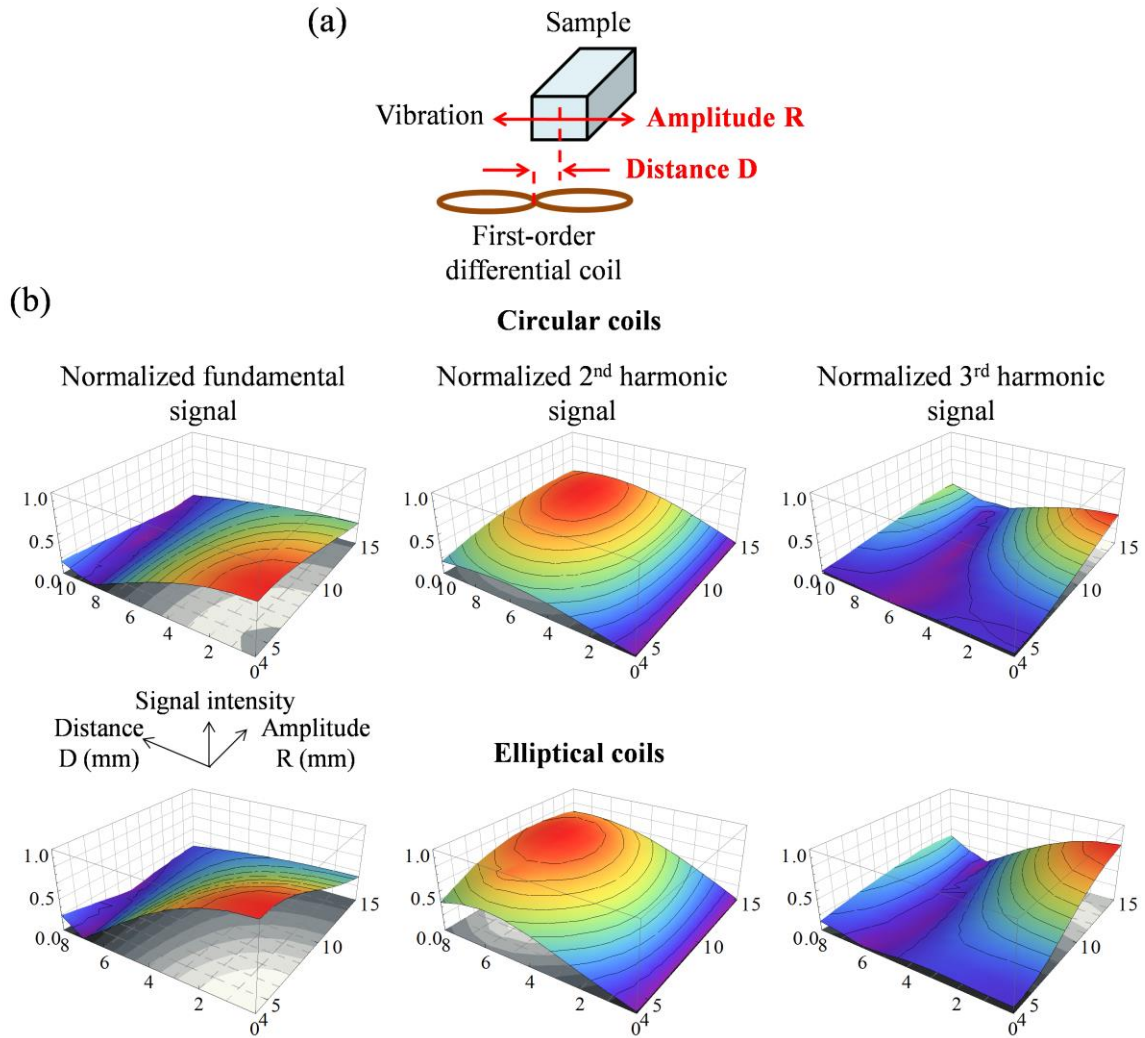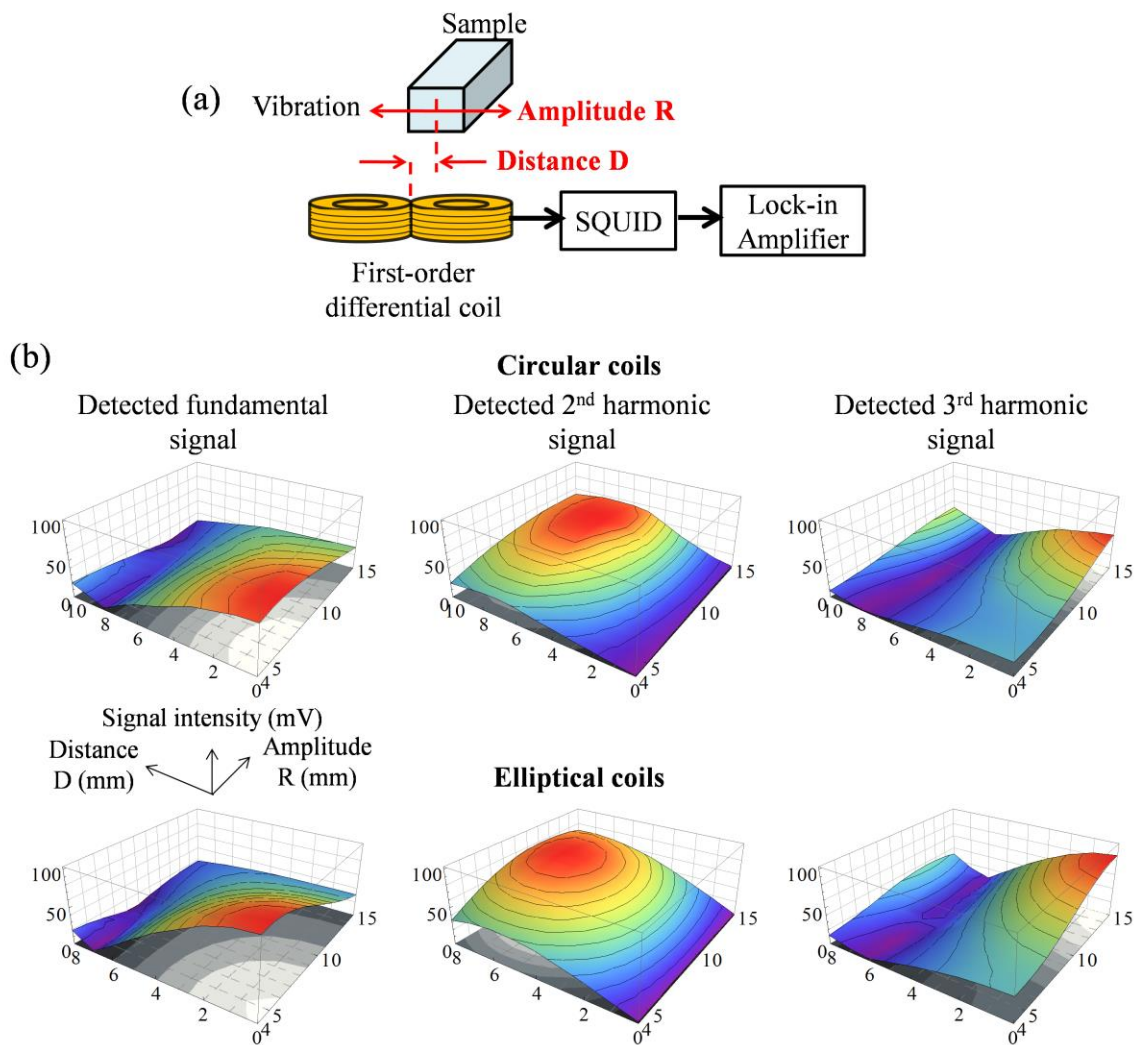
Fig. 4.6.1. (a) Schematic arrangement of the fabricated first order differential coil relative to the sample. (b) Measured harmonic components of first-order differential coils.

harmonic components was improved using the elliptical coils in comparison with the circular coils. When the sample was vibrated within region 1, 2 or 3 (see Fig. 4.3.1) with small amplitudes, the fundamental signal was larger compared to others harmonic components. The others harmonic components existed due to s-curve motion of the sample (impure sine motion) and the non-linear distortion of the gradient characteristic. As amplitude R was increased, the third harmonic component increased in smaller distance D region due to the fact that the sample movement with large amplitude R covered all regions of the gradient
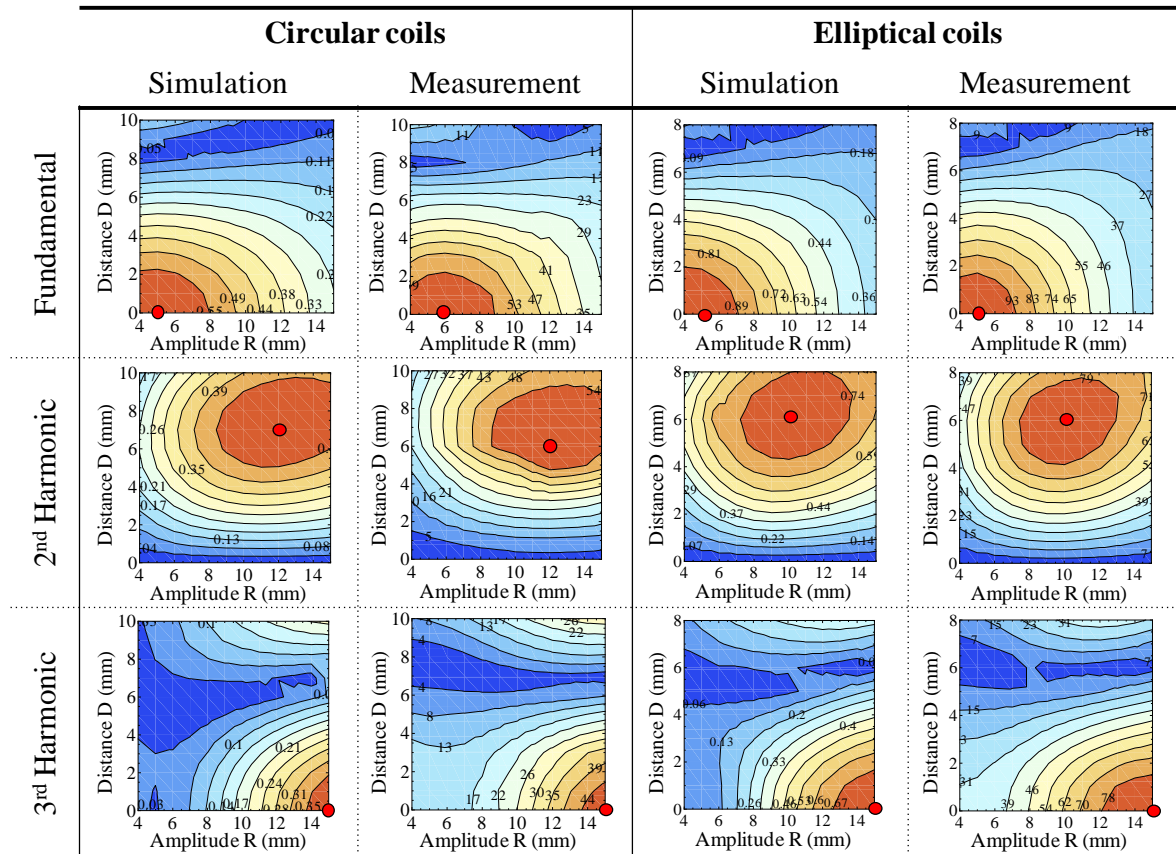
Fig. 4.6.2. Contour maps for simulation and experimental results. Red circles show the position of the peaks.

characteristic (2 peaks and 1 trough) resulting in the dominance of the third harmonic components. However, compared to simulation results where the third harmonic components were relatively small at the region of small distance D and amplitude R, the experimental results showed relatively large signal intensity in this region. This difference between simulation and experimental results could be caused by the simplification of one-turn first-order differential coils in the simulation; the fabricated first-order differential coils were consisted of multi-turn coils with different diameter and baseline, in which the third harmonic components were generated at high-order number of turns. The second harmonic components increased and became dominant when distance D was increased. The changing polarity of the

signals due to the gradient characteristic in this region contributed to the modulation of the signals at the second harmonic components. Moreover, amplitude R at the peak for the second harmonic component of the elliptical coils was smaller compared to the case of the circular coils. This result reflects the characteristic of the baseline in which the elliptical coils had a shorter baseline length. For a constant driving velocity of vibration systems, a smaller vibration amplitude will result in an increment in vibration frequency, thus further improving the SNR of vibrating-sample magnetometers.

Although the second and third harmonic signals for the elliptical coils was 1.17 and 1.19 times smaller compared to the fundamental signal, the noise level was improved approximately from 32 nT/$\sqrt{}$ Hz at the fundamental frequency of vibration to 23 nT/$\sqrt{}$ Hz at the second harmonic frequency of vibration, and 21 nT/$\sqrt{}$ Hz at the third harmonic frequency of vibration. This resulted in 1.2 times and 1.3 times of improvement in SNR for the second harmonic detection and the third harmonic detection, respectively, in comparison to the fundamental signal detection. As a comparison to the previous detection technique where the sample was vibrated within region 1 (see Fig. 4.3.1 (a)) using the circular coils, the harmonic detection technique with the elliptical coils improved SNR by greater than 3 times. As shown in section 6.3, the sensitivity of the developed measurement system using elliptical coils was calibrated with a low-T_c SQUID susceptometer (Quantum Design, MPMS) by measuring the magnetization curve of a same MnF_2 sample. A sensitivity of 3×10^{-10} Am^2 at the fundamental frequency (2.8 Hz) was shown. It should be noted that in the developed system, a low vibration frequency of a few Hz was used and the vibration frequency was related to the vibration amplitude. By using a more superior vibration system, the reduction in noise level as well as improvement in SNR can be expected. A higher vibration frequency will intensify the potential of this method and effectiveness of the SQUID amplification.

CHAPTER 5: INTEGRATION OF AC/DC DETECTION COIL

5.1 Overview

Dynamic magnetization (AC susceptibility) is one of the vastly utilized magnetic property in various applications besides static magnetization. In this case, AC magnetic fields are applied to a sample and its AC responses are measured with respect to frequency, amplitude and so on. In the case of a normal Cu coil is used as a detection coil, the use of AC response measurement improves the SNR (signal-to-noise ratio) and sensitivity of the detection coil easily. Moreover, a fast evaluation also can be expected in comparison to the measurement of DC susceptibility since a wide region of magnetic field can be covered by a single shot of AC magnetic field. This is beneficial in the case of routine measurements of a large number of samples. The combination of the measurement techniques of AC and DC susceptibilities in the developed measurement system will result in a more versatile magnetometer system for applications in various fields to reveal further information on magnetic properties.

Although the sensitivity of Cu coil is improved in the case of AC susceptibility measurement, a highly sensitive measurement is difficult to achieve due to the interference of the excitation magnetic field. When a large excitation AC magnetic field is applied to the detection coil, the dynamic of the excitation magnetic field is also sensed by the detection coil and transferred to the SQUID, resulting in a large offset signal of interference. In this case, the usable dynamic range of a SQUID system is reduced substantially and may hinder a proper operation of the SQUID. Moreover, the ability to resolve a small magnetic response may become difficult under this large offset signal and this will limit the sensitivity of AC measurement technique. The cancelling of the interference can be performed using mechanical and electronic methods [5]. In the mechanical method system, the sensitive axis

is aligned to be off-axis from the magnetization direction to obtain higher cancelling rate by reducing the coupling between the excitation magnetic field and the coil. However, this configuration may interfere with the spatial alignment of the sample circumference. In the electronic method, the interference of the excitation magnetic field can be regarded as an in-phase noise and by adding an in-phase signal electronically or magnetically to the detection system, the interference of the excitation magnetic field can be cancelled. However, this method is difficult as it requires a complex circuit. In an attempt to reduce this interference, two different cancellation techniques were applied and compared. In the first technique, the sensitive axis of the detection coil was mechanically aligned to be off-axis from the magnetization direction [43]. In the second technique, a compensation coil was used in order to reduce the remaining interference. Effectiveness of both techniques was evaluated and compared [28].

5.2 Fabrication of AC Detection Coils

The coil arrangements with respect to a sample in between the electromagnet poles are shown in Fig. 5.2.1. In the first technique as shown in Fig. 5.2.1 (a), the sensitive axis of the elliptical coils was aligned to be off-axis from the magnetization direction. Furthermore, since the environmental noise is also required to be cancelled, a first-order axial differential coil was used to improve the detection of the orthogonal component of the secondary magnetic field from the magnetized sample. Both elliptical coils sense the magnetization of the sample by utilizing the characteristic of the closed loop flux lines from the magnetized sample. The cancelling factor was optimized by manually adjusting the angle of the sensitive axis with respect to the magnetization direction. In the second technique, a compensation coil was connected in series to the first-order planar differential coil used in the DC susceptibility
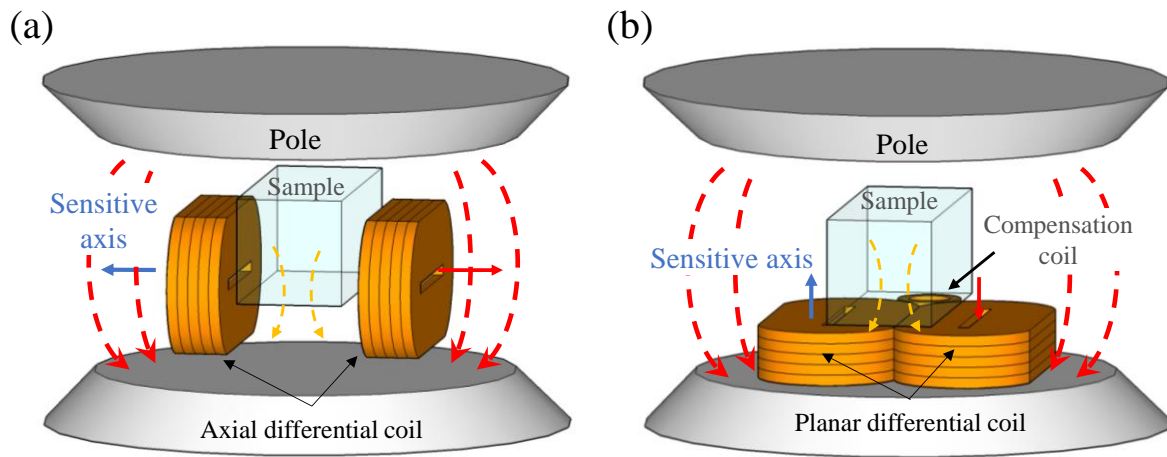
66

Fig. 5.2.1. (a) First-order axial differential coil. (b) First-order planar differential coil with compensation coil.

measurement as shown in Fig. 5.2.1 (b). The compensation coil was fabricated from a 0.32-mm Cu wire, which was same with the elliptical coils, to form a coil with 6-mm diameter. The compensation coil was used to improve the balance of the elliptical coils by cancelling the remaining interference signal during the excitation of magnetic fields. In this technique, the cancelling factor was improved by optimizing the number of turns of the compensation coil.

5.3 Characteristics of AC Detection Coils

The induced voltage V_o, of the planar differential coil with the compensation coil was measured with a lock-in amplifier during excitation of the magnetic field at 5 Hz and 80 mT_{pp}. The induced voltage V_o with respect to the number of turns is shown in Fig. 5.3.1 (a). The residual signal was reduced effectively when the number of turns was near the optimum value. Then, the SQUID was connected to the both detection coils, respectively, in order to measure the magnetic field noise. The corresponding SQUID magnetic field noises for both techniques under excitation of a magnetic field at 5 Hz and 30 mT_{pp} are shown in Fig. 5.3.1

(b). The excitation spectrum for the magnetic field in the case of the compensation coil technique was relatively small compared to the case of off-axis technique using the axial differential coil. The residual signal of interference was reduced effectively by the compensation coil method, in addition to the harmonic spectra. Further measurements using the lock-in amplifier revealed that the residual signal with the compensation coil technique was reduced by a factor of 37 to 6 μT_{pp} compared to the off-axis technique. The cancellation factor for the compensation coil and off-axis techniques were $B_{detected}/B_{applied} = 2 \times 10^{-4}$ and
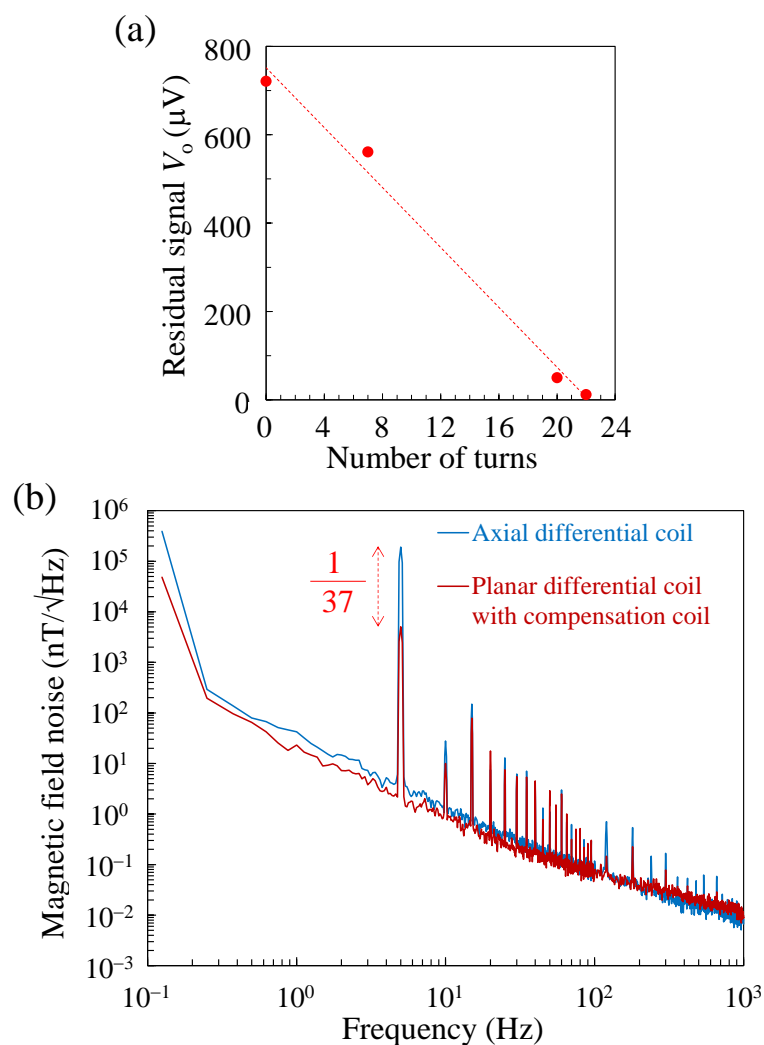

Fig. 5.3.1. (a) Residual signal in the compensation coil technique with respect to the number of turns. (b) Magnetic field noise of the SQUID connected to the axial differential coil and to the planar differential coil with the 22-turn compensation coil under an excitation magnetic field of 5 Hz and 30 mT$_{pp}$.

68

7×10^{-3}, respectively. It must be noted that in order to detect 1 nT of a magnetic response under excitation of a 10-mT magnetic field, a cancelling factor $B_{detected}/B_{applied}$ less than 10^{-3} is required.

Although the residual signal from the excitation magnetic field was reduced to some extent in the off-axis technique, a substantial reduction of the residual signal was difficult and technically challenging. This might be due to slight differences in the intrinsic characteristics and alignments of each elliptical coils. Since the axial differential coil was placed under a magnetic field gradient between the pole gap, this had resulted in a poor cancellation characteristic of the differential coil due to the orthogonal component of the magnetic field. Besides the effectiveness of the compensation coil method in reducing the interference, this technique also requires only one detection coil for both measurements of the AC and DC susceptibilities, thus reduces the spatial complexity at the sample circumference. This resulted in a compact and integrated detection unit. Increase in the coupling between the detection coil and the secondary magnetic field from the sample can be expected since the sensitive axis was parallel to the magnetization direction compared to the off-axis method. Furthermore, a same optimized sample shape can be used for both measurements of AC and DC susceptibilities by using the planar differential coil to increase the sensitivity. In the case of using different detection coils for measurements of AC and DC susceptibilities, the optimized sample shape depends on the geometry of the detection coils and the sample.

Because the sensitive axis of the compensation coil was in the direction of the magnetization and placed near to the detection coil, the effect of the compensation coil on the output characteristics of the detection coil must be clarified. A line measurement across the baseline of the detection coil was performed by applying an excitation magnetic field at 5 Hz and 10 mT$_{pp}$ to a paramagnetic MnF_2 sample to investigate this effect. The MnF_2 powder was
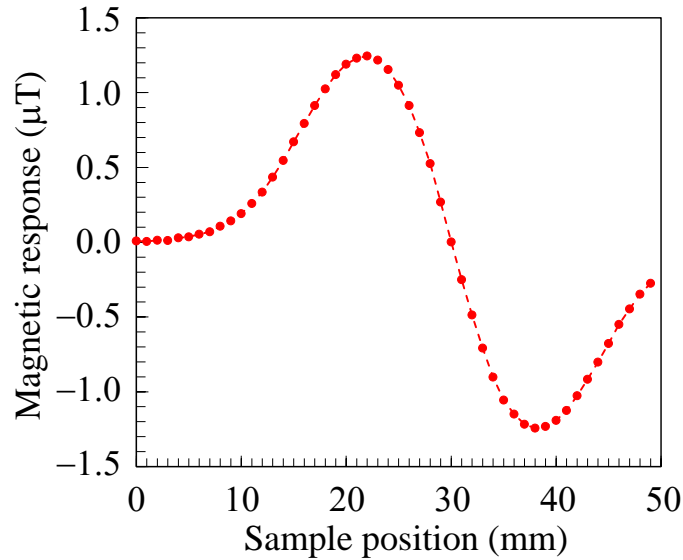
Fig. 5.3.2. Magnetic response of MnF_2 sample measured using the detection coil with a compensation coil under an excitation magnetic field of 5 Hz and 10 mT$_{pp}$.

encased in a standardized acrylic case with inner dimensions of 20 mm $\times$ 15 mm $\times$ 10 mm. Fig. 5.3.2 shows the fundamental component of AC response with respect to the position of the MnF_2 sample. The distance between the center of the planar differential coil and the center of the sample at the 0 mm position was 30 mm. The 16 mm distance between the peak and trough agreed well with the width of the MnF_2 sample. The smooth gradient characteristic of the measured magnetic response without anomalies inferred that the effect of the compensation coil on the output of the detection coil was negligible, despite the compensation coil being placed in between the elliptical coils. This result is consistent with the fact that the relatively small product of the number of turns and flux-coupling area of the compensation coil by a factor of 300 compared with one elliptical coil. The magnetic response detected by the compensation coil was relatively small compared to the elliptical coils because the size of the MnF_2 sample was larger than the compensation coil. From the fluctuation of signal in the fundamental component, the resolution of magnetic field at the excitation frequency of 5 Hz was determined to be 34 nT$_{pp}$, showing the effectiveness of the
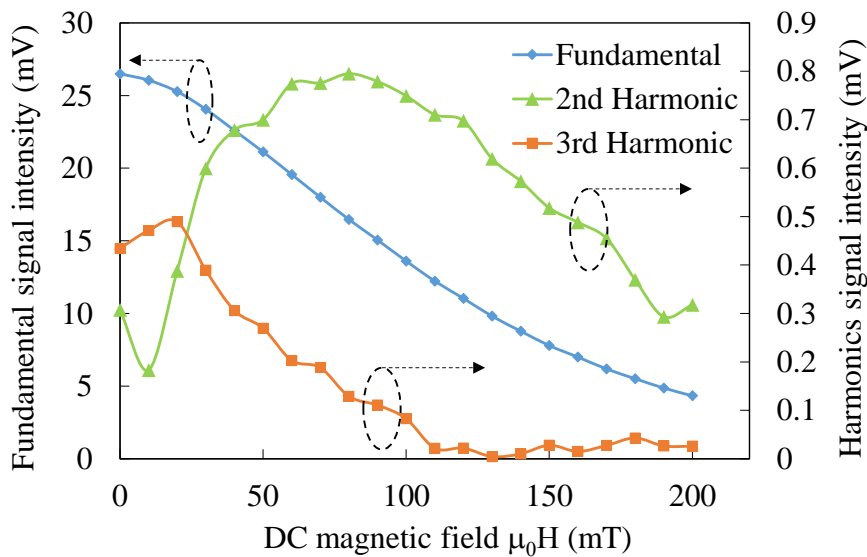
70

Fig. 5.4.1. Measured harmonic components of the test sample with respect to the offset of the DC magnetic field.

compensation coil in reducing the interference. Furthermore, improvement of the cancellation factor to the order of 10^{-5} can be expected via a finer tuned compensation coil.

5.4 Harmonics and Magnetization Curve of Ferromagnetic Test Sample

The performance of the new detection coil was assessed by performing measurements on the 1 wt% ferromagnetic test sample mentioned in section 4.4.2. The size of the test sample was 10 mm × 30 mm × 3 mm with a mass of 0.871 g. The harmonics induced from the test sample during application of AC and DC magnetic fields were measured. The amplitude of 5 Hz AC magnetic field was fixed at 30 mT_{pp} and different offsets of DC magnetic field ranging from 0 mT to 200 mT with 10 mT intervals were superimposed to the AC magnetic field. The fundamental, second and third harmonic components from the AC response were measured by using the lock-in amplifier. The harmonics induced from the sample were obtained after removing the offset signals at each harmonics by subtracting the data measured at the 0 mm position from that at the 22 mm position (see Fig. 5.3.2). The measured
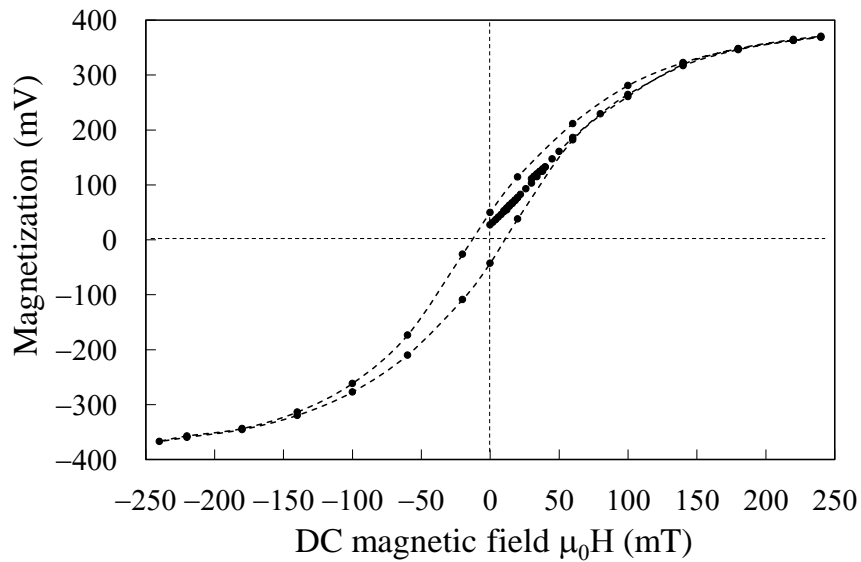
Fig. 5.4.2. Magnetization curve of the test sample

harmonics with respect to the offset of the DC magnetic field are shown in Fig. 5.4.1. The

fundamental component decreased with the increase of the DC magnetic field. However, the

second harmonic component increased to a maximum value at around 80 mT and then

decreased as the DC magnetic field increased. The third harmonic component shows similar

characteristic with the fundamental component where it decreased as the DC magnetic field

increased. To investigate the dependency of harmonic components with the DC magnetic

field, measurement of magnetization curves was performed. The induced harmonic

components can be expected to have a relation with the magnetization curve. A closed loop

of magnetization curve of the test sample is shown in Fig. 5.4.2. The magnetization curve

was measured within −250 mT to 250 mT. The ferromagnetism of the test sample could be

confirmed from the hysteresis characteristic of the magnetization curve. As shown in the

initial magnetization curve of the test sample, the slope decreased as the DC magnetic field

increased. The fundamental component reflects the first derivative of the magnetization curve,

i.e., the slope. The non-linear characteristic of the magnetization curve will reflect in higher

derivative components, i.e., higher harmonic components. Since the initial magnetization

curve started to saturate near 100 mT, the second harmonic component increased in this

72

region due to the square-wave-like response. On the other hand, the third harmonic component is related to the triangle-wave-like response, therefore, it could be thought that the third harmonic component was improved when the slope of the non-linear magnetization was high.

As a result, the compensation coil technique implemented in the detection coil had resulted in improved cancellation factor and dynamic range of the developed system. More importantly, this technique enabled a compact detection unit to be achieved without compromising spatial degree of freedom in between the pole gap and both AC and DC coils could be operable using only one SQUID.

CHAPTER 6: EVALUATION OF MOISTURE CONTENT IN MORTAR

6.1 Overview

Concrete is one of the widely used materials in the construction of modern buildings nowadays. It is composed of cement (Portland cement), water, fine aggregate (natural sand) and coarse aggregate (natural gravel). Since it is widely used, safety factor which relates to the performance of concrete used in constructions becomes extremely important parameter needed to be monitored. One of the main factors affects the mechanical properties of concrete is moisture content [44]. The ratio of water and cement determines the mechanical strength of concrete where too high or too low ratio reduces the concrete strength. Therefore, measurement of moisture content in concrete prior application is very important. The oven method is commonly used to determine moisture content. In the conventional oven method, a sample is heated to vaporize its moisture content and from the difference in weight before and after heating processes, its moisture content is derived. However, the oven method is a destructive method where the sample cannot be re-measured and time consuming. The magnetic method is more promising and offers a faster evaluation [45], [46].

When all components of concrete are mixed together, these mixture materials undergo a chemical reaction where cement hydrates to bind together fine and coarse aggregates. As the hydration process proceeds, the mixture transforms from a thixotropic fluid to a hardened state. At the early stage of the hydration process, the moisture exists as free and bound water in cement [47]. Then, the chemical reaction transforms free water to bound water at the final stage of hydration process. Since the magnetic properties are related to the chemical composition of concrete, the moisture content at the early and final state of concrete after mixing is reflected in its magnetic responses. The diamagnetic effect of water reflected in magnetization curve can

be utilized to evaluate the moisture content. Since coarse aggregate remains inactive during chemical reaction process, coarse aggregate can be excluded from cement to simplify the magnetic characterization. To evaluate the moisture content, mortar samples, which are the product of concrete without course aggregate, were prepared and their magnetization curves were measured at the early stage of hydration process.

6.2 Preparation of Mortar Samples

The mechanical properties of mortar depend on water to cement ratio; a too low ratio results in low fluidity, which is hard to work, while a too high ratio reduces its strength and causes safety issues. A weight ratio of water to total mixture between 11 wt.% to 13 wt.% is considered suitable to be used in construction generally. Standard sand (JISR5201), Portland cement and water were mixed together at different ratios to prepare a set of mortar samples. The weight ratio of Portland cement to sand was kept constant at 1:3 and the weight ratio of water to total mixture was varied from 10 wt.% to 14 wt.%. After mixing, the fresh mortar samples were inserted in acrylic cases with dimensions of 10 mm $\times$ 30 mm $\times$ 11 mm. The acrylic cases were constructed from 1-mm acrylic plates. The weight of prepared mortar samples was measured to range from 6.82 g to 7.15 g. The magnetization curves of Portland cement, water and standard sand were also measured to find their magnetic contributions in mortar.

6.3 Magnetization Curves of Mortar Samples

The moisture content in prepared mortar samples was evaluated by utilizing their magnetization curves. The magnetization curve of each sample was obtained by modulating the DC magnetization signal of a sample at 2.8 Hz under different DC magnetic fields. The
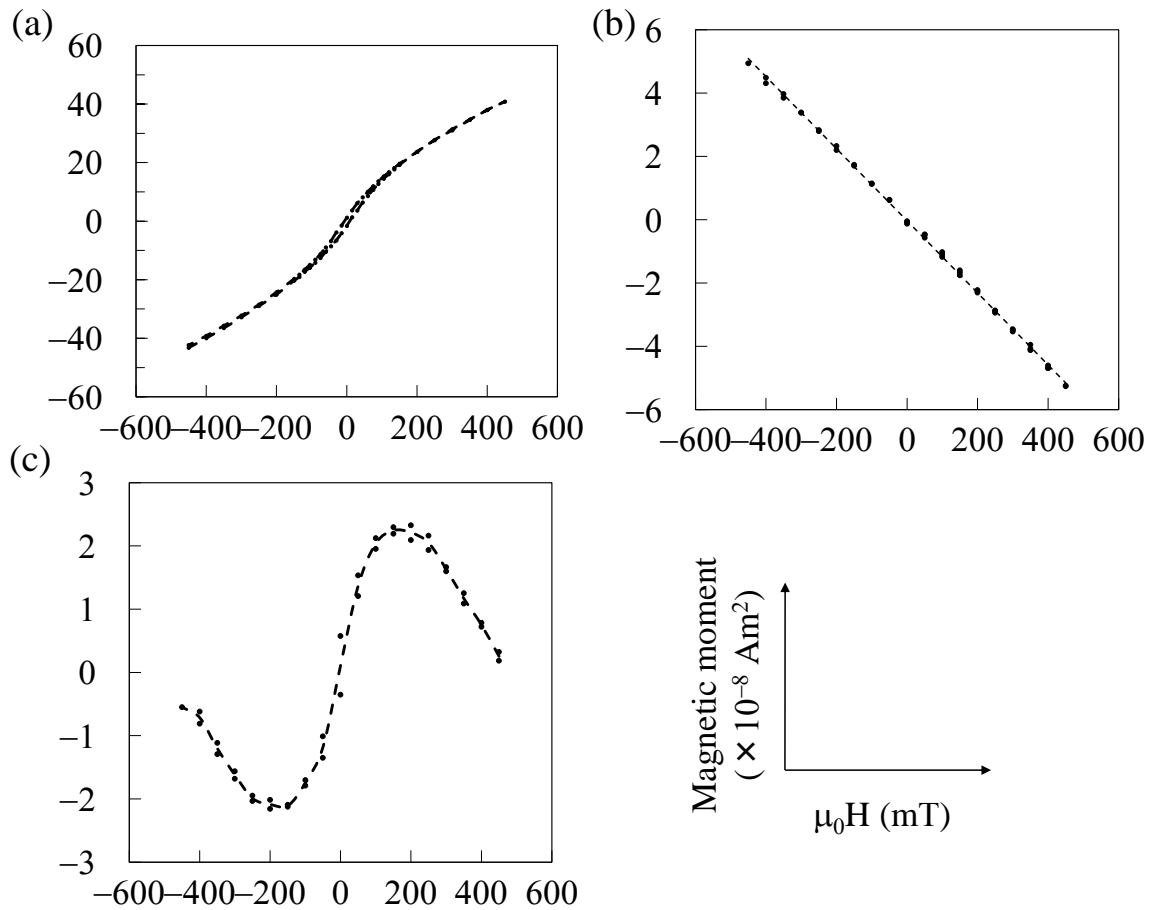
Fig. 6.3.1. Magnetization curves of base materials in mortar; (a) Portland cement, (b) water and (c) standard sand.

measurement was performed at room temperature. The output of the developed measurement system was calibrated with a low-T_c SQUID susceptometer (Quantum Design, MPMS) by measuring the magnetization curve of the same MnF_2 sample. The magnetization curves of each sample were obtained by performing a complete loop of magnetization starting from virgin state.

The magnetization curves of each base material in mortar are shown in Fig. 6.3.1. Portland cement showed a ferromagnetic characteristic; its magnetization rapidly increased and saturated with increasing of magnetic field. The magnetization of water increased linearly with magnetic field, which is a typical characteristic of diamagnetism. In the case of standard sand, its magnetization curve showed a complex characteristic. In a low magnetic field region,

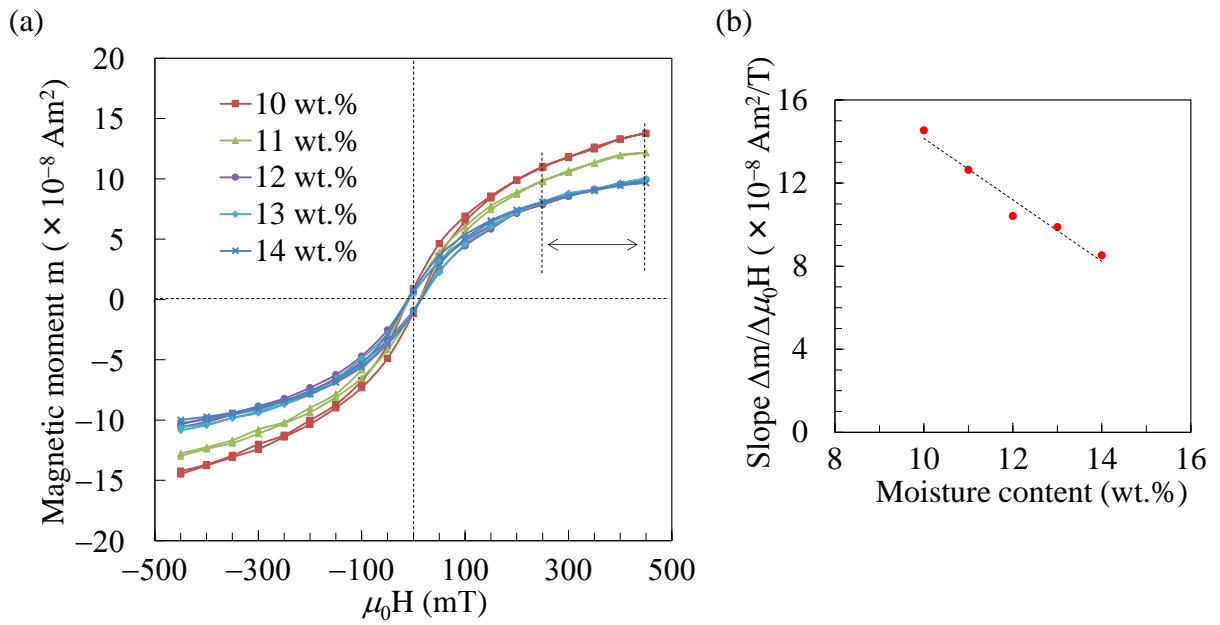**Fig. 6.3.2.** (a) Magnetization curves of mortar samples with different moisture contents. (b) Calculated slope in the region from 250 mT to 450 mT with respect to moisture content.

paramagnetism or ferromagnetism was observed and this positive susceptibility turned to negative susceptibility (diamagnetism) in the regions higher than 200 mT. This was due to standard sand consists of mainly natural silica (over 99%) and impurities [48]. Impurities which contained paramagnetic and ferromagnetic materials had resulted in a rapid increase and saturation of magnetization in the region below 200 mT. Then, the diamagnetic effect from natural silica increased and the magnetization curve showed a negative susceptibility in the regions higher than 200 mT. However, the magnetization of natural sand was weak compared to water and Portland cement, therefore, the magnetization of mortar could be thought to be mainly affected by the amount of water and Portland cement.

The magnetization curves of fresh mortar samples with different moisture contents ranged from 10 wt.% to 14 wt.% are shown in Fig. 6.3.2 (a). The magnetization curves of mortar samples showed a hysteresis characteristic which was similar to the base material of Portland cement. Although diamagnetism of water is small in a low magnetic field, the
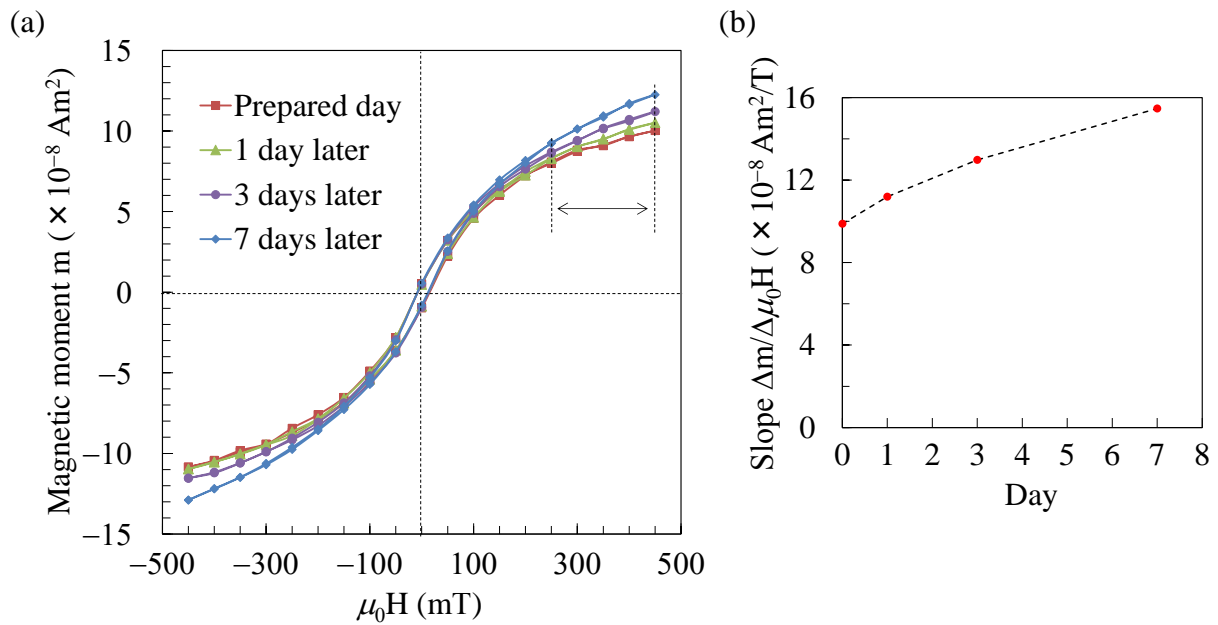
Fig. 6.3.3. (a) Magnetization curves of 13 wt.% mortar sample measured on different days. (b) Calculated slope in the region from 250 mT to 450 mT with respect to time.

magnetization of Portland cement saturates and the diamagnetic effect of water in a mixture material can be observed in a high field. Using this characteristic, the slope of magnetization curve in the region from 250 mT to 450 mT was calculated and is shown in Fig. 6.3.2 (b). The positive slope decreased with the increase of moisture content in mortar. Although the weight ratio of Portland cement to standard sand was kept constant, the increase of weight ratio of water to total mixture material would reduce the amount of Portland cement and natural sand. Therefore, the decrease of the slope, i.e., increase of diamagnetic effect, could be thought to be caused by the increase of moisture content in mortar samples.

To investigate the change of magnetization with respect to time, the magnetization curve of the mortar sample with moisture content of 13 wt.% was evaluated. The magnetization curves were measured on the prepared day and after 1, 3 and 7 days. As shown in Fig. 6.3.3 (a), the magnetization curves changed slightly over time. The hysteresis loops were similar around 0 mT indicating that its ferromagnetism was unchanged; however the slop gradually increased

over time in a higher magnetic field region. The slope derived in the region from 250 mT to 450 mT is shown in Fig. 6.3.3 (b). The gradual decrease in the diamagnetic effect was thought to be related with the decrease amount of free water in the mortar sample. When the cement and water were mixed, hydration process takes place to reduce the amount of free water and increase the amount of bound water. The hydration process changes the main components of Portland cement $3CaO \cdot SiO_2$, $2 \ CaO \cdot SiO_2$, $3CaO \cdot Al_2O_3$ and $4CaO \cdot Al_2O_3 \cdot Fe_2O_3$ to form $nCaO \cdot SiO_2 \cdot mH_2O$ and $Ca(OH)_2$. Since the amount of bound water increase after hydration process, the decrease in the diamagnetic effect was thought to be resulted from the decrease amount of free water. Further investigation on the moisture content and hydration process in mortar using magnetic resonance imaging (MRI) measurement can be found in reference [47].

As a result, a magnetization curve measurement was applied to determine the moisture content in mortar. The magnetic characteristic of base materials and mixed materials of mortar was clarified by performing magnetization curve measurements. The diamagnetic effect in a high magnetic field region was utilized to evaluate the moisture content in mortar. The change in the magnetic characteristic over time due to hydration process was clarified from the magnetization curve measurement. An easy and fast estimation of moisture content in mortar using the proposed magnetic method can be expected.

CHAPTER 7: CHARACTERIZATION OF MAGNETIC NANOPARTICLES IN LOW-CONCENTRATION SOLUTIONS

7.1 Magnetic Nanoparticles

The inner structure of materials is greatly changed when their scale is reduced. The change in the inner structure contributes to the profound modification of their intrinsic electronic, optical properties and magnetic properties. In the case of magnetic nanoparticles (MNPs), the change of magnetic properties has resulted in different magnetic phenomena compared to the established laws for their bulk materials. This results to advancements of new technologies by utilizing these new phenomena [25]. Until today, MNPs have been extensively studied and applied widely for the bio-medical applications such as imaging contrast [25], [49], magnetic hyperthermia agents [49][50], drug delivery systems [25], [49], magnetic immunoassay [51][1], [17], [18], [52]–[58] and *in vivo* imaging using magnetic particle imaging (MPI) technique [59]–[63].

In a bulk ferromagnetic material such as iron, the internal energy in this material is minimized by the spontaneous split of magnetic domains [64]. These magnetic domains contain magnetic moments that are pointing into a same direction and they are separated from each other by domain walls. The formation of domain walls is likely due to defects present in the material. When the dimensions of the material are reduced greatly, the formation of domains to achieve the energetic stability decreases considerably due to the competition between the dipolar interaction and exchange interaction within the system. In the case where no external magnetic field acting on a given volume of the material, the formation of domains is suppressed and the system spontaneously exists as a single domain configuration. Changes of the magnetic behavior due to this scale reduction and a comparison to the size of
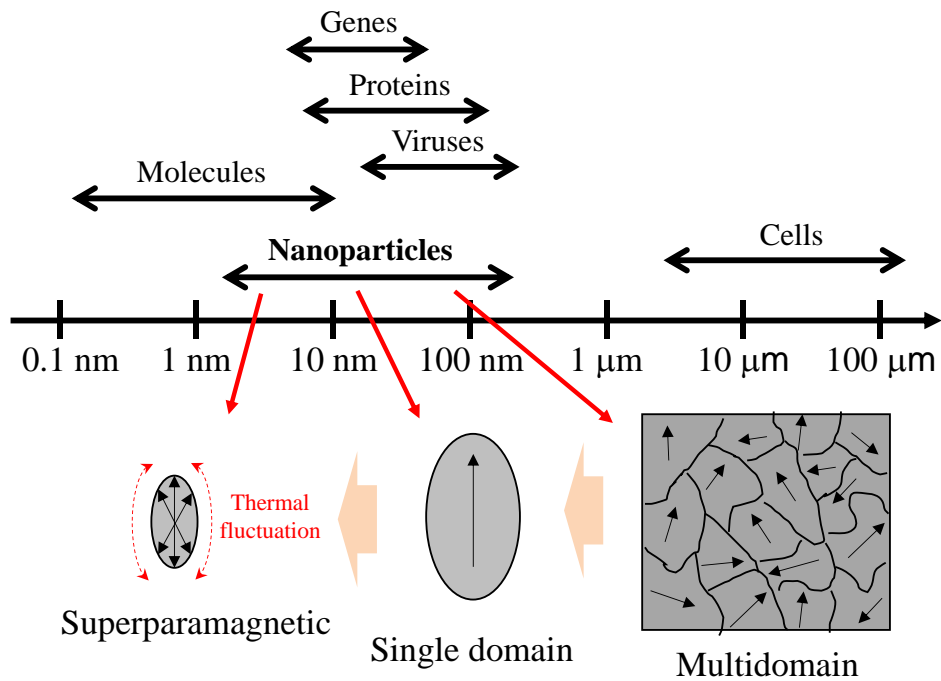
Fig. 7.1.1. Changes of magnetic behavior due to the scale reduction in magnetic materials and a comparison to the dimensions of biological entities.

biological entities are shown in Fig. 7.1.1. The downsized system can be represented as a single superspin where it is uniformly magnetized throughout its volume. The possible orientations of the magnetization in a material are determined by an energy barrier which is the anisotropy energy of the material. The anisotropy energy tends to preserve the magnetization orientation in a particular crystallographic direction (easy axis) where in the absence of an external magnetic field, the magnetization is spontaneously pointed to the easy axis. The easy axis is mainly determined by the anisotropic constant of the material and closely related to the crystal system. When the size of a single domain particle is further reduced in the absence of any external magnetic field, the thermal energy will overcome the energy barrier of the anisotropy energy to rapidly fluctuate the magnetization from one orientation state to other. This process is called as superparamagnetic relaxation where the system has entered into a superparamagnetic regime. The fluctuations of magnetization result in a behavior of a paramagnetic material with a high order magnitude of magnetic moment.

81

This characteristic has opened new applications of MNPs where an improved detection sensitivity can be expected when MNPs are used as a sensing target activated by external magnetic fields. Since their size is comparable to biological entities, promising results can be expected in sensing techniques utilizing MNPs, particularly in bio-medical applications.

The magnetism of MNPs is influenced by several factors such as size distribution of magnetic cores, temperature, morphology (shape anisotropy), intrinsic and extrinsic surface effects, surface spin disorder and magnetic interactions. Assessing the information on these parameters is important in order to optimize MNPs for the target applications where they can be detected through magnetic susceptibility [56], [57], [65]–[68], relaxation [3], [69], [70], and remanence [18], [71], [72] methods. Instrumental techniques such as DC and AC susceptibilities, magnetorelaxometry, Mössbauer spectroscopy, ferromagnetic resonance, neutron diffraction, transmission electron microscopy (TEM), and photon correlation spectroscopy have been used to assess and characterize the magnetic properties of MNPs [25], [73]. As a preliminary study of MNPs, characterization of size distribution is one of the main focus in this research. The magnetic properties of MNPs can be evaluate with a fast an easy way by the measurement of magnetization versus field, i.e., the magnetization of the magnetic nanoparticles as a function of external magnetic field strength. Using the measured magnetization curve, the size distribution of magnetic cores in MNPs can be reconstructed by solving the inverse problem based on assumptions on the model of MNPs. However, the reconstruction quality of the size distribution is influenced by the assumed model and the noise presents in the measured data. In the latter factor, the reconstructed quality may be further reduced in the case of measurement of a small quantity of MNPs suspended in a liquid, which is commonly used in bio-medical applications. Therefore, the analysis of the magnetic properties may require highly sensitive magnetometers to improve the reconstruction quality. Based on this, the sensitivity of the developed magnetometer system was demonstrated by
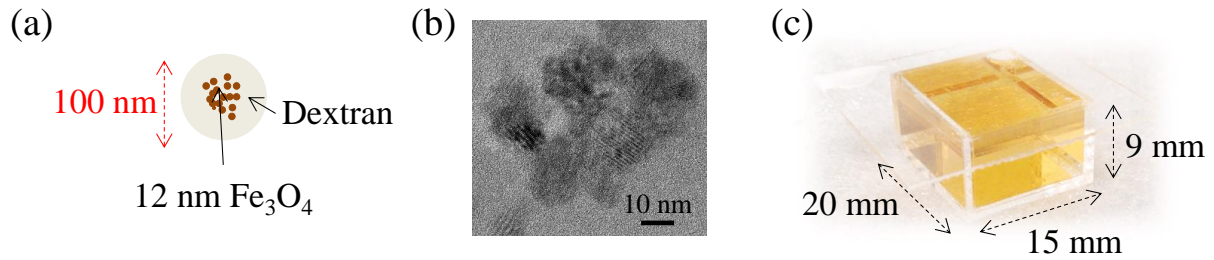
Fig. 7.2.1. (a) Iron oxide multi-core particles coated in dextran with a typical diameter of 100 nm. (b) TEM image of the iron oxide cores. (c) Diluted solution in acrylic measurement case.

investigating the size distribution in highly diluted solution of iron oxide multi-core particles. Measurements of AC and DC magnetizations was performed on the iron-oxide particles solutions. In the AC measurement, harmonics distribution was used as an approach to validate the constructed magnetization curves [74]. In order to achieve a non-biased construction of the distribution and a better fit of the magnetization curves, two construction methods without a prior assumption on the distribution form were applied, i.e., singular value decomposition (SVD) [75] and non-negative non-regularized inversion methods [76]. A comparison on the magnetic property of particles having different typical diameters was also performed to investigate the effect of the aggregated cores in particles.

7.2 Measurement of Magnetization Curves

The magnetic nanoparticles used for characterization of magnetic moment distribution were nanomag®-D-spio (Micromod Partikeltechnologie GmbH). These particles are composed of clusters of single-domain iron oxide nanoparticles and dextran, where dextran is used as coating. The typical diameters of these multi-core particles are 100 nm with the mean size of the elementary particles (iron oxide nanoparticles) is 12 nm as shown in Fig. 7.2.1 (a) and (b). The image of the elementary particles was measured at 200 keV using a transmission electron microscope (JEM-2100F, JEOL Ltd.). As shown in Fig. 7.2.1 (b), these elementary particles

formed particle aggregations in the magnetic nanoparticles with the iron oxide composition of 35 wt%. These multi-core particles are suspended in water with a particle concentration of 7.5×10^{12} particles per ml.

Four sets of low-concentration solutions of the iron oxide multi-core particles were prepared by diluting the stock solution in purified water. The dilution factors of the prepared solutions were 25, 33, 75 and 100, resulting in the iron concentrations of 24 µg/ml, 48 µg/ml, 72 µg/ml, and 96 µg/ml. The prepared solutions were encased in acrylic cases with dimensions of 20 mm $\times$ 15 mm $\times$ 9 mm, constructed from 1 mm acrylic plates. To subtract the background diamagnetic magnetization from water and sample case, magnetization curves of three different empty cases and a water sample were measured. The magnetizations of the 3 acrylic cases were averaged and then fitted using a linear equation. The fitted magnetization curves of the acrylic cases and water were used to subtract the background diamagnetic magnetization in the diluted solutions.

The measured magnetization curves of water and diluted solutions of 100 nm particles at room temperature are shown in Fig. 7.2.2. The magnetization curves were obtained after subtracting the averaged magnetic contribution of the 3 empty cases. The discrete magnetization curves were measured between −240 mT and 240 mT with the smallest intervals of 0.1 mT. As shown in Fig. 7.2.2, the DC susceptibility of the solutions gradually transformed from a positive value to a negative value as the increment of the applied DC magnetic field. The rapid saturation of the iron oxide nanoparticles had resulted in a superparamagnetic characteristic in a low DC magnetic field region. As the magnetization of the iron oxide multi-core particles saturated, the diamagnetic response from the water increased with increasing of the magnetic field. The magnetic saturation of the iron oxide multi-core particles was gradually cancelled by the diamagnetism of water, resulting in a decrease in the observed magnetization. From the measured magnetization curves of highly
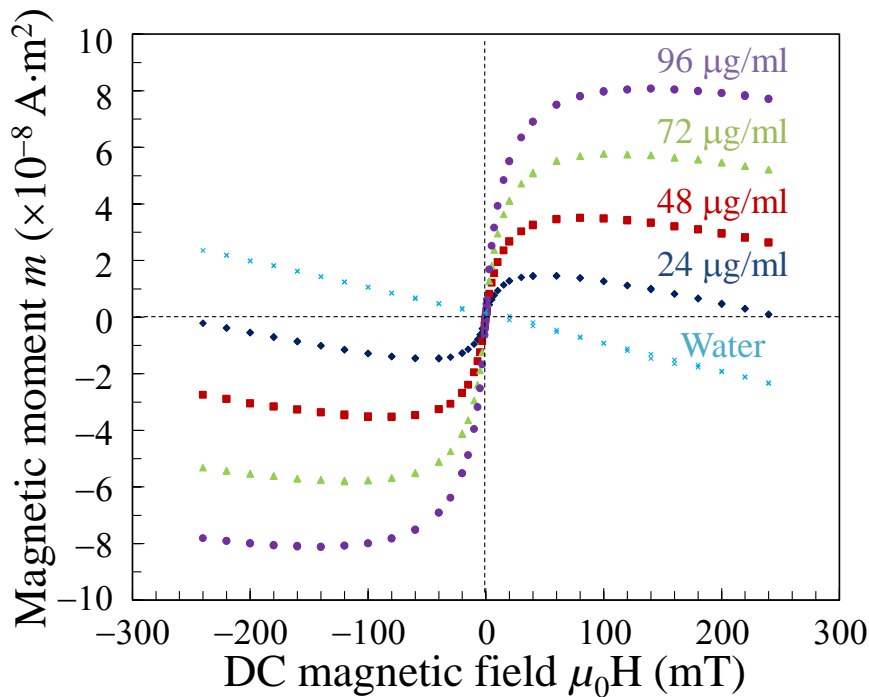
Fig. 7.2.2. Magnetization curves of water and low-concentration solutions of 100 nm iron oxide multi-core particles at room temperature.

diluted solutions, it was clear that the diamagnetic effect of water used as the liquid carrier reduced the observed magnetization and deformed the magnetization curves. Although this diamagnetic effect was comparatively small in the low region of the DC magnetic field, the diamagnetic correction must be performed in the analysis of the magnetic moment distribution.

7.3 Reconstruction Methods of Distribution of Magnetic Moments

The distribution reconstruction of magnetic moments $m = M_s V$ in particles can be achieved by analyzing the discrete magnetization curves. Here, M_s is the intrinsic saturation magnetization and V is the core volume of the magnetic particles. For a monodisperse sample having a single particle magnetic moment $m = M_s V$, the average magnetization M during the

application of an external magnetic field H can be expressed by the so-called Langevin function:

$$M(\mu_0 H) = M_0 L(m\mu_0 H / k_b T),\qquad(7.3.1)$$

where k_B is the Boltzmann constant, T is the absolute temperature, μ_0 is the vacuum permeability, and $L(x) = coth(x) - 1/x$ is the Langevin function. The spontaneous magnetization M_0 is given by $M_0 = c\,m$, where c is the particle concentration. However, in a physical sample, the magnetic moment m is distributed to some extents and is not sufficient to be represented by a single value. Therefore, for a system where particles are not effected by interparticle interactions and having isotropic spin governed by thermal fluctuations and the magnetization field, the average magnetization of magnetic moments with a distribution of $\rho(m)$ is given

$$M(\mu_0 H) = \int m\rho(m)L(m\mu_0 H / k_b T)dm\,.\qquad(7.3.2)$$

To obtain a numerical solution for a measured ferrofluid magnetization M with N points of the applied magnetic field H, equation (7.3.2) can be discretized in N linear equations of

$$M(\mu_0 H_i) = \sum_{j=1}^{J} \Delta m\, m_j\, \rho_j(m) L(m_j \mu_0 H_i / k_b T),\qquad(7.3.3)$$

where $i = 1,\ldots,N$ is the number of magnetic field H_i. Here, J denotes the number of discretization intervals of the distribution $\rho(m)$ and $\rho_j(m)\Delta m_j = n_j$ represents the number of particles with a magnetic moment between m_j and $m_j + \Delta m$. Equation (7.3.3) can be further simplified as

$$M(\mu_0 H_i) = \sum_{j=1}^{J} w_j\, L(m_j \mu_0 H_i / k_b T),\qquad(7.3.4)$$

where $w_j(nm^2)=\Delta m \; m_j \; \rho_j(m)$ is the magnetic moment-weighted distribution. Instead of equation (7.3.3), equation (7.3.4) is easy to apply since $w_j(nm^2)$ represents as a constant to the sum of the Langevin functions of magnetic moment m_j. Furthermore, $w_j(nm^2)$ expresses the magnetic contribution of a magnetic moment m to the resulted distribution in a measured magnetization curve. As the measured magnetization at different points can be represented by vector m with the components $m_i=M(\mu_0 H_i)$, the magnetic weighted contribution by vector w and the Langevin function $L(m_j\mu_0 H_i/k_b T)$ by the $N \times J$ matrix $\mathbf{A}$, equation (7.3.4) can be rewritten as

$$m_i = \sum_{j=1}^{J} A_{ij} w_j \qquad (i = 1,....,N).$$

(7.3.5)

Solving the magnetic weighted distribution w_j for measured magnetization values can be achieved by minimizing the deviation χ^2 between the measured and calculated magnetization values. Moreover, the solution for equation (7.3.5) is the distribution of some physical quantity where it should be non-negative: $w_j \geq 0$. Therefore, the magnetic moment weighted distribution w_j is the solution for the non-negative least-squares problem in which the deviation

$$\chi^2 = \left\| \mathbf{m} - \mathbf{A}\mathbf{w} \right\|^2 = \sum_{i=1}^{N} \left(m_i - \sum_{j=1}^{J} A_{ij} w_j \right)^2$$

(7.3.6)

is minimize with vector $\mathbf{w}$ satisfying the condition $w_j \geq 0$ $(j = 1,…,J)$.

To obtain the required distribution of the magnetic moments $\rho(m)$ for a ferrofluid sample, its measured magnetization curve $M(H)$ can be fitted using equation (7.3.2). In the most simplified approaches used to determine the distribution of the magnetic moments $\rho(m)$, the distribution is assumed to be some analytical forms such as log-normal function. However, this approach is not satisfactory due to the need of such priori information of the distribution

and not sufficient for complicate cases of distribution. Generally, an analysis techniques that requires no assumption on the distribution results a better fit of the measured magnetization curve. The direct approach for a non-biased reconstruction of $\rho(m)$ is to solve the integral equation in equation (7.3.2) [75]. However, this approach will result to the ill-conditioned solution due to unavoidable experimental errors during measurements of $M(H)$, resulting a large non-physical oscillation of the solution $\rho(m)$. Therefore, a specific regulation technique for the ill-conditioned solution is required in order to suppress this oscillation. This inversion problem can be solved by many inversion methods such as generic algorithms [77], singular value decomposition (SVD) [75], [78], moment expansion [79], and non-negative least squares methods [76]. In this study, the minimization problem of equation (7.3.6) was carried out by using the singular value decomposition (SVD) [55], [75] and non-negative non-regularized least squares methods [76], [80], which were implemented in Mathematica (Wolfram Research, USA).

7.3.1 Singular Value Decomposition Method

The SVD is performed by decomposing the system matrix to $\mathbf{A} = \mathbf{USV}^{\mathrm{T}}$, where $\mathbf{U}$ and $\mathbf{V}$ is the $N \times N$ and $J \times J$ orthogonal matrices and $\mathbf{S}$ is the $N \times J$ diagonal matrix with elements s_i ($= s_{ii}$, $i = 1,\ldots$, min (N, J) of singular values of $\mathbf{A}$. Therefore, equation (7.3.5) can be represented as

$$
\begin{bmatrix} m_1 \\ \vdots \\ m_i \\ \vdots \\ m_N \end{bmatrix} = \begin{bmatrix} u_{11} & \cdots & u_{1N} \\ \vdots & \ddots & \vdots \\ u_{N1} & \cdots & u_{NN} \end{bmatrix} \begin{bmatrix} s_1 & 0 & 0 & \cdots & 0 & 0 & \cdots & 0 \\ 0 & \ddots & 0 & \cdots & 0 & 0 & \cdots & 0 \\ 0 & 0 & s_{i=j} & \ddots & 0 & 0 & \cdots & 0 \\ \vdots & \vdots & \ddots & \ddots & 0 & \vdots & \ddots & \vdots \\ 0 & 0 & \cdots & 0 & s_N & 0 & \cdots & 0 \end{bmatrix} \begin{bmatrix} v_{11} & \cdots & v_{1J} \\ \vdots & \ddots & \vdots \\ v_{J1} & \cdots & v_{JJ} \end{bmatrix}^T \begin{bmatrix} w_1 \\ \vdots \\ w_j \\ \vdots \\ w_J \end{bmatrix}, \quad (7.3.7)
$$

$$
\mathbf{m} = \mathbf{USV}^T \mathbf{w} .
$$

Equation (7.3.7) can be rearranged as

$$\mathbf{U}^T\mathbf{m} = \mathbf{U}^T\mathbf{U}\mathbf{S}\mathbf{V}^T\mathbf{w} = \mathbf{S}\mathbf{V}^T\mathbf{w}. \tag{7.3.8}$$

Since the $\mathbf{m}$, $\mathbf{U}$, $\mathbf{S}$, and $\mathbf{V}$ matrices are known-value matrices, the $\mathbf{V}^T\mathbf{w}$ matrix can be determined from the calculated $\mathbf{U}^T\mathbf{m} = \mathbf{b}$ matrix and the diagonal elements of $\mathbf{S}$.

$$\mathbf{U}^T\mathbf{m} = \mathbf{b} = \begin{bmatrix} b_1 \\ \vdots \\ b_i \\ \vdots \\ b_N \end{bmatrix} = \begin{bmatrix} s_1 & 0 & 0 & \cdots & 0 & 0 & \cdots & 0 \\ 0 & \ddots & 0 & \cdots & 0 & 0 & \cdots & 0 \\ 0 & 0 & s_{i=j} & \ddots & 0 & 0 & \cdots & 0 \\ \vdots & \vdots & \ddots & \ddots & 0 & \vdots & \ddots & \vdots \\ 0 & 0 & \cdots & 0 & s_N & 0 & \cdots & 0 \end{bmatrix} \begin{bmatrix} v_{11} & \cdots & v_{1J} \\ \vdots & \ddots & \vdots \\ v_{J1} & \cdots & v_{JJ} \end{bmatrix}^T \begin{bmatrix} w_1 \\ \vdots \\ w_j \\ \vdots \\ w_J \end{bmatrix}$$

$$= \begin{bmatrix} s_1 & 0 & 0 & \cdots & 0 & 0 & \cdots & 0 \\ 0 & \ddots & 0 & \cdots & 0 & 0 & \cdots & 0 \\ 0 & 0 & s_{i=j} & \ddots & 0 & 0 & \cdots & 0 \\ \vdots & \vdots & \ddots & \ddots & 0 & \vdots & \ddots & \vdots \\ 0 & 0 & \cdots & 0 & s_N & 0 & \cdots & 0 \end{bmatrix} \begin{bmatrix} g_1 \\ \vdots \\ g_j \\ \vdots \\ g_J \end{bmatrix} = \mathbf{S}\mathbf{g}. \tag{7.3.9}$$

This can be further simplified to

$$\begin{bmatrix} b_1 \\ \vdots \\ b_i \\ \vdots \\ b_N \end{bmatrix} = \begin{bmatrix} s_{11}g_1 \\ \vdots \\ s_{ij}g_j \\ \vdots \\ s_N g_{j=N} \end{bmatrix}, \tag{7.3.10}$$

$$\therefore \sum_{j=1}^{J} g_j = \begin{cases} \sum_{i=j=1}^{N} b_i / s_{ij} & \text{for } j = i \le N \\ 0 & \text{for } N < j \le J \end{cases}.$$

Therefore, the magnetic moment weighted distribution can be calculated by

$$\mathbf{V}^T\mathbf{w} = \mathbf{g}, \\ \mathbf{w} = \mathbf{V}\mathbf{g}. \tag{7.3.11}$$

However, some singular values of the system matrix $\mathbf{A}$ are very small for the ill-conditioned problem, and this will greatly amplify the errors present in the matrix $\mathbf{b} = \mathbf{U}^T\mathbf{m}$ when the b_i components are divided with these relatively small s_i. The errors in the matrix $\mathbf{g}$ and in the magnetic moment weighted distribution $\mathbf{w}$ can be arbitrary large. The

conventional method to suppress this numerical instability in SVD is to introduce a threshold value $s_{\min}$ for the singular values of S. The component $g_i = b_i/s_i$ is calculated for $s_i > s_{\min}$ and $g_i = 0$ for $s_i < s_{\min}$. The choice of the threshold value $s_{\min}$ can be determined using $s_{\min} = \sigma\, s_{\max}$, where σ and $s_{\max}$ are the average relative experimental error and the maximal singular value of the system matrix $\mathbf{A}$, respectively. Apart from that, it is also must be noted that the final solution of $\mathbf{w}$ by the conventional SVD method will result in the negative values, where the physical quantity of $\mathbf{w}$ should be non-negative: $w_j \geq 0$. The values of the magnetic moment can be set in logarithmic scale to homologize a sample with a wide distribution of magnetic moment; $m_j = m_{\min}(m_{\max}/\, m_{\min})^{(j-1)/(N-1)}$. The expected value of $m_{\min}$ can be determined by $k_b T/\, H_{\max}$ where $H_{\max}$ is the maximum applied magnetic field of the magnetization curve $M(H)$. The corresponding $m_{\max}$ can be expected using the same manner by substituting the minimum applied magnetic field. Insufficient range of the distribution of the magnetic moments m will result in the abrupt cut-off of the reconstructed distribution from zero point of distribution, unlike any normal physical distribution having a closed and finite distribution. Adjusting the range of the distribution after several attempts of reconstructions can avoid this abrupt cut-off. In this study, the range of the magnetic moment for the system matrix $\mathbf{A}$ is adjusted after several reconstructions of the distribution $\mathbf{w}$. Several attempts on the reconstruction will provide an insight on the distribution patterns. These patterns may contain a closed continuous distribution and oscillations with negative values. The closed continuous distribution may reflect the 'true' distribution of the magnetic moment. Using this information, the range of the magnetic moment, which is to be calculated in the system matrix $\mathbf{A}$ prior to the decomposition, can be adjusted to obtain only positive values of distribution. Detail explanations on the analysis of magnetic moment distribution using SVD can be found in references [55], [75].

7.3.2 Non-Negative Non-Regularized Inversion Method

In order to obtain a physical meaning of the solution of the inversion problem, the solution must be constrained to be positive; $w_j \geq 0$ ($j = 1,\ldots,J$). In this method, this non-negative least squares problem is solved by minimizing the mean squared deviation of equation (7.3.6) using a non-negative least mean squares method, developed by Lawson and Hanson [81]. Moreover, the advantage of this method is that the non-negative constraint w_j results in equation (7.3.5) becomes less ill-conditioned, i.e., a more physically stable solution. The algorithm developed by Lawson and Hanson starts with a set of possible basis solutions and improves its candidate solution by taking a finite number of steps. The algorithm is shown as follows.

Input: $\mathbf{A} \in \mathbf{R}^{m \times n}$, $\mathbf{b} \in \mathbf{R}^m$

Output: $x^* \geq 0$ such that $x^* = \arg \min \| \mathbf{Ax} - \mathbf{b} \|^2$.

Initialization: $P = \emptyset$, $R = \{1, 2, \cdots, n\}$, $\mathbf{x} = \mathbf{0}$, $\mathbf{w} = \mathbf{A}^T (\mathbf{b} - \mathbf{Ax})$

Repeat

1. Proceed if $R \neq \emptyset \wedge [\max_{i \in R}(w_i) > \text{tolerance}]$

2. $j = \arg \max_{i \in R}(w_i)$

3. Include the index j in P and remove it from R

4. $s^P = [(\mathbf{A}^P)^T \mathbf{A}^P]^{-1} (\mathbf{A}^P)^T \mathbf{b}$

    4.1. Proceed if $\min(s^P) \leq 0$

    4.2. $\alpha = -\min_{i \in P} [x_i/(x_i - s_i)]$

    4.3. $\mathbf{x} := \mathbf{x} + \alpha(\mathbf{s} - \mathbf{x})$

    4.4. Update R and P

    4.5. $s^P = [(\mathbf{A}^P)^T \mathbf{A}^P]^{-1} (\mathbf{A}^P)^T \mathbf{b}$

    4.6. $\mathbf{s}^R = 0$

5. $\mathbf{x} = \mathbf{s}$

6. $\mathbf{w} = \mathbf{A}^T (\mathbf{b} - \mathbf{Ax})$

In the SVD method, the threshold singular value $s_{\min}$ acts as a regularizing parameter where a higher threshold value will smoothen the distribution, resulting in peak broadening. On the other hand, if the threshold value is too small, the solution may oscillate with non-negative values. However, in the non-negative least squares method where it enforces positive constraints, the regularization is not applied so that peaks can be distinguished in case of multi-modal distributions. The principal of the non-regularization method is by splitting N intervals of magnetic moments into k domains and these domains are further split into S subdomains. Each subdomains only contain a magnetic moment. For one evaluation, a set of subdomains $\mathbf{n}_s$ composed of one magnetic moment in every domain is evaluated together using the non-negative least mean squares method. By this division, the number of magnetic moments taken into account for the minimization of equation (7.3.6) is reduced, rendering the problem less ill-conditioned so that fast converged solutions can be achieved. A set of subdomains $\mathbf{n}_s$ can be expressed as

$$
\begin{aligned}
\mathbf{n}_s &= \left(m_s, m_{S+s}, m_{2S+s}, \cdots, m_{(k-1)S+s} \right)^T, \\
k &= 1, \cdots, \frac{N}{S}; \quad s = 1, \cdots, S; \quad \frac{N}{S} \in Integer.
\end{aligned}
\tag{7.3.12}
$$

By performing k evaluations on all subdomains, the results of k evaluations can be merged into one total probability distribution of w. The solutions of each evaluations give an equal probability of solution to the problem; thus, small peaks arise within the range of one or a few of magnetic moments can be considered as noise.

A precise reconstruction of magnetization curve with a high resolution of magnetic moments can be obtained by setting a large number N to be taken into account for the minimization; however, this can contribute to noisy peaks in the probability distribution and a long computation time. A large number N can be an optimal choice in the case of a
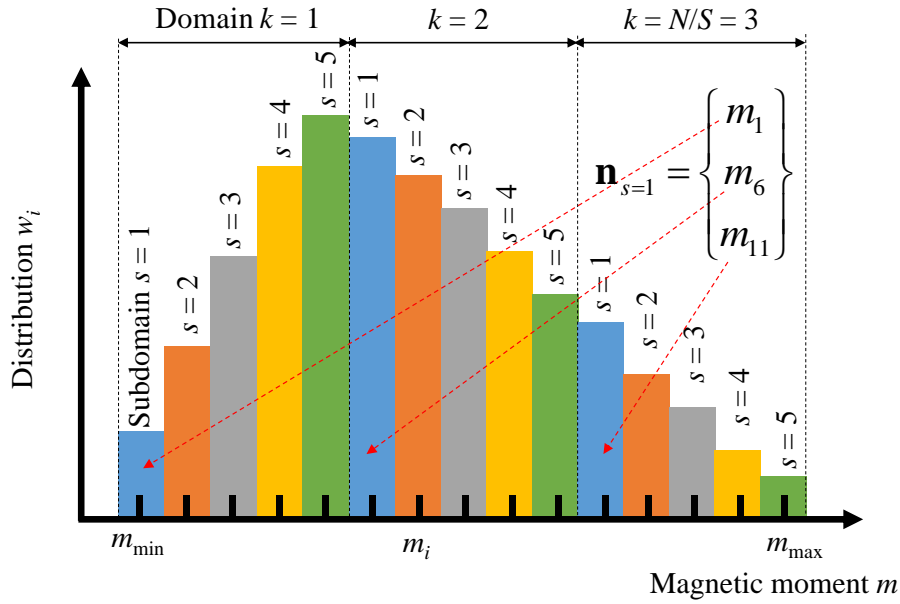
Fig. 7.3.1. Division of magnetic moments into k domains and S subdomains in the non-negative non-regularized inversion method.

monomodal system with low polydispersity. However, in the case of a small number N, the evaluations yield a smooth probability distribution, resulting in peak broadening where peaks of a multimodal system may not be distinguished. This is comparable in the case of a high threshold singular value s_{min} is used in the SVD method. The number of subdomains S has an optimal value with respect to the number of N intervals of magnetic moments. Following the optimized value of S determined in reference [76], a value of 20 magnetic moments per decade in logarithmic scale was used in the analysis.

7.4 Reconstruction of Magnetization Curves

The analyzed distributions of magnetic weight w with respect to m for the SVD and non-negative non-regularized inversion methods are shown in Fig. 7.4.1 (a) and Fig. 7.4.2 (a), respectively. Using the obtained distributions for each concentration in both methods, the magnetization curves were reconstructed and are shown in Fig. 7.4.1 (b) and Fig. 7.4.2 (b),
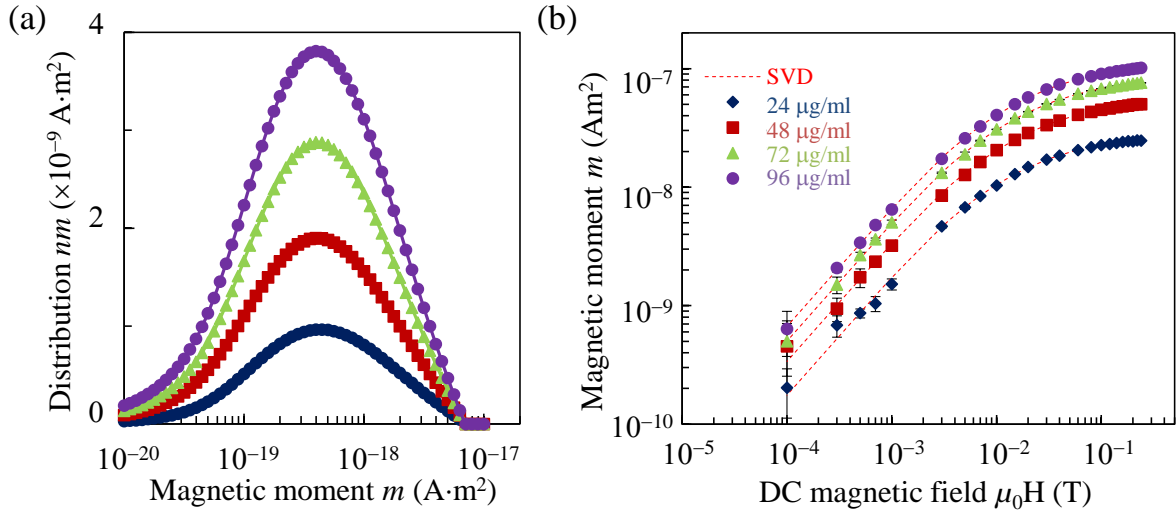
Fig. 7.4.1. (a) Constructed magnetic weight distribution and (b) comparison of measured and reconstructed magnetization curves in the SVD method.
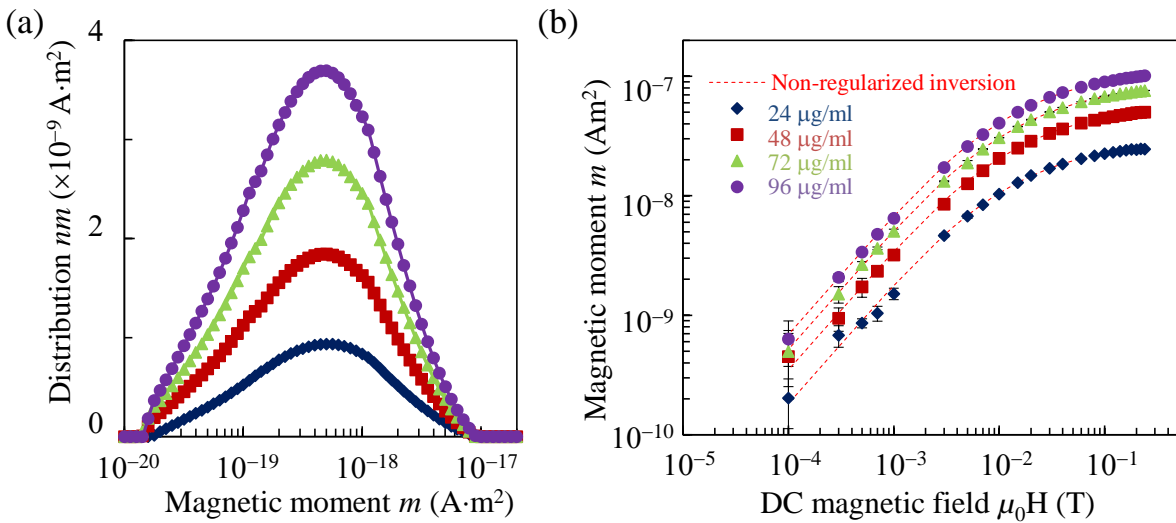

Fig. 7.4.2. (a) Constructed magnetic weight distribution and (b) comparison of measured and reconstructed magnetization curves in the non-negative non-regularized inversion method.

respectively. The obtained distributions in the SVD and non-negative non-regularized methods were similar for all concentrations. The fit quality in both method can be assessed by determining the norm of residual σ between the calculated values of magnetization m^{calc} and the experimental values m^{exp}. The norm of residual σ between the measured and calculated magnetization curves is expressed by

$$\sqrt{\sum_{i=1}^{N}\left(m_i^{\text{exp}} - m_i^{calc}\right)^2} \qquad (7.4.1)$$

and the calculated values of σ in both methods are shown in Fig. 7.4.3 (a). A good quality of fit of the magnetization curves was obtained in both methods since the σ values were fairly low. The peak values in the obtained distributions with respect to the concentration in both methods are shown in Fig. 7.4.3 (b). The peaks of the distributions correlated with the concentration, revealing the change in the number of the most magnetically contributed particles in the solutions. The intrinsic saturation magnetization from the measured magnetization curves was determined to be M_s = 333 kA/m at 240 mT by using the specific density of 5150 kg/m^3 for the magnetic nanoparticles. The values of M_s and the specific density were typical values for iron oxide nanoparticles of magnetite or maghemite at room temperature. By assuming a spherical shape of magnetic cores where $m = (\pi/6)d^3 M_s$, the peaks around $m = 4 \times 10^{-19}$ Am^2 could be determined to correspond to elementary particles with a core size of d = 13.19 nm. This calculated size of elementary particles was approximately the same with the size determined from the TEM image in Fig. 7.2.1 (b).
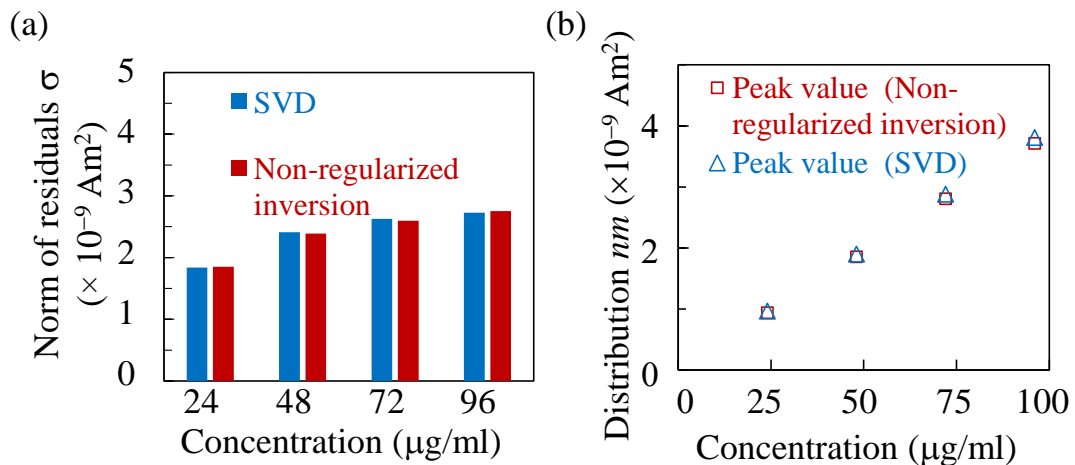

Fig. 7.4.3. (a) Calculated norm of residuals σ. (b) Peak values of the distribution with respect to concentration.

7.5 AC Response of Magnetic Nanoparticles in Solutions

The dynamic magnetization of the 100 nm iron oxide multi-core particles in solutions can be investigated by measuring the harmonics induced upon the excitation of AC and DC magnetic fields. These harmonics can be utilized to validate the measured magnetization curves since they are induced from the non-linear magnetization of MNPs as shown in Fig. 7.5.1. In the case of MNP systems that satisfy equation (7.3.2) and where effects such as Neel and Brownian relaxations can be ignored, the harmonics resulted from the excitation of the AC and DC magnetic fields can be utilized to estimate the shape of the magnetization curve. Since the generated harmonics reflect the shape of the magnetization curve in the regions covered by the excitation magnetic fields, a fast estimation on the shape of magnetization curve can be expected compared to measurement of magnetization curve. Based on this method, the harmonics of the prepared low-concentration solutions were measured during excitation of the AC and DC magnetic fields. An AC magnetic field of 30 mT$_{pp}$ and 5 Hz was
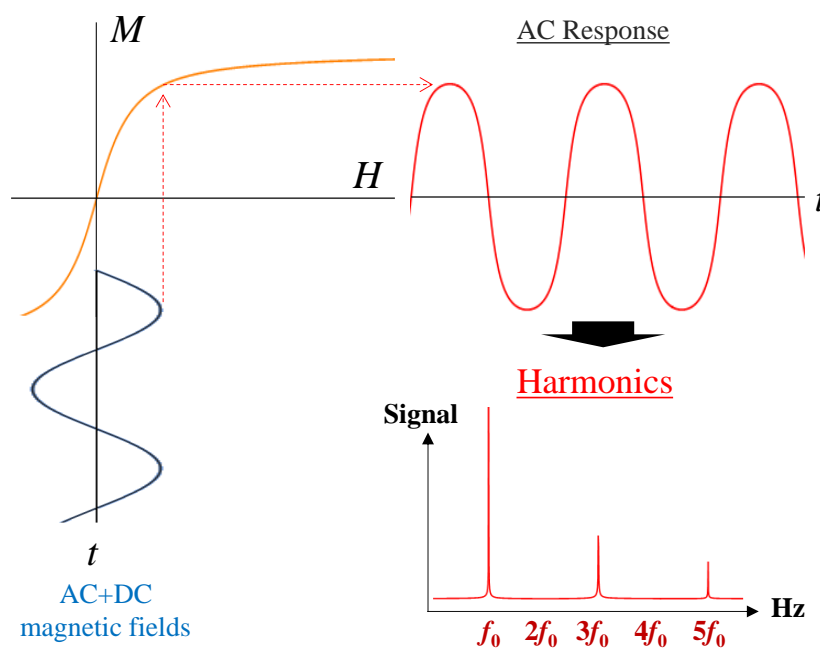

Fig. 7.5.1. Harmonics induced due to non-linear magnetization of magnetic nanoparticles upon application of AC and DC magnetic fields.
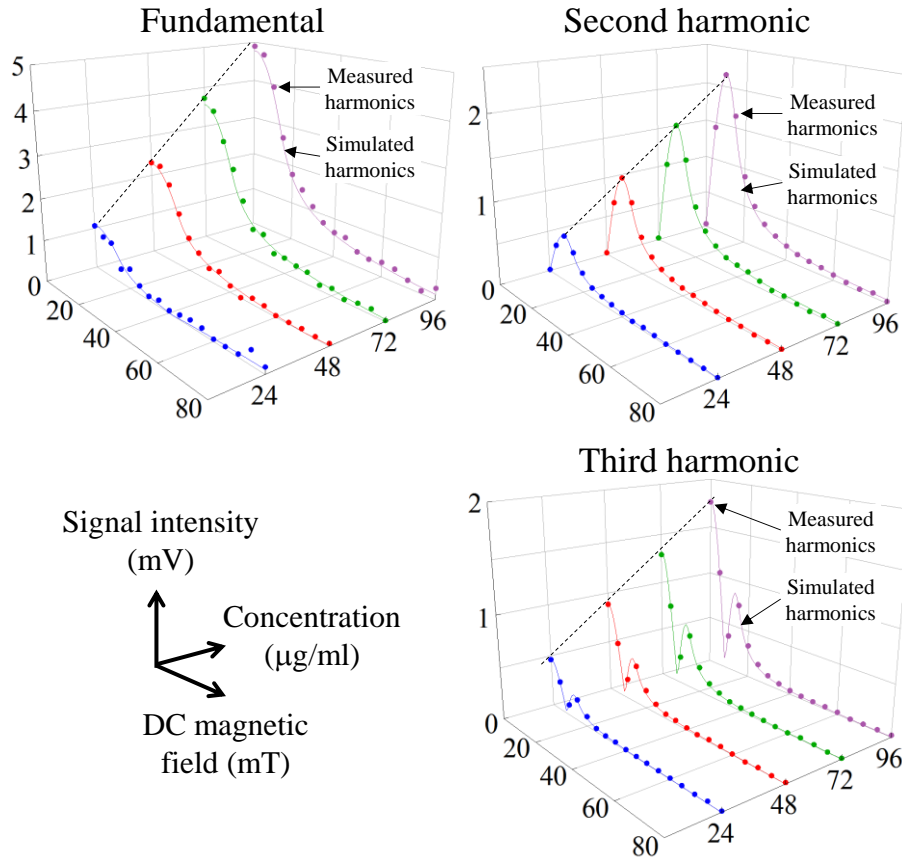
Fig. 7.5.2. Comparison of measured and calculated harmonics of the 100 nm iron oxide multi-core particles in low-concentration solutions.

applied with different offsets of DC magnetic fields to obtain the harmonics distribution over DC magnetic fields, i.e., the characteristic of the magnetization curve. The measured harmonics of the prepared solutions are shown in Fig.7.5.2. To reveal the relation between the harmonics and magnetization curves, the time waveform of magnetization was simulated upon the excitation of AC and DC magnetic fields. The obtained distribution was substituted into equation (7.3.3) to calculate the time waveform magnetization and Fast Fourier Transform (FFT) analysis was performed to extract the harmonics. Since the induced fundamental component reflects the slope of the deformed magnetization curve, the magnetic contributions from the sample case and water were accounted for in the calculation. The results for the simulated and measured fundamental, second, and third harmonic components are shown in Fig. 7.5.2 by the solid lines. A good agreement between the simulated and
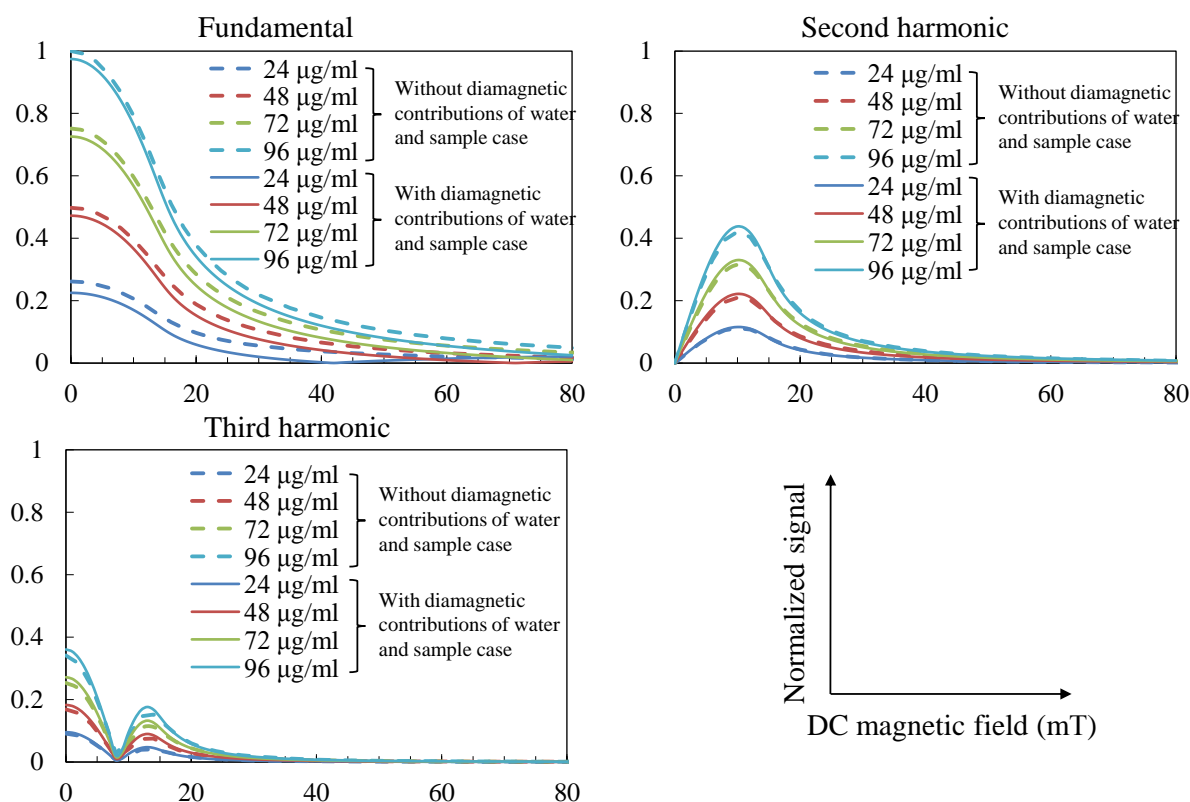
Fig. 7.5.3. Simulated harmonics of the 100 nm iron oxide multi-core particles with and without diamagnetic contributions of water and sample case with respect to DC magnetic field.

measured components indicated that the discrete magnetization curves of the highly diluted 100 nm iron oxide multi-core particles were successfully measured. Furthermore, the peaks of the induced harmonics were also correlated with the concentrations of the iron oxide particles. From this, a fast determination of the concentration of iron oxide multi-core particles could be expected by utilizing the induced harmonics. Furthermore, the detection sensitivity for iron oxide particles, i.e., the slope of dashed lines in Fig. 7.5.2, could be improved by appropriate selection of the bias DC magnetic field. To investigate the effect of the diamagnetic contributions of water and sample case to the harmonics, the induced harmonics of the 100 nm iron oxide multi-core particles with and without the diamagnetic contributions were simulated. The calculated harmonics are shown in Fig. 7.5.3. A non-negligible difference between the fundamental component in the cases of with and

without the diamagnetic contributions could be observed. The diamagnetic contributions deformed the magnetization curves of magnetic nanoparticles in highly diluted solutions and affected the induced fundamental signal. From this, the diamagnetic contributions of the sample case and water should be taken into account when measuring a highly diluted solution of magnetic nanoparticles.

7.6 Comparison of Magnetic Nanoparticles

Factors such as the size of elementary particles and aggregation degree of the elementary particles affect the magnetic properties of the magnetic nanoparticles. To investigate the effect of the aggregation degree of elementary particles to the magnetic property, a magnetization curve of 130 nm iron oxide multi-core particles in solution (nanomag®-D, Micromod Partikeltechnologie GmbH) was measured. This 130 nm particles are composed of clusters of 12 nm-single domain iron oxide core and coated in dextran, which are same with the 100 nm particles. The typical diameters of the particles are 130 nm and these particles are suspended in water with a particle concentration of 7.3×10^{12} particles per ml. Compared to the 100 nm particles, the 130 nm particles contain a higher composition of iron oxide ranging from 60 to 70 wt%. The stock solution of the 130 nm particles was diluted with a dilution factor of 50 during sample preparation for the magnetization curve measurement.

The measured magnetization curve and the constructed distribution of the 130 nm particles in solution are shown in Fig. 7.6.1. A non-negligible hysteresis characteristic was observed in the 130 nm particles in comparison to the 100 nm particles. Since the magnetization curve showed the hysteresis characteristic, the distribution of magnetic moments was reconstructed by using the initial magnetization curve ranged from 0 mT to 240 mT. By using the intrinsic saturation magnetization $M_s = 295$ kA/m which was determined from the magnetization curve, the highest peak around $m = 2.5 \times 10^{-19}$ Am^2 was calculated to
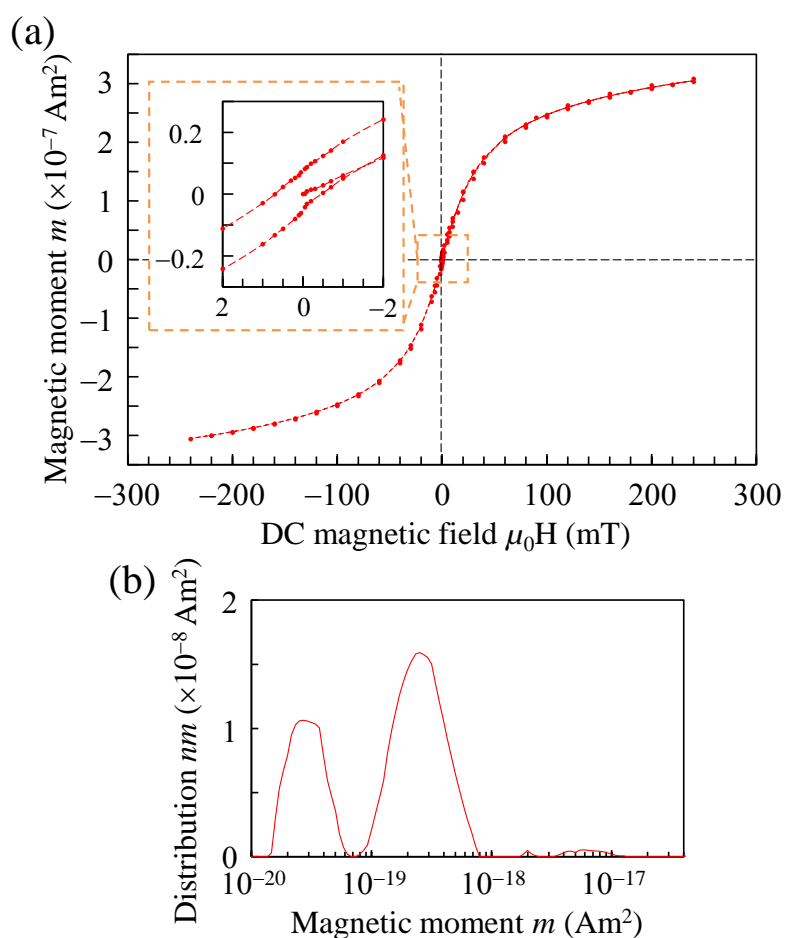
Fig. 7.6.1. (a) Magnetization curve of the 130 nm iron oxide multi-core particles in a low-concentration solution. (b) Constructed distribution of magnetic weight.

correspond to particles with a core size of $d = 11.74$ nm. This calculated core size was approximately same with the known size of the elementary particles. A second peak which corresponded to a core size $d = 5.79$ nm was also observed in the constructed distribution. The origin of this second peak might be due to the model used to extract the distribution parameters was not appropriate since factors such as magnetic interactions between the nanoparticles in the multi-core particles and magnetic anisotropy were not taken into account. Since the high composition of iron oxide in the 130 nm particles, a high degree of aggregation of elementary particles might result in interactions between these elementary particles and affect the magnetic anisotropy of the assembled particles. The comparison of
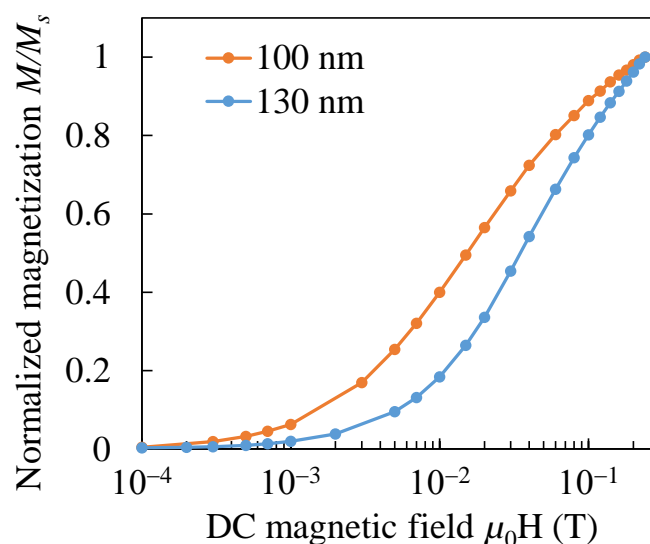
Fig. 7.6.2. Comparison of normalized initial magnetization curves of 100 nm and 130 nm particles.

normalized initial magnetization curves of 100 nm and 130 nm particles is shown in Fig. 7.6.2. The 100 nm particles showed a rapid saturation compared to the 130 nm particles revealing the difference in the magnetic anisotropy between them. From this, a distinct magnetic property between the 100 nm and 130 nm particles was successfully characterized from measurements of magnetization curve.

As a result, the distribution of the magnetic moment was successfully evaluated even in the case of highly diluted solutions by using the developed system. The obtained distributions and the image of the iron oxide nanoparticles revealed that the net magnetic moment originated from multiple iron oxide cores was associated to the size of the magnetic cores and their degree of aggregation in the particles. A highly sensitive exploration on magnetic properties of MNPs can be expected via the developed system.

8. CONCLUSION

A compact AC/DC magnetometer using a high-T_c SQUID with a flux transformer consisted of an induction coil was developed and its characteristics were presented. Increase in sensitivity was attained by improvements performed during this research. The developed system had been implemented in a non-destructive evaluation of moisture content in mortar and characterization of magnetic nanoparticles in solutions for bio-medical applications.

Chapter 1 covered the initial steps in this research where various considerations in the system design were presented. In chapter 2, a comparison of magnetic sensors for application in this research was presented where a configuration consisted of a SQUID with a flux transformer using an induction coil was adopted. The configuration of the high-T_c SQUID employed in this study and its characteristics were presented. The high-T_c SQUID showed a superior sensitivity compared to the conventional ultra-low-noise amplifier.

In chapter 3, the configurations of the developed system were presented in details as well as its basic characteristics for various parts. Improvements in the control and design of the excitation coils in the electromagnet system had resulted in a wide range of excitation magnetic field with a resolution of 40 μT. Synchronization between detection unit and vibrating stage for a precise signal detection were attained. The detected signal intensity could be improved by optimizing the relative position of the first order differential coil and the sample. The investigation of the sample shape dependency using experimental and simulation methods showed that the detected signal was significantly related to the sample surface area compared to the sample height. The developed system showed a high sensitivity as the weak diamagnetism of water was successfully measured.

In chapter 4, investigation and consideration on the harmonic detection technique was performed to improve detection unit sensitivity for the DC susceptibility measurement. Optimizations of the shape of the sample and the first-order differential coil, as well as investigation of harmonic components, were performed using simulation and experimental methods. The induced harmonic components were greatly influenced by the relative position between the first order differential coils and the sample. The detected signal intensity was improved by greater than 3 times in the case of the detection using the elliptical differential coil combined with the harmonic detection technique in comparison to the detection using circular differential coil. By improving the vibration frequency, the effectiveness of the harmonic detection technique can be further amplified.

In chapter 5, the compensation coil method was proposed and investigated to reduce the inference of the excitation magnetic field so that sensitivity could be improved in the AC susceptibility measurement. The compensation coil method showed a superior cancelling characteristic in comparison to the off-axis alignment method. The compensation coil method resulted in a compact detection system with a single detection coil for both AC and DC functions and an improved dynamic range. A cancellation factor of $B_{\text{detected}}/B_{\text{applied}} = 2\times10^{-4}$ was achieved by using the compensation coil method. Furthermore, improvement of the cancellation factor to the order of 10^{-5} can be expected via a finer tuned compensation coil.

In chapter 6, evaluations of moisture content in mortar was performed by measuring the magnetization curve of the mixture materials. The magnetic characteristic of base materials and mixed material of mortar was clarified and the diamagnetic effect in a high magnetic field region was utilized to evaluate the moisture content in mortar. The change in the magnetic characteristic over time due to hydration process could be observed by the developed system.

An easy and fast estimation of moisture content in mortar using the proposed magnetic method can be expected.

In chapter 7, characterization of magnetic moment distribution of the iron oxide multi-core particles of 100 nm and 130 nm in low-concentration solutions were carried out using the developed system. Reconstruction of the magnetic moment distribution using the SVD and non-regularized inversion methods revealed that a similar distribution characteristic was obtained with the peaks correlated with the concentration. The size of iron oxide cores determined from the TEM image, which was approximately 12 nm, agreed with the calculated size in the constructed distributions. A distinctive magnetic property between the 100 nm and 130 nm particles was successfully characterized. Investigation of magnetic properties with high sensitivity using the developed system can be expected in future.

ACKNOWLEDGEMENTS

ACHIEVEMENTS

AWARDS

1. The Best Student Paper-Second Place in Electronics, Applied Superconductivity Conference and IEEE Council of Superconductivity, 2014.8.15.

2. 博士前期課程の研究科長賞, 岡山大学自然科学研究科 電子情報システム工学専攻 電気電子機能開発講座, 2013.3.25.

3. 第 33 回（2012 年秋季）応用物理学会講演奨励賞，「サンプル振動型磁化率計の高感度計測法」第 73 秋季 回応用物理学会学術講演会，愛媛，2012.9.11-14.

REFERED PAPERS

1. **M. M. Saari**, K. Sakai, T. Kiwa, T. Sasayama, T. Yoshida, and K. Tsukada, "Characterization of the magnetic moment distribution in low-concentration solutions of iron oxide nanoparticles by a high-Tc superconducting quantum interference device magnetometer," *J. Appl. Phys.*, vol. 117, no. 17, p. 17B321, May 2015.

2. **M. M. Saari**, Y. Ishihara, Y. Tsukamoto, T. Kusaka, K. Morita, K. Sakai, T. Kiwa, and K. Tsukada, "Optimization of an AC/DC High-Tc SQUID Magnetometer Detection Unit for Evaluation of Magnetic Nanoparticles in Solution," *IEEE Trans. Appl. Supercond.*, vol. 25, no. 3, pp. 1–4, Jun. 2015.

3. **M. M. Saari**, Y. Tsukamoto, T. Kusaka, Y. Ishihara, K. Sakai, T. Kiwa, and K. Tsukada, "Effect of diamagnetic contribution of water on harmonics distribution in a dilute solution of iron oxide nanoparticles measured using high-Tc SQUID magnetometer," *J. Magn. Magn. Mater.*, vol. 394, pp. 260–265, Nov. 2015.

4. **M. M. Saari**, K. Sakai, T. Kiwa, and K. Tsukada, "Optimization of the Detection Technique for a Vibrating-Sample Magnetometer Using High-Tc SQUID," *IEEE Trans. Appl. Supercond.*, vol. 23, no. 3, p. 1600204, Jun. 2013.

5. **M. M. Saari**, K. Sakai, T. Kiwa, A. Tsukamoto, S. Adachi, K. Tanabe, A. Kandori, and K. Tsukada, "Development of a Compact Moving-Sample Magnetometer Using High-Tc Superconducting Quantum Interference Device," *Jpn. J. Appl. Phys.*, vol. 51, p. 046601, Mar. 2012.

6. T. Sasayama, T. Yoshida, **M. M. Saari**, and K. Enpuku, "Comparison of volume distribution of magnetic nanoparticles obtained from M-H curve with a mixture of log-normal distributions," *J. Appl. Phys.*, vol. 117, no. 17, p. 17D155, May 2015.

7. K. Sakai, N. Okamoto, Y. Watanabe, **M. M. Saari**, T. Kiwa, and K. Tsukada, "Moisture Content Evaluation Using Improved High-Tc SQUID-Based Rotating-Sample Magnetometer," *IEEE Trans. Appl. Supercond.*, vol. 25, no. 3, pp. 1–5, Jun. 2015.

8. K. Tsukada, T. Kusaka, **M. M. Saari**, R. Takagi, K. Sakai, T. Kiwa, and Y. Bito, "Magnetic susceptibility and magnetic resonance measurements of the moisture content and hydration condition of a magnetic mixture material," *J. Appl. Phys.*, vol. 115, no. 17, p. 17E301, May 2014.

9. T. Kiwa, S. Miyazaki, **M. M. Saari**, K. Sakai, A. Tsukamoto, S. Adachi, T. Hato, K. Tanabe, and K. Tsukada, "Visualization of ion transportation in an electrolyte using an HTS-SQUID gradiometer," *Phys. C Supercond.*, vol. 504, pp. 84–87, Sep. 2014.

10. T. Kiwa, Y. Fukudome, S. Miyazaki, **M. M. Saari**, K. Sakai, and K. Tsukada, "Magnetic evaluation of a solar panel using HTS-SQUID," *Phys. C Supercond.*, vol. 494, pp. 195–198, Nov. 2013.

11. T. Kiwa, Y. Fukudome, S. Miyazaki, **M. M. Saari**, K. Sakai, A. Tsukamoto, S. Adachi, K. Tanabe, A. Kandori, and K. Tsukada, "Magnetic Detection of Currents in an Electrolytic Cell Using High-Tc SQUID," *IEEE Trans. Appl. Supercond.*, vol. 23, no. 3, p. 1600804, Jun. 2013.

12. K. Sakai, **M. M. Saari**, T. Kiwa, and K. Tsukada, "Compact Rotating-Sample Magnetometer for Relaxation Phenomenon Measurement Using HTS-SQUID," *IEEE Trans. Appl. Supercond.*, vol. 23, no. 3, pp. 1601904–1601904, Jun. 2013.

13. K. Sakai, **M. M. Saari**, T. Kiwa, a Tsukamoto, S. Adachi, K. Tanabe, a Kandori, and K. Tsukada, "Development of a compact DC magnetometer using HTS-SQUID and a rotating sample," *Supercond. Sci. Technol.*, vol. 25, no. 4, p. 045005, Apr. 2012.

OTHER PAPERS

1. **M. M. Saari**, R. Takagi, T. Kusaka, Y. Ishihara, Y. Tsukamoto, K. Sakai, T. Kiwa, and K. Tsukada, "Development of integrated AC-DC magnetometer using high- T c SQUID for magnetic properties evaluation of magnetic nanoparticles in solution," *J. Phys. Conf. Ser.*, vol. 507, no. 4, p. 042035, May 2014.

2. R. Takagi, **M. M. Saari**, K. Sakai, T. Kiwa, and K. Tsukada, "Development of a compact magnetometer with an AC/DC magnetic field using HTS-SQUID," in *Superconductive Electronics Conference (ISEC), 2013 IEEE 14th International*, 2013, pp. 1–3.

ORAL AND POSTER PRESENTATIONS

(INTERNATIONAL CONFERENCES)

1. **Mohd Mawardi Saari**, Kenji Sakai, Toshihiko Kiwa, Teruyoshi Sasayama, Takashi Yoshida and Keiji Tsukada, "*Characterization of magnetic moment distribution in low-concentrated solutions of iron oxide nanoparticles by high-Tc SQUID magnetometer*", 59th Annual Conference on Magnetism and Magnetic Materials (MMM 2014), 3-7 November 2014, Hawai, USA.

2. Toki Kusaka, **Mohd Mawardi Saari**, Yuichi Ishihara, Yuya Tsukamoto, Kenji Sakai, Toshihiko Kiwa, Keiji Tsukada, "*Measurement of moisture content using HTS-SQUID magnetometer*", Progress In Electromagnetics Research Symposium (PIERS 2014), 2014/8/25-28, Guangzhou, China.

3. Shohei Kasuya, Kohei Tanaka, **Mohd Mawardi Saari**, Kenji Sakai, Toshihiko Kiwa, Keiji Tsukada, "*Development of DC Current Distribution Mapping System for Solar Panels Using an HTS-SQUID Gradiometer*", Progress In Electromagnetics Research Symposium (PIERS 2014), 2014/8/25-28, Guangzhou, China.

4. Naohiro Okamoto, Yuta Watanabe, **Mohd Mawardi Saari**, Kenji Sakai, Toshihiko Kiwa, Keiji Tsukada, "*Highly Sensitive Detection Method for Rotating Sample Magnetometer Using HTS-SQUID*", Progress In Electromagnetics Research Symposium (PIERS 2014), 2014/8/25-28, Guangzhou, China.

5. Yuichi Ishihara, **Mohd Mawardi Saari**, Toki Kusaka, Yuya Tsukamoto, Kenji Sakai, Toshihiko Kiwa, Keiji Tsukada, "*Optimization of Pickup Coil in Compact Magnetometer with DC/AC Unit Employing High-Tc SQUID*", Progress In Electromagnetics Research Symposium (PIERS 2014), 2014/8/25-28, Guangzhou, China.

6. **Mohd Mawardi Saari**, Yuya Tsukamoto, Yuichi Ishihara, Toki Kusaka, Koji Morita, Kenji Sakai, Toshihiko Kiwa and Keiji Tsukada, "*Optimization of Detection Unit of AC/DC High-Tc SQUID Magnetometer for Evaluation of Magnetic Nanoparticles in Solution*", Applied Superconductivity Conference 2014 (ASC 2014),10-15 August 2014, Charlotte, NC, USA.

7. Toshihiko Kiwa, Shouhei Kasuya, Shingo Miyazaki, **Mohd Mawardi Saari**, Kenji Sakai, Keiji Tsukada, "*Ion transportation observed by an HTS-SQUID gradiometer*", Applied Superconductivity Conference 2014 (ASC 2014), 10-15 August 2014, Charlotte, NC, USA.

8. Kenji Sakai, Naohiro Okamoto, Toki Kusaka, **Mohd Mawardi Saari**, Toshihiko Kiwa, Keiji Tsukada, "*Moisture Content Evaluation Using Improved High-Tc SQUID Based Rotating-Sample Magnetometer*", Applied Superconductivity Conference 2014 (ASC 2014), 10-15 August 2014, Charlotte, NC, USA.

9. Toshihiko Kiwa, Shinogo Miyazakia, **Mohd M. Saari**, Kenji Sakaia, Akira Tsukamoto, Seiji Adachi, Tsunehiro Hato, Keiichi Tanabe, Keiji Tsukada, "*Time-Domain Measurements of the Ion Transportation in the Electrolyte using HTS-SQUID's Gradiometer*", 26rd International Symposium on Superconductivity (ISS 2013), 18-20, Nov. 2013, Tokyo, Japan.

10. **Mohd Mawardi Saari**, Ryuki Takagi, Toki Kusaka, Yuichi Ishihara, Yuya Tsukamoto, Kenji Sakai, Toshihiko Kiwa and Keiji Tsukada, "*Highly Sensitive Vibrating-Sample Magnetometer Using High-Tc SQUID*", The 7th East Asia Symposium on Superconductive Electronics (EASSE 2013), 23-26 Oct. 2013, Taipei, Taiwan.

11. Keiji Tsukada, **Mohd Mawardi Saari**, Kenji Sakai, and Toshihiko Kiwa, "High performance magnetometers using HTS-SQUIDs and their applications", The 7th East Asia Symposium on Superconductive Electronics (EASSE 2013), 23-26 Oct. 2013, Taipei, Taiwan.

12. Kenji Sakai, Naohiro Okamoto, Daichi Hamasaki, **Mohd Mawardi Saari**, Toshihiko Kiwa and Keiji Tsukada, "*Compact Rotating-Sample Magnetometer Using HTS-SQUID for Magnetic Susceptibility and Magnetic Relaxation Measurement*", The 7th East Asia Symposium on Superconductive Electronics (EASSE 2013), 23-26 Oct. 2013, Taipei, Taiwan.

13. **Mohd Mawardi Saari** , Ryuki Takagi, Toki Kusaka, Yuichi Ishihara, Yuya Tsukamoto, Kenji Sakai, Toshihiko Kiwa and Keiji Tsukada, "*Development of integrated AC-DC magnetometer using high-Tc SQUID for magnetic properties evaluation of magnetic nanoparticles in solution*", 11th European Conference on Applied Superconductivity (EUCAS 2013), 15-19 Sep. 2013, Genoa, Italy.

14. Miyazaki S., Kasuya S., **Saari M.M.**, Sakai K., Kiwa T., Tsukamoto A., Adachi S., Tanabe K., Tsukada K., "*DC current distribution mapping system of solar panels*

using a HTS-SQUID", 11th European Conference on Applied Superconductivity (EUCAS 2013), 15-19 Sep. 2013, Genoa, Italy.

15. Daichi Hamasaki, Naohiro Okamoto, **Mohd Mawardi Saari**, Kenji Sakai, Toshihiko Kiwa, Keiji Tsukada, *"Improvement of sensitivity for a compact magnetometer using HTS-SQUID with rotating sample"*, 14th International Superconductive Electronics Conference (ISEC2013), 7-11 Jul. 2013, Cambridge, MA, USA.

16. Toshihiko Kiwa, Shingo Miyazaki, **Mohd M. Saari**, Kenji Sakai, Akira Tsukamoto, Seiji Adachi, Tsunehiro Hato, Keiichi Tanabe, Keiji Tsukada, *"Current Imaging of Voltaic Systems using High-Tc SQUID"*, 14th International Superconductive Electronics Conference (ISEC2013), 7-11 Jul. 2013, Cambridge, MA, USA.

17. Kenji Sakai, Daichi Hamasaki, **Mohd M. Saari**, Toshihiko Kiwa, Keiji Tsukada, *"Improved rotating-sample magnetometer for magnetic relaxation measurement using HTS-SQUID"*, 14th International Superconductive Electronics Conference (ISEC2013), 7-11 Jul. 2013, Cambridge, MA, USA.

18. Ryuki Takagi, **Mohd Mawardi Saari**, Kenji Sakai, Toshihiko Kiwa and Keiji Tsukada, *"Development of a Compact Magnetometer with an AC/DC Magnetic Field Using HTS-SQUID"*, 14th International Superconductive Electronics Conference (ISEC2013), 7-11 Jul. 2013, Cambridge, MA, USA.

19. **M. M. Saari**, R. Takagi, K. Sakai, T.Kiwa, K. Tsukada, "*Optimization of the detection Technique for a Vibrating-Sample Magnetometer Using High-Tc SQUID*", Applied Superconductivity Conference 2012, Portland, Oregon, USA, 7-12 October 2012.

20. **M. Mawardi Saari**, Ryuki Takagi, K. Sakai, T.Kiwa, A. Tsukamoto, S. Adachi, K. Tanabe, A. Kandori, K. Tsukada, "*Compact Vibrating-Sample Magnetometer using High-Tc SQUID and Shape Dependency of Sample*", 11th International Symposium on High Temperature Superconductors in High Frequency Fields (HTSHFF 2012), Miyagi, Japan, 29 May-1 June 2012.

21. **M. Mawardi**, K. Sakai, T.Kiwa, A. Tsukamoto, S. Adachi, K. Tanabe, A. Kandori, K. Tsukada, "*Development of A Compact Moving-Sample Magnetometer employing HTS-SQUID*", 24rd International Symposium on Superconductivity (ISS 2011), Tokyo, Japan, 24-26, Oct., 2011.

22. K. Sakai, **M. M. Saari**, D. Hamasaki, T.Kiwa, K. Tsukada, "Moisture Content Evaluation Measured by A Compact Rotating-Sample Magnetometer Using High-Tc SQUID", 25rd International Symposium on Superconductivity (ISS 2012), Tokyo, Japan, 3-5 December 2012.

23. K. Sakai, **M. Mawardi Saari**, T.Kiwa, K. Tsukada, "*Compact Rotating-Sample Magnetometer for Relaxation Phenomenon Measurement using HTS-SQUID*", Applied Superconductivity Conference 2012, Portland, Oregon, USA, 7-12 October 2012.

24. T. Kiwa, Y. Fukudome, S. Miyazaki, **M.M. Saari**, K. Sakai, A. Tsukamoto, S. Adachi, K. Tanabe, A. Kandori, K. Tsukada, "*Magnetic Detection of Currents in an Electrolytic Cell using High-Tc SQUID*", Applied Superconductivity Conference 2012, Portland, Oregon, USA, 7-12 October 2012.

25. Y. Fukudome, S. Miyazaki, **M.M. Saari**, K. Sakai, T.Kiwa, A. Tsukamoto, S. Adachi, K. Tanabe, A. Kandori, K. Tsukada, "*Evaluation of Solar Panels by Measuring Tangential Component of Magnetic Fields*", Applied Superconductivity Conference 2012, Portland, Oregon, USA, 7-12 October 2012.

26. K. Sakai, **M. Mawardi Saari**, T. Kiwa, A. Tsukamoto, S. Adachi, K. Tanabe, A. Kandori, K. Tsukada, "*Improvement of Sensitivity for a Compact Magnetometer using HTS-SQUID and Rotating Sample*", 11th International Symposium on High Temperature Superconductors in High Frequency Fields (HTSHFF 2012), Miyagi , Japan, 29 May-1 June 2012.

27. K. Tsukada, **M. Mawardi Saari**, Ryuki Takagi, K. Sakai, T.Kiwa, A. Tsukamoto, S. Adachi, K. Tanabe, A. Kandori, "*Compact Magnetometers using HTS-SQUID for Detection of Magnetic Property*", 11th International Symposium on High Temperature Superconductors in High Frequency Fields (HTSHFF 2012), Miyagi , Japan, 29 May-1 June 2012.

28. Ryuki Takagi, **Mohd Mawardi Saari**, Kenji Sakai, Toshihiko Kiwa, Akira Tsukamoto, Seiji Adachi, Keiichi Tanabe, Akihiko Kandori, Keiji Tsukada, "*A Compact Moving-Sample Magnetometer using High-T$_C$ SQUID*", 24th International Cryogenic Engineering Conference and International Cryogenic Materials Conference 2012 (ICEC24-ICMC2012), Fukuoka, Japan ,14-18 May, 2012.

29. Shingo Miyazaki, Yohei Fukudome, **Mohd Mawardi Saari**, Kenji Sakai, Toshihiko Kiwa, Akira Tsukamoto, Seiji Adachi, Keiichi Tanabe, Akihiko Kandori, Keiji Tsukada, "*Electrical Property Mapping System of the Solar Panels using High-Tc SQUID*", 24th International Cryogenic Engineering Conference and International Cryogenic Materials Conference 2012 (ICEC24-ICMC2012), Fukuoka, Japan ,14-18 May, 2012.

30. K. Tsukada, S. Maeda, **M. Mawardi**, K. Sakai, T. Kiwa, A. Tsukamoto, S. Adachi, K. Tanabe, A. Kandori, "*Compact AC and DC magnetometers using HTS-SQUID*", 24rd International Symposium on Superconductivity (ISS 2011), Tokyo, Japan, 24-26, Oct., 2011.

31. Kenji Sakai, **Mawarudei Mohamado**, Toshihiko Kiwa, Akira Tsukamoto, Seiji Adachi, Keiichi Tanabe, Akihiko Kandori, Keiji Tsukada, "*Development of Compact DC Magnetic Susceptibility Meter using HTS-SQUID*", Superconductivity Centennial Conference 2011(EUCAS-ISEC-ICMC 2011), Hague, Netherlands, 18-23, Sep., 2011.

(DOMESTIC CONFERENCES)

1. 堺健司、渡部裕太、岡本直大、**モハマド マワルディ サーリ**、紀和利彦、塚田啓二，「高温超伝導 SQUID を用いた磁気計測システムの高精度化と水分量計測への応用」，第 23 回 MAGDA コンファレンス，高松， 12/4/2014.

2. 堺　健司・岡本直大・渡部裕太・**Saari Mohd Mawardi**・紀和利彦・塚田啓二，「HTS-SQUID を用いた試料回転式磁化率計の試料形状最適化による高感度計測法の検討」，2014 年電子情報通信学会ソサイエティ大会，徳島，9/23/2014.

3. **モハマド マワルディ サーリ**，森田 洪爾，石原 優一，日下 瞬，堺 健司，紀和 利彦，塚田 啓二，「高温超伝導 SQUID 用いた磁化率計の複合型 AC/DC 検出ユニットの最適化」，2014 第 75 回 応用物理学会秋季学術講演，北海道，2014/9/17-20.

4. 森田洪爾、**Mohd Mawardi Saari**、石原優一、日下瞬、塚本有哉、堺健司、紀和利彦、塚田啓二，「HTS-SQUID を用いた高精度磁化率計の開発と水溶液中の磁気ナノ粒子への応用」，2014 年度　応用物理·物理系学会中四国支部合同学術講演会，7/26/2014.

5. 田中 洸平，糟谷 尚平，**モハマド マワルディ サーリ**，堺 健司，紀和 利彦，塚田 啓二，「直冷式 HTS-SQUID を用いた太陽電池の光応答特性評価システムの開発」，2014 年度　応用物理·物理系学会中四国支部合同学術講演会，7/26/2014.

6. 渡部 裕太，岡本 直大，**モハマド マワルディ サーリ**，堺 健司，紀和 利彦，塚田　啓二，「HTS-SQUID を用いた回転型磁化率計の高感度化の研究」，2014 年度　応用物理·物理系学会中四国支部合同学術講演会，7/26/2014.

7. 田中洸平，宮崎真伍，糟谷尚平，**Mohd Mawardi Saari**，堺 健司，紀和利彦，塚田啓二，「HTS-SQUID グラジオメータを用いた太陽電池評価システムの開発」，平成 26 年　電気学会全国大会，愛媛，3/19/2014.

8. 森田洪爾，**Mohd Mawardi Saari**，高木竜輝，石原優一，日下瞬，塚本有哉，堺健司，紀和利彦，塚田啓二，「HTS-SQUID を用いた AC/DC 複合小型磁化率計の研究開発」，平成 26 年　電気学会全国大会，愛媛，3/19/2014.

9. 堺　健司，日下　瞬，岡本直大，濵﨑大地，**Mohd Mawardi Saari**，紀和利彦，塚田啓二，「HTS-SQUID を用いた磁気応答計測システムの高感度化による水分量評価への応用」，2014 電子情報通信学会　総合大会，新潟，3/21/2014.

10. モハマド　マワルディ　サーリ，塚本　有哉，石原　優一，日下　瞬，堺　健司，紀和　利彦，塚田　啓二，「AC/DC 高温超伝導 SQUID 磁化率計による水溶液中の酸化鉄ナノ粒子の磁気特性計測」，2014 春季 第 61 回 応用物理学会学術講演会，横浜，2014/3/17-20.

11. 堺　健司，岡本直大，浜崎大地，**モハマド マワルディ サーリ**，紀和利彦，塚田啓二，「HTS-SQUID を用いた試料回転式磁化率計の高感度化と磁気緩和信号の測定」，超伝導エレクトロニクス研究会，東京，2014/1/23-24.

12. 濱﨑 大地， 岡本 直大，**モハマド マワルディ サーリ**，紀和 利彦，塚田 啓二，「HTS-SQUID を用いたサンプル回転方式小型磁化率計の高感度化」， 第12 回低温工学・超伝導若手合同講演会，大阪，2013.12.7.

13. 宮崎 真伍，糟谷 尚平，**モハマド マワルディ サーリ**，紀和 利彦，塚田 啓二，「直冷式平面型 HTS-SQUID グラジオメータを用いた太陽電池評価」， 第12 回低温工学・超伝導若手合同講演会，大阪，2013.12.7.

14. 髙木 竜輝，**モハマド マワルディ サーリ**，石原 優一，紀和 利彦，塚田 啓二，「HTS-SQUID を用いた AC/DC 複合型小型磁化率計」，第 12 回低温工学・超伝導若手合同講演会，大阪，2013.12.7.

15. 高木竜輝，石原優一，**Mohd Mawardi Saari**，堺健司，紀和利彦，塚田啓二，「HTS-SQUID を用いた AC/DC 複合小型磁化率計の開発」， 2013 年 第 74 回応用物理学会秋季学術講演会．京都，2013.9.16-20.

16. 宮崎真伍，糟谷尚平，**サーリ モハマド マワルディ**，堺健司，紀和利彦，塚本晃，安達誠司，田辺圭一，塚田啓二，「HTS-SQUID グラジオメータを用いた太陽電池直流電流計測システムの開発」， 2013 年 第 74 回応用物理学会秋季学術講演会，京都，2013.9.16-20.

17. 濱﨑 大地，岡本直大，**モハマド マワルディ サーリ**，堺 健司，紀和 利彦，塚田 啓二，「HTS-SQUID を用いたサンプル回転型小型磁化率計の高感度化」，2013 年 第 74 回応用物理学会秋季学術講演会，京都，2013.9.18.

18. 堺 健司，岡本直大，濱﨑大地，**モハマド マワルディ サーリ**，紀和利彦，塚田啓二，「HTS-SQUID を用いた磁気緩和測定システムの高精度化」， 2013 年電子情報通信学会ソサイエティ大会，福岡，2013.9.19.

19. 堺健司，日下瞬，岡本直大，濱崎大地，**モハマド マワルディ サーリ**，紀和利彦，塚田啓二，「HTS-SQUID を用いた試料回転型磁化率計の最適化と水分量計測への応用」，超伝導エレクトロニクス研究会，仙台，2013.10.2-3.

20. 塚本 有哉，**モハマド マワルディ サーリ**，髙木竜輝，堺 健司，紀和 利彦，塚田 啓二，「HTS-SQUID 磁気特性評価装置における高調波検波方式の研究」，2013 応用物理学会中国四国支部合同学術講演会，香川，2013.7.27.

21. 日下 瞬，**モハマド マワルディ サーリ**，髙木竜輝，堺 健司，紀和 利彦，塚田 啓二，「高温超伝導 SQUID を用いた磁気特性評価装置によるモルタル水分量測定」，2013 応用物理学会中国四国支部合同学術講演会，香川，2013.7.27.

22. 石原 優一，**モハマド マワルディ サーリ**，髙木竜輝，堺 健司，紀和 利彦，塚田 啓二，「HTS-SQUID 磁気特性評価装置における AC 磁場検出方式の最適化」， 2013 応用物理学会中国四国支部合同学術講演会，香川，2013.7.27.

23. 岡本 直大，濱崎 大地，**モハマド マワルディ サーリ**，堺 健司，紀和 利彦，塚田 啓二，「HTS-SQUID を用いたサンプル回転型小型磁化率計の開発」，2013 第 37 回日本磁気学会学術講演会，北海道，2013.9.3-6.

24. 日下　瞬，**モハマド マワルディ サーリ**，髙木 竜輝，堺 健司，紀和 利彦，塚田 啓二，「高温超伝導 SQUID を用いた小型磁化率計による水分量測定」，2013 第 37 回日本磁気学会学術講演会，北海道，2013.9.3-6.

25. 石原 優一，**モハマド マワルディ サーリ**，髙木 竜輝，堺 健司，紀和 利彦，塚田 啓二，「高温超伝導 SQUID を用いた DC・AC 複合小型磁化率計の開発」，2013 第 37 回日本磁気学会学術講演会，北海道，2013.9.3-6.

26. 糟谷　尚平，宮崎　真伍，**モハマド マワルディ サーリ**，堺 健司，紀和 利彦，塚田 啓二，「高温超伝導 SQUID を用いた太陽電池特性自動計測システムの開発」，2013 電気学会基礎・材料・共通部門大会，横浜，2013.9.12-13.

27. 堺 健司，岡本　直大，濱﨑　大地，**モハマド マワルディ サーリ**，紀和 利彦，塚田 啓二，「HTS-SQUID を用いた磁化率計による水の磁気信号計測と水分量測定への応用」，2013 電気学会基礎・材料・共通部門大会, 横浜, 2013.9.12-13.

28. 塚本 有哉，**モハマド マワルディ サーリ**，髙木 竜輝，堺 健司，紀和 利彦，塚田 啓二，「HTS-SQUID 磁気特性評価装置を用いた水溶液中の酸化鉄ナノ粒子の高感度測定」，2013 電気学会基礎・材料・共通部門大会，横浜，2013.9.12-13.

29. 髙木 竜輝，**モハマド マワルディ サーリ**，石原 優一，堺 健司，紀和 利彦，塚田 啓二，「高温超伝導 SQUID を用いた DC/AC 複合小型磁化率計の開発」，2013 年度春季低温工学・超電導学会，東京，2013.5.13.

30. 堺健司，濱崎大地，**モハマド マワルディ サーリ**，紀和利彦，塚田啓二，「HTS-SQUID を用いた交流磁化率計の開発とシステムの最適化」，超伝導エレクトロニクス研究会，東京，2013.7.22.

31. 糟谷 尚平，宮崎 真伍，**モハマド マワルディ サーリ**，堺 健司，紀和 利彦，塚田 啓二，「HTS-SQUID を用いた太陽電池の光応答特性分布解析」，2013 応用物理学会中国四国支部合同学術講演会，香川，2013.7.27.

32. 岡本 直大，濱崎 大地，**モハマド マワルディ サーリ**，堺 健司，紀和 利彦，塚田 啓二，「回転型 HTS-SQUID 磁化率計における高感度検出法の研究」，2013 応用物理学会中国四国支部合同学術講演会，香川，2013.7.27.

33. 宮崎 真伍，福留 陽平，**モハマド マワルディ サーリ**，堺 健司，紀和 利彦，塚田 啓二，「HTS-SQUID 磁気計測による太陽電池電気特性評価」，2013 電子情報通信学会　総合大会，岐阜，2013.03.22.

34. 堺　健司，濱﨑大地，**モハマド マワルディ サーリ**，紀和利彦，塚田啓二，「HTS-SQUID を用いた試料回転式小型磁化率計のシステム改善による高感度化」，2013 電子情報通信学会　総合大会，岐阜，2013.03.22.

35. 濱﨑 大地，**モハマド マワルディ サーリ**，堺 健司，紀和 利彦，塚田 啓二，「HTS-SQUID を用いたサンプル回転方式小型磁気計測計による磁気緩和測定」，平成 25 年　電気学会全国大会，名古屋，2013.3.22.

36. モハマド マワルディ サーリ， 髙木 竜輝，堺 健司,，紀和 利彦，塚田 啓二，「 "高感度計測法を用いた高温超伝導 SQUID 磁化率計」，2013 春季 第 60 回 応用物理学会学術講演会，神奈川，2013.3.27-30.

37. 堺健司，濱崎大地，モハマド マワルディ サーリ，紀和利彦，塚田啓二，「HTS-SQUID を用いたサンプル回転式小型磁化率計の高感度計測手法の検討」，超伝導エレクトロニクス研究会，岡山，2013.1.24.

38. 堺 健司，モハマド マワルディ サーリ，濵崎 大地，紀和 利彦，塚田 啓二，「HTS-SQUID を用いた小型磁化率計の開発と磁気緩和測定」，第 11 回低温工学・超伝導若手合同講演会，大阪，2012.12.7.

39. モハマド マワルディ サーリ，高木 竜輝，堺 健司，紀和 利彦，塚田 啓二，「高温超伝導 SQUID を用いたサンプル振動方式小型磁化率計の高感度計測法」平成 24 年度（第 63 回）電気・情報関連学会中国支部大会プログラム，松江，2012.10.20.

40. モハマド マワルディ サーリ，高木 竜輝，堺 健司,紀和 利彦，塚田 啓二，「サンプル振動型磁化率計の高感度計測法」第 73 秋季 回応用物理学会学術講演会，愛媛，2012.9.11-14.

41. モハマド マワルディ サーリ，高木 竜輝，堺 健司，紀和 利彦，塚本 晃，安達 成司，田辺 圭一，神鳥 明彦，塚田 啓二，「高温超伝導 SQUID を用いた小型サンプル振動方式磁化率計とサンプル形状の依存性」超伝導エレクトロニックス （SCE2012-9 - SCE2012-16），東京，2012.7.19.

42. モハマド マワルディ，前田 敏志，堺 健司，紀和 利彦，塚本 晃，安達 成司，田辺 圭一，神鳥 明彦，塚田 啓二，「高温超伝導 SQUID を用いた小型磁化率計の開発」第 72 回応用物理学会学術講演会，山形，2011.8.29-9.2.

43. 堺 健司，マワルディサーリ モハマド，浜崎 大地，紀和 利彦，円福 敬二，塚田 啓二，「HTS-SQUID を用いた磁気緩和測定用小型磁化率計の開発」第 73 秋季 回応用物理学会学術講演会，愛媛，2012.9.11-14.

44. 宮崎 真伍，福留 陽平，モハマド マワルディ サーリ，堺 健司，紀和 利彦，塚田 啓二，「HTS-SQUID 磁気計測による太陽電池電気特性評価」 2012 年度 応用物理学会 中四国支部学術講演会，山口，2012.7.28.

45. 髙木 竜輝，モハマド マワルディ サーリ，堺 健司，紀和 利彦，塚田 啓二，「高温超伝導 SQUID を用いた振動型小型磁化率計の開発」2012 年度 応用物理学会 中四国支部学術講演会，山口，2012.7.28.

46. 濵﨑 大地，モハマド マワルディ サーリ，堺 健司，紀和 利彦，塚田 啓二，「HTS-SQUID を用いたサンプル 回転型直流磁化率計の開発」2012 年度 応用物理学会 中四国支部学術講演会，山口，2012.7.28.

47. 堺 健司，モハマド マワルディ，紀和 利彦，塚本 晃，安達 成司，田辺 圭一，神鳥 明彦，塚田 啓二，「HTS-SQUID を用いた試料回転式小型磁化率計の開発」第 85 回(2011 年秋季) 低温工学・超電導学会，金沢，2011.11.9-11.

REFERENCES

[1] K. Enpuku, T. Tanaka, Y. Tamai, and M. Matsuo, "AC susceptibility of magnetic markers in suspension for liquid phase immunoassay," *J. Magn. Magn. Mater.*, vol. 321, no. 10, pp. 1621–1624, May 2009.

[2] F. Ludwig, E. Heim, S. Mäuselein, D. Eberbeck, and M. Schilling, "Magnetorelaxometry of magnetic nanoparticles with fluxgate magnetometers for the analysis of biological targets," *J. Magn. Magn. Mater.*, vol. 293, no. 1, pp. 690–695, May 2005.

[3] H. C. Bryant, N. L. Adolphi, D. L. Huber, D. L. Fegan, T. C. Monson, T. E. Tessier, and E. R. Flynn, "Magnetic Properties of Nanoparticles Useful for SQUID Relaxometry in Biomedical Applications.," *J. Magn. Magn. Mater.*, vol. 323, no. 6, pp. 767–774, Mar. 2011.

[4] S. Tanaka, T. Akai, M. Takemoto, Y. Hatsukade, T. Ohtani, Y. Ikeda, S. Suzuki, S. Adachi, and K. Tanabe, "Application of SQUID to magnetic contaminant detection," *Phys. C Supercond.*, vol. 470, no. 20, pp. 1507–1510, Nov. 2010.

[5] K. Tsukada, T. Kiwa, H. Tahara, E. Miyake, H. Yamada, A. Tsukamoto, and A. Kandori, "Highly Sensitive Measurement of Moisture Content Using HTS-SQUID," *IEEE Trans. Appl. Supercond.*, vol. 19, no. 3, pp. 878–881, Jun. 2009.

[6] R. L. Fagaly, "Superconducting quantum interference device instruments and applications," *Rev. Sci. Instrum.*, vol. 77, no. 10, p. 101101, 2006.

[7] S. Foner, "Versatile and Sensitive Vibrating-Sample Magnetometer," *Rev. Sci. Instrum.*, vol. 30, no. 7, p. 548, 1959.

[8] D. Smith, "Development of a Vibrating-Coil Magnetometer," *Rev. Sci. Instrum.*, vol. 27, no. 5, pp. 261–268, 1956.

[9] M. Pelizzone and A. Treyvaud, "A SQUID Susceptometer for Fields up to 8.5 Tesla," *Appl. Phys.*, vol. 24, pp. 375–379, 1981.

[10] A. D. Hibbs, R. E. Sager, S. Kumar, J. E. McArthur, a. L. Singsaas, K. G. Jensen, M. a. Steindorf, T. a. Aukerman, and H. M. Schneider, "A SQUID-based ac susceptometer," *Rev. Sci. Instrum.*, vol. 65, no. 8, p. 2644, 1994.

[11] B. M. Zawilski, D. L. E. Maillard, O. Geoffroy, and D. Dufeu, "Rotating sample magnetometer for precise, real time differential measurements," *Rev. Sci. Instrum.*, vol. 77, no. 1, p. 015102, 2006.

[12] M. Cerdonio, F. Mogno, G. L. Romani, C. Messana, and C. Gramaccioni, "Oscillating sample superconducting magnetometer," *Rev. Sci. Instrum.*, vol. 48, no. 3, p. 300, 1977.

[13] J. S. Philo and W. M. Fairbank, "High-sensitivity magnetic susceptometer employing superconducting technology," vol. 94305, no. July 1977, pp. 1529–1536, 1978.

[14] A. Pasquarelli, C. Del Gratta, S. Della Penna, S. Di Luzio, V. Pizzella, and G. L. Romani, "A SQUID based AC susceptometer for the investigation of large samples.," *Phys. Med. Biol.*, vol. 41, no. 11, pp. 2533–9, Nov. 1996.

[15] J. C. and A.I.Braginski, *The SQUID Handbook: Vol. 1 Fundamental and technology of SQUIDs and SQUIDs Systems*. WILEY-VCH Verlag GmbH & Co. KGaA,Weiheim, 2004.

[16] S. Adachi, a. Tsukamoto, Y. Oshikubo, T. Hato, and K. Tanabe, "Fabrication of integrated HTS-SQUID magnetometers having multiturn input coils with different sizes," *Phys. C Supercond.*, vol. 471, no. 21–22, pp. 1258–1262, Nov. 2011.

[17] A. Tsukamoto, K. Saitoh, D. Suzuki, N. Sugita, Y. Seki, A. Kandori, K. Tsukada, Y. Sugiura, S. Hamaoka, H. Kuma, N. Hamasaki, and K. Enpuku, "Development of Multisample Biological Immunoassay System Using HTS SQUID and Magnetic Nanoparticles," *IEEE Trans. Appl. Supercond.*, vol. 15, no. 2, pp. 656–659, Jun. 2005.

[18] A. Tsukamoto, K. Saitoh, N. Sugita, H. Kuma, Y. Sugiura, S. Hamaoka, N. Hamasaki, and K. Enpuku, "Improvement of sensitivity of multisample biological immunoassay system using HTS SQUID and magnetic nanoparticles," *Phys. C Supercond.*, vol. 445–448, pp. 975–978, Oct. 2006.

[19] Y. Hatsukade, K. Hayashi, Y. Shinyama, Y. Kobayashi, S. Adachi, K. Tanabe, and S. Tanaka, "Characteristics of an HTS-SQUID gradiometer with ramp-edge Josephson junctions and its application on robot-based 3D-mobile compact SQUID NDE system," *Phys. C Supercond.*, vol. 471, no. 21–22, pp. 1228–1233, Nov. 2011.

[20] A. Kandori, M. Ueda, H. Ogata, and H. Kado, "Considerations on the use of high resistance signal wires for SQUID systems," *Cryogenics (Guildf).*, vol. 35, no. 4, pp. 239–242, 1995.

[21] K. Enpuku, Y. Tsuji, S. Hirakawa, M. Matsuo, and T. Yoshida, "Performance of HTS SQUID coupled to cooled-Cu/superconductor pickup coil," *Phys. C Supercond.*, vol. 470, no. 20, pp. 1511–1514, Nov. 2010.

[22] K. Enpuku, S. Hirakawa, R. Momotomi, M. Matsuo, and T. Yoshida, "Performance of HTS SQUID using resonant coupling of cooled Cu pickup coil," *Phys. C Supercond.*, vol. 471, no. 21–22, pp. 1234–1237, Nov. 2011.

[23] K. Tsukada, T. Kiwa, and Y. Masuda, "AC Magnetic Properties of Large Volume of Water -- Susceptibility Measurement in Unshielded Environment," *Jpn. J. Appl. Phys.*, vol. 45, no. No. 41, pp. L1097–L1099, Oct. 2006.

[24] K. Enpuku, S. Nabekura, Y. Tsuji, S. Okada, M. Matsuo, a. Tsukamoto, T. Mizoguchi, and a. Kandori, "Detection of magnetic nanoparticles utilizing cooled normal pickup coil and high Tc SQUID," *Phys. C Supercond.*, vol. 469, no. 15–20, pp. 1634–1637, Oct. 2009.

[25] N. Thanh, *Magnetic nanoparticles: from fabrication to clinical applications*. CRC Press, 2012, p. 616.

[26] S. TUMANSKI, "Modern magnetic field sensors–a review," *Organ*, no. 10, pp. 1–12, 2013.

[27] S. Tumanski, "Induction coil sensors—a review," *Meas. Sci. Technol.*, vol. 18, no. 3, pp. R31–R46, Mar. 2007.

[28] M. M. Saari, Y. Ishihara, Y. Tsukamoto, T. Kusaka, K. Morita, K. Sakai, T. Kiwa, and K. Tsukada, "Optimization of an AC/DC High-Tc SQUID Magnetometer Detection Unit for Evaluation of Magnetic Nanoparticles in Solution," *IEEE Trans. Appl. Supercond.*, vol. 25, no. 3, pp. 1–4, Jun. 2015.

[29] R. Kleiner, D. Koelle, F. Ludwig, and J. Clarke, "Superconducting quantum interference devices: State of the art and applications," *Proc. IEEE*, vol. 92, no. 10, pp. 1534–1548, Oct. 2004.

[30] J. Clark and A. Braginski, *The SQUID handbook, vol 2: applications of SQUIDs and SQUID systems*. 2006.

[31] T. Q. Yang and K. Enpuku, "SQUID magnetometer utilizing normal pickup coil and resonant-type coupling circuit," *Phys. C Supercond.*, vol. 392–396, pp. 1396–1400, Oct. 2003.

[32] G. Rietveld, P. de la Court, and H. E. van den Brom, "Internally Damped CCC for Accurate Measurements of Small Electrical Currents," *IEEE Trans. Instrum. Meas.*, vol. 58, no. 4, pp. 1196–1201, Apr. 2009.

[33] K. Knaack, M. Wendt, K. Wittenburg, D. Hamburg, R. Neubert, W. Vodel, F. Schiller, U. Jena, A. Peters, and G. S. I. Darmstadt, "CRYOGENIC CURRENT COMPARATOR FOR ABSOLUTE MEASUREMENTS OF THE DARK CURRENT OF SUPERCONDUCTING CAVITIES FOR TESLA 2 REQUIREMENTS OF THE DARK," pp. 1915–1917, 2002.

[34] J. Clarke, W. Goubau, and M. Ketchen, "Tunnel junction dc SQUID: fabrication, operation, and performance," *J. Low Temp. Phys.*, vol. 25, 1976.

[35] A. Tsukamoto, S. Adachi, Y. Oshikubo, K. Tanabe, and K. Enpuku, "Development of a HTS SQUID module for use with an external pickup coil," *Supercond. Sci. Technol.*, vol. 26, no. 1, p. 15013, Jan. 2013.

[36] S. Adachi, K. Hata, T. Sugano, H. Wakana, T. Hato, Y. Tarutani, and K. Tanabe, "Preparation of multilayer films for integrated high-Tc SQUIDs with ramp-edge Josephson junctions," *Phys. C Supercond.*, vol. 468, no. 15–20, pp. 1936–1941, Sep. 2008.

[37] K. Nguyen, T. Ng, and I. Chen, "On algorithms for planning s-curve motion profiles," *Int. J. Adv. Robot. Syst.*, vol. 5, no. 1, pp. 99–106, 2008.

[38] J. D. Kraus and D. A. Fleisch, "Electromagnetics with Applications," in *Electromagnetics with Applications*, 5th ed., New York: McGraw-Hill, 1999, p. 407.

[39] C. Jooss, R. Warthmann, A. Forkl, and H. Kronmüller, "High-resolution magneto-optical imaging of critical currents in YBa2Cu3O7−δ thin films," *Phys. C Supercond.*, vol. 299, no. 3–4, pp. 215–230, 1998.

[40] C. N. Guy, "Frequency doubling-a new approach to vibrating sample magnetometers," *J. Phys. E Sci. Instruments*, vol. 9, no. 6, p. 433, 1976.

[41] T. Johansson and K. Nielsen, "A low frequency vibrating sample magnetometer," *J. Phys. E.*, vol. 9, no. 10, pp. 852–854, 1976.

[42] G. Bowden, "Detection coil systems for vibrating sample magnetometers," *J. Phys. E.*, vol. 5, no. 11, p. 1115, 1972.

[43] M. M. Saari, R. Takagi, T. Kusaka, Y. Ishihara, Y. Tsukamoto, K. Sakai, T. Kiwa, and K. Tsukada, "Development of integrated AC-DC magnetometer using high- T c SQUID for magnetic properties evaluation of magnetic nanoparticles in solution," *J. Phys. Conf. Ser.*, vol. 507, no. 4, p. 042035, May 2014.

[44] A. Çolak, "A new model for the estimation of compressive strength of Portland cement concrete," *Cem. Concr. Res.*, vol. 36, no. 7, pp. 1409–1413, Jul. 2006.

[45] K. Tsukada and T. Kiwa, "Magnetic Measurement of Moisture Content of Grain," *IEEE Trans. Magn.*, vol. 43, no. 6, pp. 2683–2685, Jun. 2007.

[46] K. Tsukada, Y. Masuda, Y. Ishihara, and T. Kiwa, "Magnetic Measurement of the Moisture Content in Soil: Diamagnetic Measurement with the Presence of Ferromagnetic Material," *Appl. Phys. Express*, vol. 1, p. 067008, Jun. 2008.

[47] K. Tsukada, T. Kusaka, M. M. Saari, R. Takagi, K. Sakai, T. Kiwa, and Y. Bito, "Magnetic susceptibility and magnetic resonance measurements of the moisture content and hydration condition of a magnetic mixture material," *J. Appl. Phys.*, vol. 115, no. 17, p. 17E301, May 2014.

[48] H. Nishikawa, R. Nakamura, Y. Ohki, and Y. Hama, "Correlation of preexisting diamagnetic defect centers with induced paramagnetic defect centers by ultraviolet or vacuum-ultraviolet photons in high-purity silica glasses," *Phys. Rev. B*, vol. 48, no. 21, pp. 15584–15594, Dec. 1993.

[49] Q. A. Pankhurst, N. T. K. Thanh, S. K. Jones, and J. Dobson, "Progress in applications of magnetic nanoparticles in biomedicine," *J. Phys. D. Appl. Phys.*, vol. 42, no. 22, p. 224001, 2009.

[50] H. Mamiya and B. Jeyadevan, "Hyperthermic effects of dissipative structures of magnetic nanoparticles in large alternating magnetic fields.," *Sci. Rep.*, vol. 1, p. 157, Jan. 2011.

[51] K. Enpuku, A. Ohba, K. Inoue, and T. Q. Yang, "Application of HTS SQUIDs to biological immunoassays," *Phys. C Supercond.*, vol. 412–414, pp. 1473–1479, Oct. 2004.

[52] K. Enpuku, H. Watanabe, Y. Higuchi, T. Yoshida, H. Kuma, N. Hamasaki, M. Mitsunaga, H. Kanzaki, and A. Kandori, "Characterization of Magnetic Markers for Liquid-Phase Immunoassays Using Brownian Relaxation," *Jpn. J. Appl. Phys.*, vol. 51, p. 023002, Jan. 2012.

[53] G. Glöckl, V. Brinkmeier, K. Aurich, E. Romanus, P. Weber, and W. Weitschies, "Development of a liquid phase immunoassay by time-dependent measurements of the

transient magneto-optical birefringence using functionalized magnetic nanoparticles," *J. Magn. Magn. Mater.*, vol. 289, pp. 480–483, Mar. 2005.

[54] K. Enpuku, M. Hotta, and a. Nakahodo, "High-Tc SQUID system for biological immunoassays," *Phys. C Supercond.*, vol. 357–360, pp. 1462–1465, Aug. 2001.

[55] K. Enpuku, T. Tanaka, T. Matsuda, F. Dang, N. Enomoto, J. Hojo, K. Yoshinaga, F. Ludwig, F. Ghaffari, E. Heim, and M. Schilling, "Properties of magnetic nanoparticles in the Brownian relaxation range for liquid phase immunoassays," *J. Appl. Phys.*, vol. 102, no. 5, p. 054901, 2007.

[56] M. J. Chiu, H. E. Horng, J. J. Chieh, S. H. Liao, C. H. Chen, B. Y. Shih, C. C. Yang, C. L. Lee, T. F. Chen, S. Y. Yang, C. Y. Hong, and H. C. Yang, "Multi-Channel SQUID-Based Ultra-High-Sensitivity In-Vitro Detections for Bio-Markers of Alzheimer's Disease Via Immunomagnetic Reduction," *IEEE Trans. Appl. Supercond.*, vol. 21, no. 3, pp. 477–480, Jun. 2011.

[57] F. Oisjöen, J. F. Schneiderman, A. P. Astalan, A. Kalabukhov, C. Johansson, and D. Winkler, "A new approach for bioassays based on frequency- and time-domain measurements of magnetic nanoparticles.," *Biosens. Bioelectron.*, vol. 25, no. 5, pp. 1008–13, Jan. 2010.

[58] S. Tanaka, C. Toriyabe, Y. Torii, Y. Hatsukade, T. Eki, S. Katsura, N. Ohnishi, J. Wan, S. Yang, and Y. Zhang, "Evaluation of thermo responsive magnetic nano-particles for high-Tc SQUID bio application," *Phys. C Supercond.*, vol. 463–465, pp. 1029–1033, Oct. 2007.

[59] B. Gleich and J. Weizenecker, "Tomographic imaging using the nonlinear response of magnetic particles," *Nature*, vol. 435, no. 7046, pp. 1214–7, Jun. 2005.

[60] J. Weizenecker, B. Gleich, J. Rahmer, H. Dahnke, and J. Borgert, "Three-dimensional real-time in vivo magnetic particle imaging.," *Phys. Med. Biol.*, vol. 54, no. 5, pp. L1–L10, Mar. 2009.

[61] T. F. Sattel, T. Knopp, S. Biederer, B. Gleich, J. Weizenecker, J. Borgert, and T. M. Buzug, "Single-sided device for magnetic particle imaging," *J. Phys. D. Appl. Phys.*, vol. 42, no. 2, p. 022001, Jan. 2009.

[62] N. B. Othman, T. Tsubaki, T. Yoshida, K. Enpuku, and A. Kandori, "Magnetic Nanoparticle Imaging Using Harmonic Signals," *IEEE Trans. Magn.*, vol. 48, no. 11, pp. 3776–3779, Nov. 2012.

[63] K. Enpuku, T. Morishige, T. Mihaya, T. Miyazai, M. Matsuo, S. Haku, and T. Yoshida, "Magnetic Nanoparticle Imaging Using Cooled Pickup Coil and Harmonic Signal Detection," *Jpn. J. Appl. Phys.*, vol. 52, p. 087001, Jul. 2013.

[64] L. Trahms, "Colloidal Magnetic Fluids," vol. 763, S. Odenbach, Ed. Berlin, Heidelberg: Springer Berlin Heidelberg, 2009, pp. 327–358.

[65] C.-Y. Hong, C. C. Wu, Y. C. Chiu, S. Y. Yang, H. E. Horng, and H. C. Yang, "Magnetic susceptibility reduction method for magnetically labeled immunoassay," *Appl. Phys. Lett.*, vol. 88, no. 21, p. 212512, 2006.

[66] V. L. Calero-DdelC, D. I. Santiago-Quiñonez, and C. Rinaldi, "Quantitative nanoscale viscosity measurements using magnetic nanoparticles and SQUID AC susceptibility measurements," *Soft Matter*, vol. 7, no. 9, p. 4497, 2011.

[67] J. B. Weaver, X. Zhang, E. Kuehlert, S. Toraya-Brown, D. B. Reeves, I. M. Perreard, and S. Fiering, "Quantification of magnetic nanoparticles with low frequency magnetic fields: compensating for relaxation effects.," *Nanotechnology*, vol. 24, no. 32, p. 325502, Aug. 2013.

[68] T. Yoshida, K. Ogawa, T. Tsubaki, N. B. Othman, and K. Enpuku, "Detection of Magnetic Nanoparticles Using the Second-Harmonic Signal," *IEEE Trans. Magn.*, vol. 47, no. 10, pp. 2863–2866, Oct. 2011.

[69] N. L. Adolphi, D. L. Huber, J. E. Jaetao, H. C. Bryant, D. M. Lovato, D. L. Fegan, E. L. Venturini, T. C. Monson, T. E. Tessier, H. J. Hathaway, C. Bergemann, R. S. Larson, and E. R. Flynn, "Characterization of magnetite nanoparticles for SQUID-relaxometry and magnetic needle biopsy," *J. Magn. Magn. Mater.*, vol. 321, no. 10, pp. 1459–1464, May 2009.

[70] N. L. Adolphi, D. L. Huber, H. C. Bryant, T. C. Monson, D. L. Fegan, J. Lim, J. E. Trujillo, T. E. Tessier, D. M. Lovato, K. S. Butler, P. P. Provencio, H. J. Hathaway, S. a Majetich, R. S. Larson, and E. R. Flynn, "Characterization of single-core magnetite nanoparticles for magnetic imaging by SQUID relaxometry.," *Phys. Med. Biol.*, vol. 55, no. 19, pp. 5985–6003, Oct. 2010.

[71] K. Enpuku, K. Soejima, T. Nishimoto, H. Tokumitsu, H. Kuma, N. Hamasaki, and K. Yoshinaga, "Liquid phase immunoassay utilizing magnetic marker and high T[sub c] superconducting quantum interference device," *J. Appl. Phys.*, vol. 100, no. 5, p. 054701, 2006.

[72] A. Tsukamoto, H. Kuma, K. Saitoh, A. Kandori, K. Yoshinaga, Y. Sugiura, N. Hamasaki, and K. Enpuku, "Reduction of the magnetic signal from unbound magnetic markers for magnetic immunoassay without bound/free separation," *Phys. C Supercond.*, vol. 463–465, pp. 1024–1028, Oct. 2007.

[73] F. Ludwig, E. Heim, and M. Schilling, "Characterization of superparamagnetic nanoparticles by analyzing the magnetization and relaxation dynamics using fluxgate magnetometers," *J. Appl. Phys.*, vol. 101, p. 113909, 2007.

[74] T. Yoshida, N. B. Othman, T. Tsubaki, J. Takamiya, and K. Enpuku, "Evaluation of Harmonic Signals for the Detection of Magnetic Nanoparticles," *IEEE Trans. Magn.*, vol. 48, no. 11, pp. 3788–3791, Nov. 2012.

[75] D. V Berkov, P. Görnert, N. Buske, C. Gansau, J. Mueller, M. Giersig, W. Neumann, and D. Su, "New method for the determination of the particle magnetic moment distribution in a ferrofluid," *J. Phys. D. Appl. Phys.*, vol. 33, no. 4, pp. 331–337, Feb. 2000.

[76] J. van Rijssel, B. W. M. Kuipers, and B. H. Erné, "Non-regularized inversion method from light scattering applied to ferrofluid magnetization curves for magnetic size distribution analysis," *J. Magn. Magn. Mater.*, vol. 353, pp. 110–115, Mar. 2014.

[77] A. Kákay, M. W. Gutowski, L. Takacs, V. Franco, and L. K. Varga, "Langevin granulometry of the particle size distribution," *J. Phys. A. Math. Gen.*, vol. 37, no. 23, pp. 6027–6041, Jun. 2004.

[78] W. Press, B. Flannery, S. Teukolsky, and W. Vetterling, *Numerical Recipes: The art of scientific computing*, 3rd ed. Cambridge University Press, 2007, p. 1256.

[79] V. John, I. Angelov, A. A. Öncül, and D. Thévenin, "Techniques for the reconstruction of a distribution from a finite number of its moments," *Chem. Eng. Sci.*, vol. 62, no. 11, pp. 2890–2904, Jun. 2007.

[80] M. D. Woodhams and M. D. Hendy, "Reconstructing phylogeny by quadratically approximated maximum likelihood.," *Bioinformatics*, vol. 20 Suppl 1, pp. i348–54, Aug. 2004.

[81] C. L. Lawson and R. J. Hanson, *Solving Least Squares Problems*. Englewood Cliffs, NJ: Prentice-hall, 1974.